A two layer model for simulating Baltic Sea inflows

Hannes Rennau

Master Thesis
University of Rostock

at the
Baltic Sea Research Institute of Warnemünde
Seestrasse 15
D-18119 Rostock

May 26, 2006

Für meine Söhne Hendrik, Bennet und Lasse. Und Yvonne.

Table of Contents

1 Introduction **1**
1.1 Baltic Sea inflow events 1

2 Theory **7**
2.1 Notation 7
2.2 2D two layer model equations 8
2.2.1 Derivation of dynamic equations for surface and interface 9
2.2.2 Dynamic equations for horizontal velocities 11
2.2.3 Bottom friction 14
2.2.4 Horizontal density advection 16
2.2.5 Entrainment 17
2.3 Summary of 2D model equations 21
2.4 3D two layer model equations 22
2.4.1 Dynamic equations for surface and interface 22
2.4.2 Bottom friction 22
2.4.3 Horizontal density advection 22
2.4.4 Horizontal momentum diffusion 22
2.4.5 Dynamic equations for horizontal transport 23
2.4.6 Entrainment 23
2.5 Summary of 3D model equations 24

3 Numerical implementation **25**
3.1 Discretisation and numerical implementation 25
3.2 Discretiation for the 2D two layer model 26
3.2.1 Dynamic equations for surface and interface 26
3.2.2 Horizontal momentum advection 27
3.2.3 Horizontal density advection 28
3.2.4 Horizontal momentum diffusion 28
3.2.5 Bottom friction 28
3.3 Full discretized two layer model equations 29
3.4 Discretisation and numerical implementation for the 3D case 30
3.4.1 Dynamic equations for surface and interface 31

3.4.2 Dynamic equations of motion for horizontal velocities in transport form . . . 31
3.4.3 Horizontal momentum advection . . . 32
3.4.4 Horizontal density advection . . . 32
3.4.5 Horizontal momentum diffusion . . . 33
3.4.6 Bottom friction . . . 33
3.5 Full discretized two layer model equations . . . 33
3.6 Numerics . . . 36
3.6.1 The lateral boundaries of the plume - drying and flooding algorithm 36
3.6.2 Principle of pressure gradient minimization . . . 38
3.6.3 Individual model problem: interface touching surface . . . 38
3.6.4 Implementation of Entrainment . . . 38

4 Basic test experiments 41
4.1 Experiments without entrainment . . . 41
4.1.1 Experiments with linearized two layer model equations . . . 41
4.1.2 Application to standing internal wave . . . 42
4.1.3 Application to plume propagation . . . 47
4.1.4 Application to lock exchange experiment . . . 50
4.1.5 Lock exchange experiment with horizontal density gradient . . . 53
4.1.6 Application to Baltic Slice scenario . . . 54
4.2 Experiments with Entrainment . . . 56
4.2.1 Gravity current on linear slope topography . . . 56
4.2.2 Lock exchange experiment with entrainment . . . 57
4.2.3 Running Baltic slice scenario with two layer model and GETM . 58
4.3 Basic test experiments with 3D model . . . 60
4.3.1 Propagation of plume with entrainment and without rotation . . 60
4.3.2 Variation of bottom friction with rotation and without entrainment 60
4.3.3 Conclusions . . . 61

5 Simulation of Baltic Sea inflow event 71
5.1 Model setup and initial conditions . . . 71
5.2 Comparison of two layer model results to GETM . . . 73
5.2.1 Modeling the Arkona inflow event . . . 74
5.2.2 Velocities of bottom track of the plume . . . 76
5.2.3 Compare different bottom drag assumptions . . . 79
5.2.4 Variation of Froude number . . . 81
5.2.5 Cross section of plume south of Drodgen Sill . . . 81
5.2.6 Cross section of plume across Kriegers Shoal . . . 82
5.3 Baltic Sea inflow event with extended bathymetry . . . 86
5.3.1 Splitting and merging around Kriegers Shoal . . . 92

6 Conclusions 99

List of Figures

1.1 Map of the model domain for simulation of inflow event 1
1.2 3D picture of plume propagation during inflow event 2
1.3 Slice trough the Baltic Sea 3
1.4 Observed and simulated salinity (*Burchard et al.* [2005]) north of Kriegers Shoal 4

2.1 Schematic illustration of two-layer model 8
2.2 Bottom drag coefficient as a function of the plume thickness 15
2.3 Schematic illustration of the entrainment process 17
2.4 Bulk flux Richardson number as a function of a nonlinear combination of Froude and Ekman number 20

3.1 Staggered grid for numerical implementation 25
3.2 Staggered grid for discretisation of 3D two layer model 26
3.3 First order upstream scheme 27
3.4 Principle of pressure gradient minimization and emergency brake 37
3.5 Consequences of applying the emergency brake 39

4.1 Initial condition for simulation of standing internal wave 42
4.2 Elevation of internal wave in centre while solving the linear two layer model equations 43
4.3 Error between analytical and numerical solution for standing internal wave 48
4.4 Initial condition for plume test case 50
4.5 Plume propagation in box. Comparison of analytical and numerical solution 51
4.6 Schematic illustration of initial conditions for lock exchange experiment 52
4.7 Lock exchange experiment 53
4.8 Schematic illustration of initial condition of density lock exchange experiment 53
4.9 Lock exchange with horizontal density contrast in lower layer 55
4.10 Baltic slice with 2D two layer model 63
4.11 Surface elevation during Baltic slice scenario with 2D two layer model . 63
4.12 Baltic slice with 2D two layer model 64
4.13 Gravity current on a slope 65

4.14 Front position of a plume under different slope angles plotted over time 66
4.15 Lock exchange experiment with entrainment 66
4.16 Baltic slice scenario modeled with the GETM and the two layer model . 67
4.17 Linear slope topography for tests with 3D two layer model 67
4.18 Horizontal two-dimensional bottom current on a linear slope 68
4.19 Plume on linear slope topography with rotation under variation of the bottom drag coefficient 69

5.1 Bathymetric map of the Arkona Sea showing positions of observations (western purple line: Feb 1 2004; western red line: Feb 2 2004 and eastern red line: Feb 05 2004) and cross sections for investigations of model results (green lines) obtained with two layer model and GETM (*Burchard and Bolding* [2002]) 72
5.2 Flowrates north and south of Kriegers Shoal 74
5.3 Comparison of GETM-simulated near-bed salt distribution and plume salinity simulated with the two layer model 77
5.4 Time series of plume thickness at different positions during inflow event 78
5.5 Mean velocities in plume in quasi steady state during Arkona inflow event 78
5.6 Map showing track of maximum salinity values during inflow event . . . 79
5.7 Hovmueller plot for inflow events as a result of a realistic simulation of inflow events 80
5.8 Simulation of Arkona inflow event with different assumptions of the bottom drag coefficient 81
5.9 Impact of Froude number Fr on simulation results 82
5.10 Simulated salinity and current velocity with two layer model 83
5.11 Observed salinity and current velocity south of Drodgen Sill 84
5.12 Simulated salinity and current velocity with GETM 85
5.13 Two layer model simulated salinity and current velocity on a north south transect across Kriegers Shoal 87
5.14 Observed salinity and current velocity on a north-south transect across Kriegers Shoal 88
5.15 GETM-simulated salinity and current velocity on a north south transect across Kriegers Shoal 89
5.16 Idealized inflow event simulation with two layer model and GETM . . . 90
5.17 Simulated and observed salinities at the hydrographic stations Møn and Bornholm 93
5.18 Simulated salinities at different points in the western Baltic Sea 93
5.19 Flowrates in the Arkona Basin 94
5.20 Water mass fluxes at different positions during Arkona inflow event . . . 95
5.21 Flowrates for the Bornholm Channel 96
5.22 Current velocity vectors for the flow around Kriegers Shoal. 97
5.23 Velocity vectors, plume thickness and salinity for the flow around Kriegers Shoal 98

Nomenclature

η_1, η_2 Interface and surface elevation [m]

η_a Analytical solution for elevation [m]

λ Wave length [m]

ω Angular velocity [s^{-1}]

τ_b, τ_i, τ_s Bottom stress [m^2 s^{-2}]

ϱ_1, ϱ_2 Density in lower and upper layer [kg m^{-3}]

A_H Horizontal diffusion coefficient [m^2 s^{-1}]

ADV Horizontal momentum advection term

$ADVM$ Horizontal momentum advection term with mixed terms for 3D case

C Constant value for initial condition of analytical plume solution [m]

c Wave propagation speed [m s^{-1}]

C_D Bottom drag coefficient

c_p Experimentally determined value for calculation of entrainment rate

CFL Courant-Friedrich-Levy condition [m s^{-1}]]

COR Coriolis term

D_{min} Minimum thickness for lower layer [m]

$DIFF$ Horizontal momentum diffusion term

$DIFFM$ Horizontal momentum diffusion term with mixed terms for 3D case

E Entrainment rate

f Coriolis parameter [s^{-1}]

Fr Froude number

$FRIC$ Bottom friction term

g Gravity acceleration [m s^{-2}]

$g^{'}$ Reduced gravity [m s^{-2}]

H Depth [m]

h_1, h_2 Thickness of lower layer (plume) and upper layer (ambient water) [m]

H_E Δh_1 due to entrainment process with respect to timestep in simulation [m]

K Ekman number

k Wavenumber [m^{-1}]

L Domain length [m]

p Pressure [N m^{-2}]

$PRESSE$ External pressure gradient term

$PRESSI$ Internal pressure gradient term

R_i Richardson number

RHO Horizontal density gradient term

t Time [s]

U Velocity amplitude [m s^{-1}]

u, v, w Velocities in East, North and vertical direction [m s^{-1}]

u_* Friction velocity [m s^{-1}]

U_1, U_2 East component of vertically integrated transports in lower and upper layer [m^2 s^{-1}]

u_1, u_2 Mean horizontal velocities in lower and upper layer (east component) [m s^{-1}]

u_a Analytical solution for horizontal velocity [m s^{-1}]

V_1, V_2 North component of vertically integrated transports in lower and upper layer [m^2 s^{-1}]

v_1, v_2 Mean horizontal velocities in lower and upper layer (north component) [m s^{-1}]

w_E Entrainment velocity [m s^{-1}]

x, y, z Coordinates in East, North and vertical direction [m]

z_0 Bottom roughness length [m]

Chapter 1

Introduction

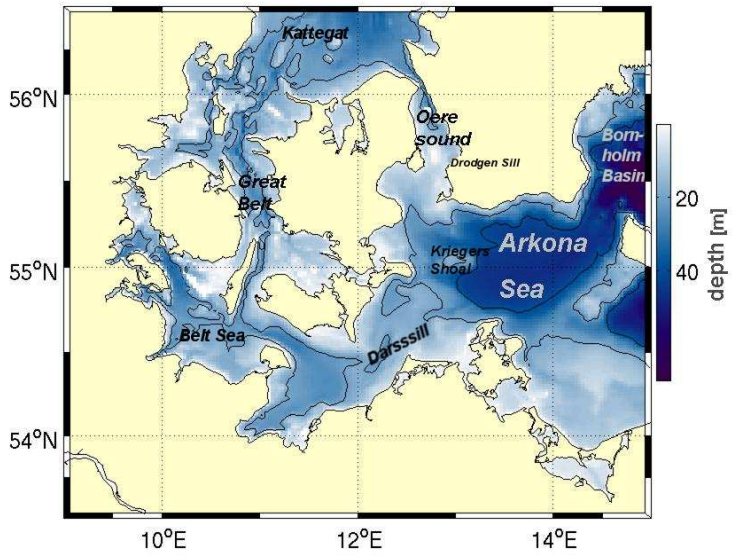

Figure 1.1: Picture showing the western Baltic Sea with the Arkona Basin. An inflow of a dense water plume from the North Sea is simulated for this region. By courtesy of Frank Janssen (BSH)

1.1 Baltic Sea inflow events

The occurance of Baltic Sea (see Fig. 1.1) inflow events has been well investigated in the work of *Matthäus and Franck* [1992]. It is shown that only major inflows, that approximately occur every ten years, can significantly affect the marine environment

due to the property that such bottom currents transport high amounts of saline and oxygenated water. Hence positive consequences of such inflow processes are for example deeper layer ventilation and increased natural reproduction. On this account, the supply with saline water has been part of different quantitative and qualitative investigations (*Kõuts and Omstedt* [1993], *Arneborg et al.* [2005], *Matthäus and Franck* [1992], *Burchard et al.* [2005], *Lass and Mohrholz* [2003]). The saline bottom current as shown in Fig. 1.2 can be considered as a lateral bordered layer of well mixed, dense water that is under the influence of Coriolis force, friction force and pressure gradient force. These dense bottom currents, called plumes, are diluted by the ambient brackish surface water with around 8 psu (practical salinity unit) (*Liljebladh and Stigebrandt* [1996]; *Burchard et al.* [2005]) of the Baltic Sea.

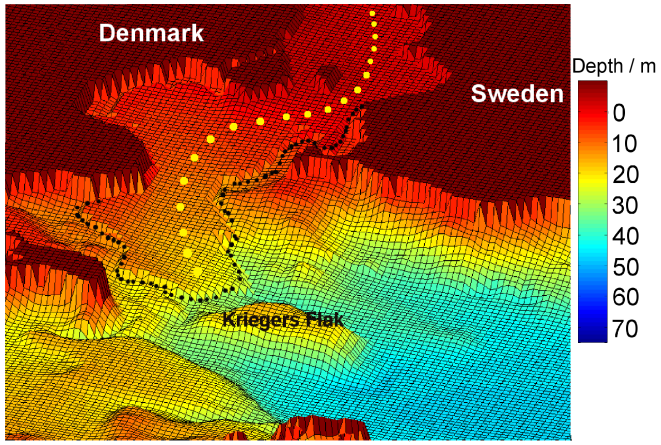

Figure 1.2: Sketch showing the plume of saline water shortly before it reaches Kriegers Flak. The yellow dots represent the main pathway through the Oeresund, crossing Drodgen Sill up to Kriegers Flak. This simulation is a result of an idealized Arkona inflow event modeled with the two layer model.

The water has to pass a set of narrow channels like the Stolpe Channel (1.3) and shallow sills like the Drodgen Sill (1.1) before reaching the eastern parts of the Baltic Sea. Fig 1.3 gives a very descriptive demonstration of the inflowing dense water with a slice through the main passway of the plume passing the Arkona Basin with a depth of around 50 m, the Bornholm Basin and finally reaching the Gotland Basin with depth values of up to 250 m. As the dense water descends the sills and basins it entrains ambient water. The vertical mixing process, called entrainment, is modifying the properties of the dense water (e.g. salinity, velocity, plume thickness). As shown in Fig. 1.3 this can be seen by decreasing salinity values with differences of around 4 psu between the Arkona Basin and the Bornholm Basin. It must be pointed out that

Fig. 1.3 only represents a qualitative result of an idealized two layer model simulation discussed in Sect. 4.2.3. Hence the net volumes and tracer properties of the water are highly sensitive at any point to the amount of entrainment that has taken place. Higher entrainment rates indicate faster mixing and thus a slower velocity of propagation of the bottom current.
Kõuts and Omstedt [1993] have defined three main mixing zones: The first two are the Sound (Oeresound; see Fig. 1.1) between Denmark and Sweden and the Belt Sea (Fig. 1.1) where the deep water inflow increases by 79%. In the second mixing zone, the Arkona Basin, the volume transport has an increase of 53% while in the third mixing zone, the Stolpe Channel (Fig. 1.3), the vertical mixing process (entrainment) adds additional 28% to the volume transport.

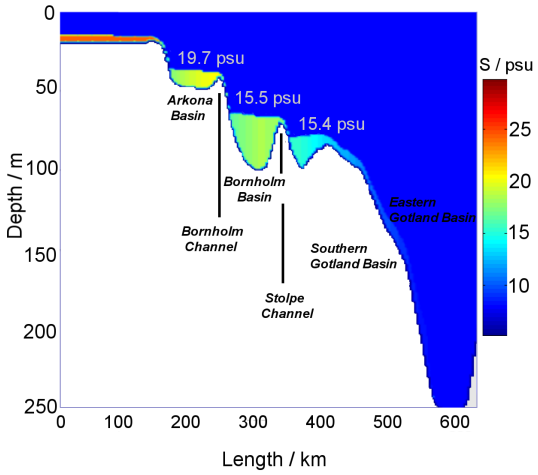

Figure 1.3: Slice from south of Drodgen Sill trough the Arkona Basin up to the Gotland Basin. Picture showing the result of an idealized simulation of the Arkona inflow event with the 2D two layer model after 30days.

On the basis of this importance the QuantAS-Off project (Quantification of water mass transformations in the Arkona Sea) has the task to investigate possible additional mixing in the Arkona Sea due to Offshore wind farms. These are planned to be build on Kriegers Shoal. The main question is how much these dense and oxygen-rich bottom currents will be obstructed and diluted by offshore wind farms. The distribution of the flux may change with consequences for the delivery of the Bornholm and Gotland Basin with oxygen-rich water. Various idealized and realistic simulations (*Janssen et al.* [2006]) with GETM (*Burchard and Bolding* [2002]) together with measurements in the Arkona Sea (*Burchard et al.* [2005]) try to understand the natural mixing processes, within the scope of the QuantAS-Nat (QuantAS - Natural processes) project. Not until further insights about natural mixing processes will have been gained, additional

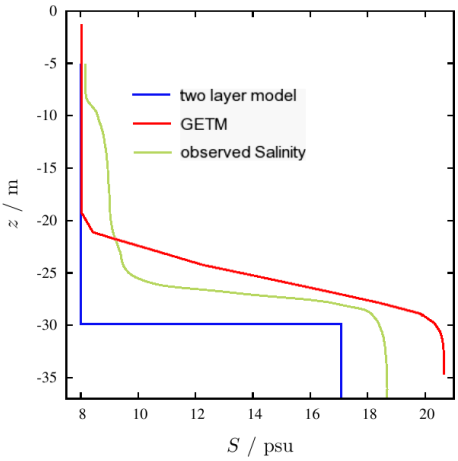

Figure 1.4: Observed (hourly averaged) and simulated salinity at a position north of Kriegers Flak during an inflow of medium-intensity dense water on Feb 7 at 4 am. Picture taken from *Burchard et al.* [2005] under addition of the two layer model result.

mixing caused by Offshore wind farms will be quantitatively estimated.
As a part of scientific research about natural mixing processes this thesis wants both to give additional information and to verify existing knowledge about water mass transformations during inflow events. Beside the development and testing of a hydrostatic and Boussinesq approximated two layer model, this thesis tries to observe plume dynamics and mixing processes during an idealized Baltic Sea inflow event. For modeling plume dynamics the Baltic Sea is assumed as a two layer system and the plume as a gravity current. A gravity current is defined as a primarily horizontal flow of a fluid within another in a gravitational field that is driven only by density difference.
Measurements in the north of Kriegers Flak (Fig. 1.4) during a medium-intensity inflow situation justify the idealized assumption of a two layer system. It is demonstrated that the saline bottom current can be considered as a well-defined current with nearly homogeneous salinity values inside the plume, bordered by the interface with high gradients for the salinity. Fig. 1.4 plots the observed salinity together with two layer model simulated salinities obtained in Chapt. 5.

This thesis is structured as follows: In the first chapter the model equations of the two layer model are derived and terms are explained. The second chapter shows the numerical implementation and the discretisation of the model equations. The third chapter deals with validation of the model equations while some analytical solutions (e.g. internal waves) are compared with the two layer model results. Furthermore some test cases like the lock exchange experiment are implemented. Idealized experiments demonstrate basic properties of gravity currents and consequently are helpful for further interpretations of more complex model results. The fifth chapter covers the simulation of the idealized Baltic Sea inflow event and the comparison to observational

data and simulations of the three-dimensional estuarine ocean model GETM (*Burchard and Bolding* [2002]).

Chapter 2

Theory

During the following sections the ocean is considered as a two layer system with two active and boussinesq-approximated fluids both being hydrostatic and incompressible. The dynamic equations for horizontal velocities are vertically but not horizontally integrated:

$$\begin{aligned} u_1 &= \frac{1}{h_1}\int_{-H}^{\eta_1} u \mathrm{d}z, \\ u_2 &= \frac{1}{h_2}\int_{\eta_1}^{\eta_2} u \mathrm{d}z, \end{aligned} \tag{2.1}$$

with u_1, u_2 being the mean velocities in upper and lower layer, u the horizontal velocity component, h_1, h_2 the thickness of lower and upper layer and the depth H. The two layer model has two active layers and uses the reduced gravity formulation. The model domain is being implemented in Cartesian coordinates and variation of the Coriolis parameter is neglected. A drying and flooding algorithm is being implemented that easily allows to split and merge the active lower layer (plume) due to topographic barriers. Turbulent exchange between upper and lower layer is modeled with the entrainment approach (Sect. 2.2.5), meaning that transport of mass and momentum from the upper into the lower layer occurs because of turbulent mixing.
First of all, the model equations are derived for the 2D two layer case. Chapt. 2.4 points out how the 2D model is expanded to 3D to reproduce plumes on complex bathymetry (see Chapt. 5).

2.1 Notation

The notation used for differentiation is written in the following form:
Partial derivatives are given by ∂, e.g. ∂_x with respect to the spatial coordinate x or ∂_t with respect to time. Other notations are in common form or explained in the text when applied.

2.2 2D two layer model equations

In this chapter the general two layer model equations are derived. Under utilization of the incompressibility condition (2.9), the hydrostatic approximation (2.21), the momentum equation without rotation (2.20) and the boundary conditions for surface and bottom (2.11), (2.24) the vertically integrated model equations are formulated. The derived equations for conservation of mass and momentum are summarized in Sect. 2.3.

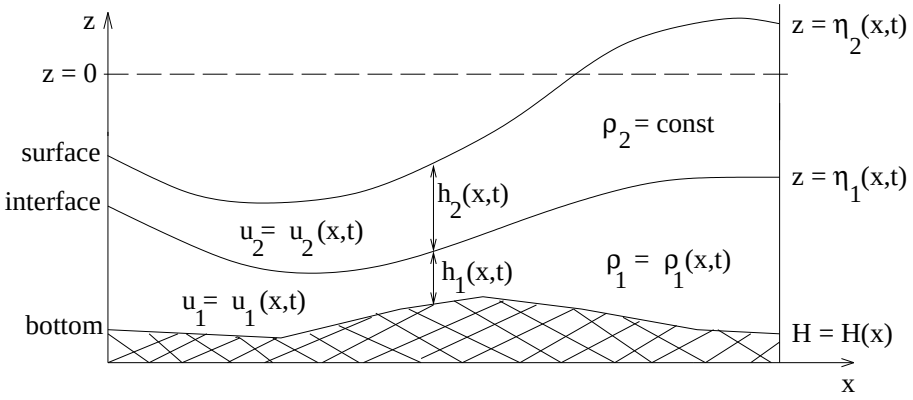

Figure 2.1: Schematic illustration of two-layer model

Let us denote the horizontal coordinate by x and the vertical coordinate by z. Let t be the time and ϱ_1 the density of the lower layer and ϱ_2 the density of the upper layer. The density of the upper layer ϱ_2 is constant and independent of time and space. The density of the lower layer ϱ_1 is a function of the horizontal coordinate x and the time t. This spatial dependency of ϱ_1 is needed to reproduce mixing in the plume with the help of the entrainment formulation (2.62) and reproduce dynamics due to horizontal density gradients:

$$\begin{array}{lrcl} \text{Upper layer:} & \varrho_2 & = & \text{const}, \\ \text{Lower layer:} & \varrho_1 & = & \varrho_1(x,t), \\ \text{with:} & \varrho_2 & < & \varrho_1. \end{array} \tag{2.2}$$

The relation $\varrho_2 < \varrho_1$ is guaranteed because of the conservative dilution (3.29) of lower layer water with upper layer water.
Because of the variable bottom topography the depth H is a function of the horizontal coordinate x:

$$H = H(x). \tag{2.3}$$

The thickness of the lower layer h_1 and the upper layer h_2 are functions of the horizontal coordinate x and the time t:

$$\begin{array}{ll} h_1 & = h_1(x,t), \\ h_2 & = h_2(x,t). \end{array} \tag{2.4}$$

The interface elevation η_1 and the surface elevation η_2 are the following:

$$\begin{aligned} \eta_1 &= \eta_1(x,t), \\ \eta_2 &= \eta_2(x,t), \end{aligned} \tag{2.5}$$

with the following relation between η_1, η_2 and h_1, h_2:

$$\begin{aligned} h_1(x,t) &= \eta_1(x,t) + H(x), \\ h_2(x,t) &= \eta_1(x,t) - \eta_2(x,t). \end{aligned} \tag{2.6}$$

The variables of the two layer model are shown in Fig. 2.1. The velocities in upper and lower layer:

$$\begin{aligned} u_1 &= u_1(x,t), \\ u_2 &= u_2(x,t), \end{aligned} \tag{2.7}$$

are obtained by calculating vertically integrated transports U_1 and U_2 in upper and lower layer in spatial x direction.:

$$\begin{aligned} u_1 h_1 = U_1(x,t) &= \int_H^{\eta_1} u \mathrm{d}z, \\ u_2 h_2 = U_2(x,t) &= \int_{\eta_1}^{\eta_2} u \mathrm{d}z. \end{aligned} \tag{2.8}$$

The solution of the two layer model equations allows to simulate a time-dependent, horizontal two-dimensional bottom current. The bottom current is considered as dense bottom water surrounded by an active upper layer with constant density.

2.2.1 Derivation of dynamic equations for surface and interface

The mathematical description of incompressibility is, with u being the horizontal velocity component and w being the vertical velocity component:

$$\partial_x u + \partial_z w = 0, \tag{2.9}$$

which can be transformed by integration over the lower layer into:

$$\int_{-H}^{\eta_1} \partial_x u \mathrm{d}z + w(\eta_1) - w(-H) = 0. \tag{2.10}$$

The kinematic boundary conditions for the surface and the bottom result from the requirement that the particles propagating close to the boundaries the boundaries are not allowed to move through the boundaries, but along these boundaries:

$$\begin{array}{lrcl} \text{Bottom:} & w(-H) &=& -u(-H)\partial_x H, \\ \text{Interface:} & w(\eta_2) &=& \partial_t \eta_2 + u(\eta_2)\partial_x \eta_2, \\ \text{Surface:} & w(\eta_1) &=& \partial_t \eta_1 + u(\eta_1)\partial_x \eta_1. \end{array} \tag{2.11}$$

We see in (2.11) that there will be no flow through the bottom. In the case of a flat bottom with $\partial_x H = 0$ there will be no vertical velocity $w(-H) = 0$ directly at the bottom.
With equations (2.10) and (2.11) we can write the following:

$$\int_{-H}^{\eta_1} \partial_x u \mathrm{d}z + \partial_t \eta_1 + u(\eta_1)\partial_x \eta_1 + u(-H)\partial_x H = 0 \tag{2.12}$$

After applying the Leibniz-Rule (*Bronstein and Semendjajew* [1984]), the partial derivative ∂_x in the integral in equation (2.12) can be written outside the integral and the following additional terms are obtained:

$$\partial_x \int_{-H(x)}^{\eta_1(x,t)} u \mathrm{d}z - \underbrace{\partial_x \eta_1 u(\eta_1)}_{\text{(i)}} - \underbrace{\partial_x H u(-H)}_{\text{(j)}} + \partial_t \eta_1 + \underbrace{u(\eta_1)\partial_x \eta_1}_{\text{(ii)}} + \underbrace{u(-H)\partial_x H}_{\text{(jj)}} = 0 \tag{2.13}$$

We see that (i) and (ii) as well as (j) and (jj) in (2.13) cancel out each other:

$$-\partial_x \int_{-H}^{\eta_1} u \mathrm{d}z = \partial_t \eta_1. \tag{2.14}$$

To get the dynamic equations for the surface- and interface elevation we define for the horizontal velocity component u_1 in the lower layer:

$$u_1 = \frac{1}{\eta_1 + H} \int_{-H}^{\eta_1} u \mathrm{d}z = \frac{1}{h_1} \int_{-H}^{\eta_1} u \mathrm{d}z, \tag{2.15}$$

so that we obtain, with U_1 being the vertically integrated transport in the lower layer:

$$h_1 u_1 = U_1 = \int_{-H}^{\eta_1} u \mathrm{d}z, \tag{2.16}$$

which we can use together with (2.14) to get the dynamic equation for the interface elevation:

$$\partial_t \eta_1 = -\partial_x (h_1 u_1). \tag{2.17}$$

The same procedure applied to the surface layer will lead us to the dynamic equation for the surface elevation:

$$\partial_t \eta_2 = \partial_t \eta_1 - \partial_x (h_2 u_2) = -\partial_x (h_1 u_1) - \partial_x (h_2 u_2), \tag{2.18}$$

with u_2 being the horizontal vertically integrated velocity in the upper layer:

$$u_2 h_2 = U_2(x,t) \quad = \int_{\eta_1}^{\eta_2} u \mathrm{d}z \tag{2.19}$$

and U_2 the vertically integrated transport in the upper layer.

2.2.2 Dynamic equations for horizontal velocities

Derivation of equation of horizontal velocity u_2 in upper layer

The momentum equation without rotation for an inviscid, incompressible and immiscible fluid in spatial $x-$ and $z-$direction can be written as:

$$\partial_t u + \partial_x u^2 + \partial_z (wu) + \partial_z \tau = -\frac{1}{\varrho_0} \partial_x p, \tag{2.20}$$

where ϱ_0 is the constant reference density, $\partial_x p$ the pressure gradient and τ the vertical shear stress normalized by mean density.
Furthermore the hydrostatic approximation is used:

$$\partial_z p = -g\varrho, \tag{2.21}$$

where p is the pressure, g the gravitational acceleration and ϱ the density.
Integration of (2.21) between z and η_2 leads to:

$$p(\eta_2) - p(z) = -g \int_z^{\eta_2} \varrho \mathrm{d}z, \tag{2.22}$$

and differentiation of (2.22) with respect to x:

$$\partial_x p(\eta_2) - \partial_x p = -g \partial_x \int_z^{\eta_2} \varrho \mathrm{d}z. \tag{2.23}$$

The term $\partial_x p(\eta_2)$ is the atmospheric pressure gradient which is neglected here:

$$\partial_x p(\eta_2) = 0. \tag{2.24}$$

Let us now divide (2.23) by the reference density ϱ_0:

$$-\frac{1}{\varrho_0} \partial_x p = -\frac{g}{\varrho_0} \partial_x \int_z^{\eta_2} \varrho \mathrm{d}z. \tag{2.25}$$

Equation (2.20) together with (2.25) results in the dynamic equation for the horizontal velocity component:

$$\partial_t u + \partial_x u^2 + \partial_z (wu) + \partial_z \tau = -\frac{g}{\varrho_0} \partial_x \int_z^{\eta_2} \varrho \mathrm{d}z. \tag{2.26}$$

Equation (2.26) is being integrated from η_1 to η_2 to obtain a transport equation for the vertically averaged momentum in the upper layer:

$$\begin{aligned}
&\underbrace{\int_{\eta_1}^{\eta_2} \partial_t u \mathrm{d}z}_{\mathrm{i}} + \underbrace{\int_{\eta_1}^{\eta_2} \partial_x u^2 \mathrm{d}z}_{\mathrm{j}} + \underbrace{w(\eta_2)}_{\mathrm{k}} u(\eta_2) - \underbrace{w(\eta_1)}_{\mathrm{l}} u(\eta_1) + \tau_s - \tau_i \\
&= -\frac{g}{\varrho_0} \int_{\eta_1}^{\eta_2} \partial_x \int_z^{\eta_2} \varrho_2 \mathrm{d}z\mathrm{d}z \\
&= -\frac{g}{\varrho_0} \int_{\eta_1}^{\eta_2} \partial_x \eta_2 \varrho_2 \mathrm{d}z \\
&= -\frac{g}{\varrho_0} h_2 \varrho_2 \partial_x \eta_2,
\end{aligned} \tag{2.27}$$

where τ_s is the surface stress and τ_i the interfacial stress and $\varrho(z) = \varrho_2 = \text{const}$ for $\eta_1 \leq z \leq \eta_2$. Now equation (2.27) is simplified under use of the Leibnitz-Rule (*Bronstein and Semendjajew* [1984]) for terms i and j in (2.27). The kinematic boundary conditions (2.11) are used for terms k and l in (2.27) and the reference density ϱ_0 is set equal to ϱ_2:

$$\begin{aligned}
&\partial_t \int_{\eta_1}^{\eta_2} u \mathrm{d}z - \underbrace{\partial_t \eta_2 u(\eta_2)}_{\mathrm{m}} + \underbrace{\partial_t \eta_1 u(\eta_1)}_{\mathrm{n}} \\
&+\partial_x \int_{\eta_1}^{\eta_2} u^2 \mathrm{d}z - \underbrace{\partial_x \eta_2 u^2(\eta_2)}_{\mathrm{o}} + \underbrace{\partial_x \eta_1 u^2(\eta_1)}_{\mathrm{p}} \\
&+ \underbrace{(\partial_t \eta_2 + u(\eta_2)\partial_x \eta_2) u(\eta_2)}_{\mathrm{q}} - \underbrace{(\partial_t \eta_1 + u(\eta_1)\partial_x \eta_1) u(\eta_1)}_{\mathrm{r}} \\
&+\tau_s - \tau_i \\
&= -g h_2 \partial_x \eta_2
\end{aligned} \tag{2.28}$$

Terms m, n, o, p, q and r cancel out each other in 2.28:

$$\partial_t \int_{\eta_1}^{\eta_2} u \mathrm{d}z + \partial_x \int_{\eta_1}^{\eta_2} u^2 \mathrm{d}z + \tau_s - \tau_i = -g h_2 \partial_x \eta_2 \tag{2.29}$$

With the approximation $u = u_2$ being constant with respect to the spatial coordinate z for $\eta_1 \leq z \leq \eta_2$ we obtain:

$$\int_{\eta_1}^{\eta_2} u^2 \mathrm{d}z = h_2 u_2^2, \tag{2.30}$$

what means that homogeneous horizontal velocity is assumed within the upper layer as well as for the lower layer. As a consequence, the two layer model equations are dealing with mean velocities in the upper and lower layer. Hence all processes due to

velocity gradients take place at the interface. Finally we get the conservative momentum equation for u_2:

$$\partial_t(h_2 u_2) + \partial_x\left(h_2 u_2^2\right) + \tau_s - \tau_i = -g h_2 \partial_x \eta_2. \tag{2.31}$$

where conservative means that this equation is momentum conserving in contrast to the differential form (2.36) derived below.
To get the differential form of equation (2.31) some further mathematical manipulations are needed. With the rules of differential calculus we have:

$$h_2\partial_t u_2 + u_2\partial_t h_2 + h_2 u_2 \partial_x u_2 + u_2\partial_x(h_2 u_2) + \tau_s - \tau_i = -g h_2 \partial_x \eta_2, \tag{2.32}$$

and the differentiation $\partial_t h_2$ results in the following:

$$\partial_t h_2 = \partial_t(\eta_2 - \eta_1) = \partial_t \eta_2 - \partial_t \eta_1. \tag{2.33}$$

Let us now use the dynamic equation for the interface elevation (2.17) and the surface elevation (2.18) together with (2.33):

$$\partial_t h_2 = -\partial_x(h_1 u_1) - \partial_x(h_2 u_2) + \partial_x(h_1 u_1) = -\partial_x(h_2 u_2). \tag{2.34}$$

Equations (2.32) and (2.34) can be transformed into the relation:

$$h_2\partial_t u_2 + h_2 u_2 \partial_x u_2 + \tau_s - \tau_i = -g h_2 \partial x \eta_2. \tag{2.35}$$

After division of (2.35) by h_2 and adding the horizontal momentum diffusion term we will get the differential equation for the horizontal velocity component u_2 in the upper layer:

$$\partial_t u_2 + u_2\partial_x u_2 - \partial_x(A_H \partial_x u_2) + \frac{\tau_s}{h_2} - \frac{\tau_i}{h_2} = -g\partial_x \eta_2, \tag{2.36}$$

with A_H being the horizontal momentum diffusion coefficient.

Derivation of equation of horizontal velocity u_1 in lower layer

Now we will derive the equation for u_1 with the help of (2.26). The integration of (2.26) within the borders of $-H$ and η_1 will lead to the differential form of the dynamic equation for the horizontal velocity component u_1 in the lower layer. We set $\varrho_0 = \varrho_2$ (see also 2.27) and use the reduced gravity $g^{'}$ which is:

$$g^{'} = g(\varrho_1 - \varrho_2)/\varrho_2. \tag{2.37}$$

For the implementation of Entrainment (see section 2.2.5) that is the mixing between the turbulent bottom current and the ambient water and hence transport of mass and momentum due to production of turbulent kinetic energy or shear strain at the interface, the density of the lower layer has to be a function of the spatial coordinate x and time t: $\varrho_1 = \varrho_1(x,t)$. The density ϱ_2 in the upper layer remains constant (2.2):

$$
\begin{aligned}
&\underbrace{\int_{-H}^{\eta_1} \partial_t u \mathrm{d}z}_{i} + \underbrace{\int_{-H}^{\eta_1} \partial_x u^2 \mathrm{z}}_{j} + \underbrace{w(\eta_1)}_{k} u(\eta_1) - \underbrace{w(-H)}_{l} u(-H) + \tau_i - \tau_b \\
&= -\frac{g}{\varrho_0} \int_{-H}^{\eta_1} \partial_x \int_z^{\eta_2} \varrho \mathrm{d}z \mathrm{d}z \\
&= -\frac{g}{\varrho_0} \int_{-H}^{\eta_1} \partial_x \left(\int_z^{\eta_1} \varrho_1 dz + \int_{\eta_1}^{\eta_2} \varrho_2 dz \right) \mathrm{d}z \\
&= -\frac{g}{\varrho_0} \int_{-H}^{\eta_1} \partial_x ((\eta_1 - z)\varrho_1 + (\eta_2 - \eta_1)\varrho_2) \mathrm{d}z \\
&= -\frac{g}{\varrho_0} \int_{-H}^{\eta_1} (\eta_1 \partial_x \varrho_1 + \varrho_1 \partial_x \eta_1 - z\partial_x \varrho_1 + \varrho_2 \partial_x \eta_2 - \varrho_2 \partial_x \eta_1) \mathrm{d}z \\
&= -\frac{g}{\varrho_0} h_1(\varrho_1 - \varrho_2)\partial_x \eta_1 - \frac{g}{\varrho_0} h_1 \varrho_2 \partial_x \eta_2 + \frac{g}{2\varrho_0} \partial_x \varrho_1 (\eta_1^2 - H^2) - \frac{g}{\varrho_0} \eta_1 \partial_x \varrho_1 (\eta_1 + H) \\
&= -g^{'} h_1 \partial_x \eta_1 - g h_1 \partial_x \eta_2 - \frac{g}{\varrho_2} \frac{h_1^2}{2} \partial_x \varrho_1,
\end{aligned}
\tag{2.38}
$$

with τ_i being the interfacial stress and τ_b being the bottom stress.
Under use of some algebraic transformations with the help of the Leibniz-Rule (*Bronstein and Semendjajew* [1984]) and the boundary conditions (2.11) for the terms i, j, k and l in (2.38), we can write down the equation for u_1, the horizontal velocity component in the lower layer, in analogy to equation (2.36) for the horizontal velocity component u_2 in the upper layer in differential form. Additionally the horizontal momentum diffusion term is inserted:

$$
\partial_t u_1 + u_1 \partial_x u_1 - \partial_x (A_H \partial_x u_1) + \frac{\tau_i}{h_1} - \frac{\tau_b}{h_1} = -g^{'} \partial_x \eta_1 - g \partial_x \eta_2 - \frac{g}{\varrho_2} \frac{h_1}{2} \partial_x \varrho_1 \tag{2.39}
$$

and for constant density $\partial_x \varrho_1 = \partial_x \varrho_1 = 0$:

$$
\partial_t u_1 + u_1 \partial_x u_1 - \partial_x (A_H \partial_x u_1) + \frac{\tau_i}{h_1} - \frac{\tau_b}{h_1} = -g^{'} \partial_x \eta_1 - g \partial_x \eta_2 \tag{2.40}
$$

2.2.3 Bottom friction

The bottom friction obeys the quadratic friction law (e.g. *Simons* [1980]):

$$
\tau_b \quad = C_D \mid u_1 \mid u_1, \tag{2.41}
$$

with C_D being the dimensionless bottom drag coefficient. There are different estimations of the bottom drag coefficient with for example the widely used value of 0.0025

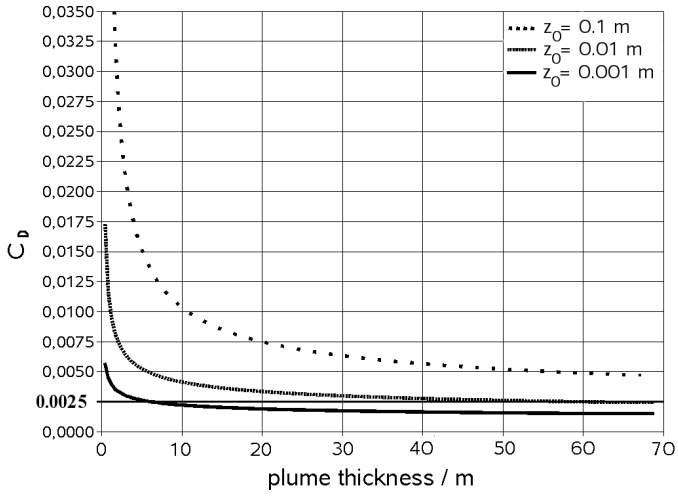

Figure 2.2: Diagram showing the range of the bottom drag coefficient under assumption of the logarithmic law for the velocity profile at the bottom.

in circulation models (*Simons* [1980]; *Backhaus* [1985]) up to values of 0.03 for dense bottom currents (*Bowden* [1960]) and 0.15 for the simulation of an overflow (*Smith* [1975]).
Another attempt is to calculate the bottom stress under the assumption of the logarithmic law (Fig. 2.2 *Baumert et al.* [1989]) for the whole lower layer:

$$u(z) - u(0) = \frac{u_*}{\kappa} \ln\left(\frac{z + z_0}{z_0}\right), \tag{2.42}$$

with $u(0) = 0$, u_* being the friction velocity, z_0 the bottom roughness length with typical values of 1 mm and κ the Karman constant ($\kappa = 0.4$) which arises in wall turbulence and is experimentally determined.
The bottom stress τ_b is linked with the friction velocity u_* by:

$$\tau_b := u_*^2 \tag{2.43}$$

whereas:

$$u_*^2 = u^2 C_D \tag{2.44}$$

In addition the following is obtained with the help of (2.42):

$$\tau_b \quad = u^2(z) \underbrace{\frac{\kappa^2}{ln^2(\frac{z+z_0}{z_0})}}_{C_D} \tag{2.45}$$

Hence the bottom drag coefficient is calculated by:

$$C_D = \frac{\tau_b}{u^2} = \frac{\kappa^2}{ln^2\left(\frac{z+z_0}{z_0}\right)}. \tag{2.46}$$

Integration over (2.42) gives the following assumption for the thickness of the logarithmic bottom layer:

$$2z = h_1. \tag{2.47}$$

For the limit of low bottom layer thickness the bottom drag coefficient is infinite:

$$\lim_{z\to 0} C_d = \infty. \tag{2.48}$$

Hence the velocity has the following physically expected relationship to the layer thickness:

$$\lim_{z\to 0} u_1 = 0. \tag{2.49}$$

The widely used value of 0.0025 (*Simons* [1980]; *Backhaus* [1985]) for the bottom drag coefficient can be found for values of $h_1 \approx 5$ m of the lower layer (see Fig. 2.2). Fig. 2.2 plots the bottom drag coefficient as a function of the bottom roughness z_0 with values of $z_0 = 0.001, 0.01 \text{and} 0.1$. With higher values of the bottom roughness length the bottom drag coefficient is increasing. In case of the Arkona inflow event (Chapt. 5) with simulated, mean plume thicknesses between 5 m and 10 m the geostrophic balance of the bottom flow would be significantly modulated by bottom friction under bottom roughness lengths of 1 cm. Thus this would result in a propagation down the slope with bottom mean bottom drag coefficients nearly six times higher for bottom roughness lengths of 1 cm compared with $z_0 = 0.001$. Experiments made with the 3D two layer model (see Fig. 5.8) and different assumptions for the bottom drag coefficient with $C_D = 0.0025$ and the calculation under use of the logarithmic law, have shown that the differences are small. In consideration of the fact that the logarithmic law is a more physical assumption, it is maintained for further simulations. Furthermore under use of the logarithmic law, the bottom roughness length is included and may be changing due to different sediment properties and small scale topographic features. Simulations under conditions of different soil conditions are not made within this thesis.

2.2.4 Horizontal density advection

The horizontal advection of density, respectively salinity, is obtained by solving the continuity equation which is:

$$\frac{\partial \varrho}{\partial t} + \vec{\Delta}(\varrho \vec{u}) \quad = 0 \tag{2.50}$$

with $\vec{u}$ being the current velocity (2.53) and $\varrho = \varrho_1$ the density in the lower layer.
The surface water of the Arkona Sea can be assumed to consist of water with mean

salinity values around 8 psu . This value is proved by observational data (*Burchard et al.* [2005]; *Liljebladh and Stigebrandt* [1996]). Thus the process of horizonal advection of density in the upper layer is assumed to be negligible (2.2).
Hence the horizontal advection of density in the lower layer is formulated by the following equation:

$$\frac{\partial h_1 \varrho_1}{\partial_t} + \frac{\partial u_1 h_1 \varrho_1}{\partial_x} = 0. \tag{2.51}$$

This equation can be verified when applying ϱ =constant to (2.51). By doing so equation (2.63) is obtained with $\partial_t h_1 = \partial_t \eta_1$.

2.2.5 Entrainment

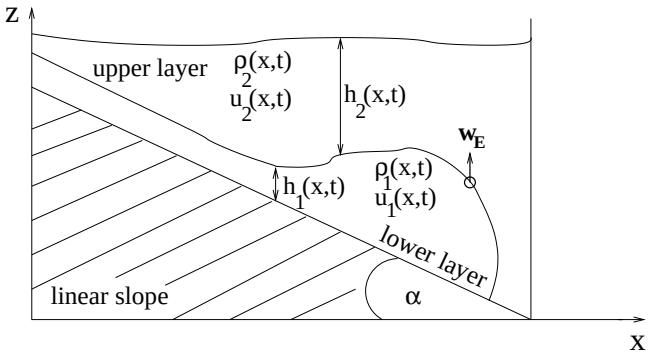

Figure 2.3: The entrainment velocity w_E or the entrainment process itself will cause fluxes of mass and momentum through the interface. The entrainment rate E depends on the local values as the current velocity u_1, the density difference between upper and lower layer and the thickness of the lower layer h_1.

The entrainment process Entrainment (e.g. *Turner* [1973])in case of the two layer model is the turbulent mixing process of the upper layer into the lower layer. The opposite of entrainment is detrainment that is not being implemented into this two layer model. The state of the four variables velocity u_1, v_1, height of the lower layer h_1, bottom friction and density difference between upper and lower layer define the entrainment rate E:

$$E = \frac{w_E}{\mid \vec{u} \mid} \tag{2.52}$$

with w_E being the entrainment velocity in spatial $z-$direction (Fig. 2.3) and $\mid \vec{u} \mid$ the current speed. This relation assumes that the rate of entrainment E is proportional to the current speed $\mid \vec{u} \mid$:

$$\mid \vec{u}_1 \mid = \sqrt{u_1^2 + v_1^2}. \tag{2.53}$$

Production of turbulent kinetic energy due to bottom friction and shear strain produces a flux of mass and momentum from the upper layer into the lower layer. Thus the increasing thickness h_1 of the lower layer will lead to higher values of the potential energy (*Oguz et al.* [1990]).
Generally the entrainment is a bulk characterization of the turbulent mixing against the stabilizing effects of stratification and can be explained as a function of the *Froude* number (*Kundu and Cohen* [1997]):

$$Fr = \frac{\mid \vec{u}_1 \mid}{\sqrt{g^{'} h_1}}. \tag{2.54}$$

The entrainment concept was developed by G.I. Taylor during investigations of ascending gases in the layered atmosphere (*Turner* [1986]). The concept of entrainment (2.52) with the entrainment rate E depending on the current speed has been applied with the work of *Ellison and Turner* [1959] for a dense bottom current on a slope. During laboratory experiments *Ellison and Turner* [1959] has shown that E is a function of the Richardson number, that is for a two layer situation defined as:

$$R_i = \frac{g^{'} h_1}{(\mid \vec{u} \mid)^2} \tag{2.55}$$

which expresses the ratio of potential to kinetic energy (*Kundu and Cohen* [1997]). The reciprocal of the square root of the Richardson number is the Froude number. The assumption of a simple linear relation between entrainment parameter and slope angle α has been suggested by *Bo Pedersen* [1980a]:

$$E \quad = c_p \sin \alpha \tag{2.56}$$

with c_p being experimentally determined ($c_p = 0.072$, see *Bo Pedersen* [1980a]; *Buch* [1982]) under the condition that $\sin \alpha < 0.01$. For a hade of $\alpha = 0.5°$, which is a realistic value for a steep continental slope, this assumption is justified. Furthermore *Bo Pedersen* [1980a] has shown that for a balance between downhill-slope force and bottom friction the following relation is obtained:

$$E = c_p C_D Fr^2 = \frac{c_p C_D}{R_i}. \tag{2.57}$$

Due to the fact that the Coriolis force plays a significant role for oceanographic flows, this assumption has been proved to be also a satisfying approximation for flows driven by the Coriolis force (*Bo Pedersen* [1980b]).
Many studies implicate greater complexity in the entrainment process of gravity currents than it is contained in the entrainment models only depending on the *Froude* number. Various dependencies of the entrainment rate on for example the ambient stratification (*Baines* [2001]) or wave breaking (*Cenedese et al.* [2004]) do exist. Additionally relations between hydraulic control points and entrainment have been carried

out (*Hornung et al.* [1995]) whereas the effect of hydraulic jumps is only poorly understood for rotational systems (*Pratt* [1987]).
The work of *Arneborg et al.* [2005] tries to obtain an entrainment formulation taking the Coriolis force into account. With a 19 hour of obtained time series of dissipation, stratification and horizontal velocities for a dense gravity current propagating into the Arkona Basin, solutions of the 1D turbulence model GOTM (*Umlauf et al.* [2005]) have been validated against observations (*Arneborg et al.* [2005]). The main dynamics for the dense gravity current are explained by simple one-dimensional theory whereas the gravitational term in the dynamic equations is balanced by bottom friction and the Coriolis force is balanced by a cross-flow pressure gradient. After insertion of the vertically integrated parameters for the simple geometry and under use of some assumptions (mild slope, quasi-geostrophic) the Froude (2.54) and the Ekman number K:

$$K = \frac{C_D \mid \vec{u}_1 \mid}{f h_1} \tag{2.58}$$

which symbolizes the relation between the height of the Ekman layer and the thickness of the gravity current, are obtained. The relation between the entrainment parameter E, Fr and Rf is as follows:

$$E = 2 C_D Rf Fr^2 \tag{2.59}$$

with Rf the bulk flux Richardson number being the ratio between shear production P and buoyancy production B:

$$Rf = \frac{B}{P}. \tag{2.60}$$

(2.59) assumes the entrainment is a function of bottom drag coefficient C_D, bulk flux Richardson number and known Froude number. C_D is assumed to be constant. The flux Richardson number is estimated with the help of turbulence measurements from a vertically profiled plume. With a high resolution turbulence model, these observations have been reproduced quite well. Then the simple model with the integrated parameters is used to simulate various idealized scenarios. With the help of a fitting procedure the following relation between flux Richardson number Rf, Froude number Fr and Ekman number K is obtained (Fig. 2.4):

$$Rf = 0.044 Fr^{0.77} K^{0.67}. \tag{2.61}$$

Thus with a combination of (2.59) with (2.61) the entrainment rate is formulated by:

$$E \quad = \frac{w_E}{\mid \vec{u}_1 \mid} = 0.008 C_D Fr^{2.77} K^{0.67} \tag{2.62}$$

The advantage of the entrainment rate model by *Arneborg et al.* [2005] especially for this two layer model is that it has been validated by a process study in the Arkona Basin and the simulation of the Arkona inflow event is a final goal of this thesis.
It must be noted that the non-dimensional parameter E has proved very useful as a

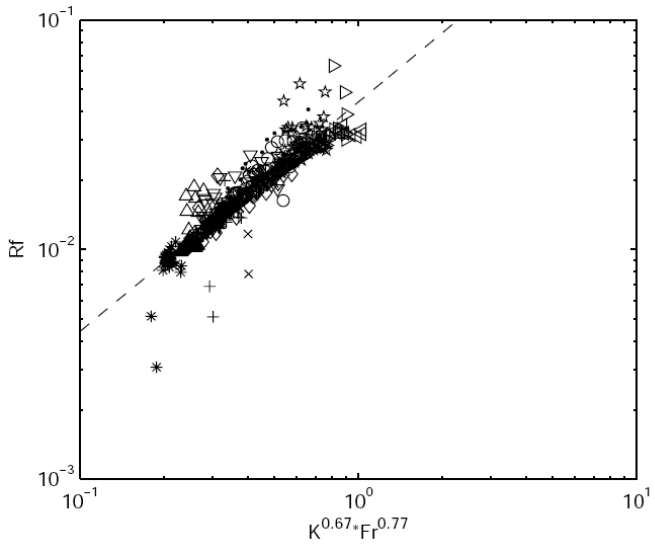

Figure 2.4: The bulk flux Richardson number as a function of a nonlinear combination of Froude and Ekman number: $K^{0.67}Fr^{0.77}$. The dashed line is the function. Picture taken from *Arneborg et al.* [2005]

modeling and parametrisation tool for the characterization of mixing in inhomogeneous systems.

2.3 Summary of 2D model equations

The dynamic equations for the surface and interface elevation are :

$$\begin{aligned} \partial_t \eta_1 &= -\partial_x(h_1 u_1) \\ \partial_t \eta_2 &= -\partial_x(h_1 u_1) - \partial_x(h_2 u_2) \end{aligned} \tag{2.63}$$

and for the dynamic equations of motion for vertically integrated velocity u_1 and u_2 the differential form:

$$\begin{aligned} \partial_t u_1 + \underbrace{\partial_x u_1^2}_{ADV} - \underbrace{C_D \mid u_1 \mid \frac{u_1}{h_1}}_{FRIC} - \underbrace{\partial_x(A_H \partial_x u_1)}_{DIFF} &= - \underbrace{g^{'} \partial_x \eta_1}_{PRESSI} - \underbrace{g \partial_x \eta_2}_{PRESSE} - \underbrace{\frac{g}{\varrho_2}\frac{h_1}{2}\partial_x \varrho_1}_{RHO} \\ \partial_t u_2 + \partial_x u_2^2 - \partial_x(A_H \partial_x u_2) &= -g \partial_x \eta_2 \end{aligned} \tag{2.64}$$

with ADV being the term for horizontal momentum advection, $FRIC$ the term due to bottom friction, $DIFF$ the horizontal momentum diffusion term, $PRESSI$ the internal pressure gradient term, $PRESSE$ the external pressure gradient term and RHO the term that describes dynamics due to horizontal density gradients within the lower layer. Thus the conservative form with vertically integrated transports is:

$$\begin{aligned} \partial_t(U_1) + \partial_x(u_1^2 h_1) - h_1 C_D \mid u_1 \mid \frac{u_1}{h_1} - \partial_x(A_H \partial_x U_1) &= -g^{'} h_1 \partial_x \eta_1 - g h_1 \partial_x \eta_2 - \frac{g}{\varrho_2}\frac{h_1^2}{2}\partial_x \varrho_1 \\ \partial_t(U_2) + \partial_x(u_2^2 h_2) - \partial_x(A_H \partial_x U_2) &= -g h_2 \partial_x \eta_2 \end{aligned} \tag{2.65}$$

with U_1, U_2 being the vertically integrated transports in the upper and lower layer:

$$\begin{aligned} U_1 &= u_1 h_1 \\ U_2 &= u_2 h_2 \end{aligned} \tag{2.66}$$

2.4 3D two layer model equations

In this section the two layer model equations for the 3D case are given. With the help of (2.63) and (2.65) the model equations are extended under conclusion by analogy. Hence all terms of the 2D model equations and the additional mixed terms for advective and diffusive processes are inserted. For the Coriolis force the Coriolis parameter $f = 2\ \Omega\ \sin\alpha = 0.0001 s^{-1}$ with the angular velocity $\Omega = 0.73 \cdot 10^{-4}\ \mathrm{s}^{-1}$ and latitude $\alpha \cong 55°$ is used.

2.4.1 Dynamic equations for surface and interface

With reference to (2.63) the dynamic equations for surface and interface elevation are:

$$\begin{aligned} \partial_t \eta_1 &= -\partial_x(h_1 u_1) - \partial_y(h_1 v_1) \\ \partial_t \eta_2 &= -\partial_x(h_1 u_1) - \partial_x(h_2 u_2) - \partial_y(h_1 v_1) - \partial_y(h_2 v_2) \end{aligned} \tag{2.67}$$

with the additional terms $-\partial_y(h_1 v_1)$ and $-\partial_y(h_2 v_2)$ for the spatial $y-$direction.

2.4.2 Bottom friction

The bottom friction for the 3D two layer model simply applies to the second horizontal coordinate y the same way as (2.41) in spatial $x-$direction and can be written as:

$$\begin{aligned} \tau_b^x &= C_D \mid u_1 \mid u_1, \\ \tau_b^y &= C_D \mid v_1 \mid v_1, \end{aligned} \tag{2.68}$$

2.4.3 Horizontal density advection

The horizontal density advection for the 3D case according to (2.51) is as follows:

$$\frac{\partial h_1 \varrho_1}{\partial_t} + \frac{\partial u_1 h_1 \varrho_1}{\partial_x} + \frac{\partial v_1 h_1 \varrho_1}{\partial_y} = 0 \tag{2.69}$$

2.4.4 Horizontal momentum diffusion

The horizontal momentum diffusion is formulated by the following equations representing the current speed in meridional and longitudinal direction under addition of the mixed terms:

$$\begin{aligned} \partial_t u &+ ... - \partial_x(A_H \partial_x u) - \partial_y(A_H(\partial_y u + \partial_x v)) = ... \\ \partial_t v &+ ... - \partial_y(A_H \partial_y v) - \partial_x(A_H(\partial_y u + \partial_x v)) = ... \end{aligned} \tag{2.70}$$

2.4.5 Dynamic equations for horizontal transport

Equation (2.65) together with preceding steps will give the dynamic equations for horizontal transport U_1, V_1 in lower and U_2, V_2 upper layer:

$$\begin{aligned}
\partial_t(U_1) + \partial_x(u_1^2 h_1) + \partial_y(h_1 u_1 v_1) - h_1 C_D \mid u_1 \mid \frac{u_1}{h_1} - \\
\partial_x(A_H \partial_x U_1) - \partial_y(A_H(\partial_y U_1 + \partial_x V_1)) - fV_1 &= -g^{'} h_1 \partial_x \eta_1 - g h_1 \partial_x \eta_2 - \frac{g}{\varrho_2}\frac{h_1^2}{2}\partial_x \varrho_1 \\
\partial_t(U_2) + \partial_x(u_2^2 h_2) + \partial_y(h_2 u_2 v_2) - \\
\partial_x(A_H \partial_x U_1) - \partial_y(A_H(\partial_y U_2 + \partial_x V_2)) - fV_2 &= -g h_2 \partial_x \eta_2 \\
\partial_t(V_1) + \partial_y(v_1^2 h_1) + \partial_x(h_1 u_1 v_1) - h_1 C_D \mid v_1 \mid \frac{v_1}{h_1} - \\
\partial_y(A_H \partial_y U_1) - \partial_x(A_H(\partial_y U_1 + \partial_x V_1)) + fU_1 &= -g^{'} h_1 \partial_y \eta_1 - g h_1 \partial_y \eta_2 - \frac{g}{\varrho_2}\frac{h_1^2}{2}\partial_y \varrho_1 \\
\partial_t(V_2) + \partial_y(v_2^2 h_2) + \partial_x(h_2 u_2 v_2) - \\
\partial_y(A_H \partial_y U_2) - \partial_x(A_H(\partial_y U_1 + \partial_x V_1)) + fU_2 &= -g h_2 \partial_y \eta_2
\end{aligned} \tag{2.71}$$

2.4.6 Entrainment

No changes to the entrainment formulation of (2.62) and numerical implementation has to be applied for the 3D case. Entrainment is calculated at the elevation points while the adaption of the modified transports in upper and lower layer after impact of entrainment is calculated with the median of the adjacent elevation points. The updates of density, elevation and transports are formulated as shown in 2.2.5 where the calculation of the additional parameters V_1 and V_2 for the 3D case is equivalent to the calculation of U_1 and U_2 for the 2D case due to the reason that entrainment is assumed to be a local process and can be calculated with the informations of a single water column.

2.5 Summary of 3D model equations

The dynamic equations for the surface and interface elevation are :

$$\begin{aligned} \partial_t \eta_1 &= -\partial_x(h_1 u_1) - \partial_y(h_1 v_1) \\ \partial_t \eta_2 &= -\partial_x(h_1 u_1) - \partial_x(h_2 u_2) - \partial_y(h_1 v_1) - \partial_y(h_2 v_2) \end{aligned} \tag{2.72}$$

and for the dynamic equations of motion for vertically integrated transports for the transport U_1 in the lower layer in spatial $x-$direction in conservative form:

$$\begin{aligned} &\partial_t(U_1) + \partial_x(u_1^2 h_1) + \partial_y(h_1 u_1 v_1) - h_1 C_D \mid u_1 \mid \frac{u_1}{h_1} - \\ &\partial_x(A_H \partial_x U_1) - \partial_y(A_H(\partial_y U_1 + \partial_x V_1)) - fV_1 = -g^{'} h_1 \partial_x \eta_1 - g h_1 \partial_x \eta_2 - \frac{g}{\varrho_2}\frac{h_1^2}{2}\partial_x \varrho_1, \end{aligned} \tag{2.73}$$

and for the transport U_2 in the upper layer in spatial $x-$direction:

$$\begin{aligned} &\partial_t(U_2) + \partial_x(u_2^2 h_2) + \partial_y(h_2 u_2 v_2) - \\ &\partial_x(A_H \partial_x U_1) - \partial_y(A_H(\partial_y U_2 + \partial_x V_2)) - fV_2 = -g h_2 \partial_x \eta_2. \end{aligned} \tag{2.74}$$

The vertically integrated transport V_1 in the lower layer in spatial $y-$direction in conservative form is as follows:

$$\begin{aligned} &\partial_t(V_1) + \partial_y(v_1^2 h_1) + \partial_x(h_1 u_1 v_1) - h_1 C_D \mid v_1 \mid \frac{v_1}{h_1} - \\ &\partial_y(A_H \partial_y U_1) - \partial_x(A_H(\partial_y U_1 + \partial_x V_1)) + fU_1 = -g^{'} h_1 \partial_y \eta_1 - g h_1 \partial_y \eta_2 - \frac{g}{\varrho_2}\frac{h_1^2}{2}\partial_y \varrho_1, \end{aligned} \tag{2.75}$$

and the transport V_2 in the upper layer in spatial $y-$direction in conservative form:

$$\begin{aligned} &\partial_t(V_2) + \partial_y(v_2^2 h_2) + \partial_x(h_2 u_2 v_2) - \\ &\partial_y(A_H \partial_y U_2) - \partial_x(A_H(\partial_y U_1 + \partial_x V_1)) + fU_2 = -g h_2 \partial_y \eta_2 \end{aligned} \tag{2.76}$$

Chapter 3

Numerical implementation

3.1 Discretisation and numerical implementation

The numerical solution requires the domain to be discretized while the governing equations are reduced to their finite difference equivalents. The spatial grid used for discretisation of the 2D two layer model equations is a slice through the Arakawa-C-Grid (*Mesinger and Arakawa* [1976]) presented in Fig. 3.1. This grid type belongs to a class of staggered grids not discussed here. Hence the staggered grid used for the 3D model equations is the Arakawa C grid represented by Fig. 3.2. The discrete values u_i are given on the interval interfaces. All η_i, and ϱ_i are given in the centres of these intervals.

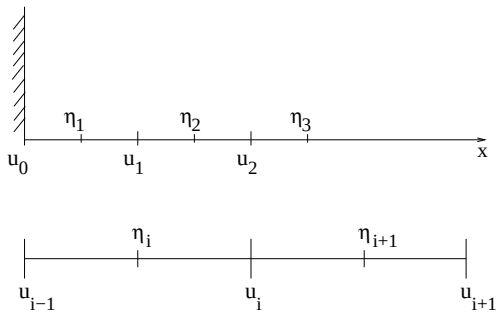

Figure 3.1: Sketch showing the staggered grid for numerical discretisation of differential equations.

This section shows how the dynamic equations, advective terms, diffusive terms and bottom friction are discretized. Some discretisations are formulated in explicit and more stable implicit form while finally the model uses, when assigned, the implicit form. The term 'explicit' denotes a scheme where all terms on the right hand side of for example equation (2.63) are evaluated at time steps n, $n-1$, ... That means that at any

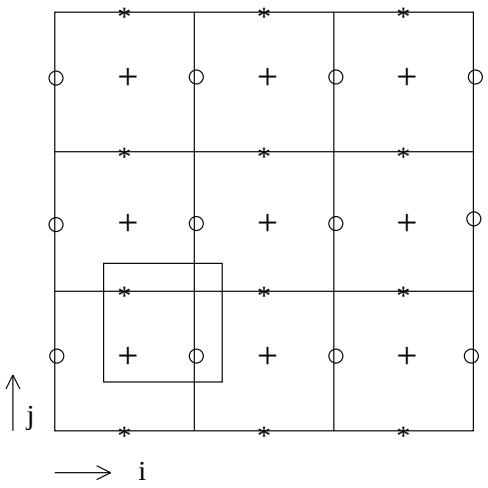

Figure 3.2: Sketch showing the staggered grid for numerical discretisation of differential equations whereas the following symbols are used: *o*: U-points; +: $\eta-$points; *: V-points. The inserted box denotes grid points with same index (i,j).

given time t^n the right hand side is known from previous time steps. 'Implicit' on the other hand is a scheme where some of the terms on the right hand side of a partial differential equation are evaluated at time step t^{n+1} and hence are not known at t^n. A solution of this 'problem' is, that one only need to transfer these unknown terms to the left hand side of the equation and invert the terms for the unknown variables with t^{n+1}. The discretisation of bottom drag for example, shown in Section 3.2.5, uses the implicit scheme.

3.2 Discretiation for the 2D two layer model

3.2.1 Dynamic equations for surface and interface

The discretized dynamic equations for the surface elevation η_2 and interface elevation η_1 can be written as:

$$\begin{aligned}
\frac{\eta_{1,i}^{n+1} - \eta_{1,i}^{n}}{\Delta t} &= -\frac{h_{1,i}^{n} u_{1,i}^{n} - h_{1,i-1}^{n} u_{1,i-1}^{n}}{\Delta x}, \\
\frac{\eta_{2,i}^{n+1} - \eta_{2,i}^{n}}{\Delta t} &= -\frac{h_{1,i}^{n} u_{1,i}^{n} - h_{1,i-1}^{n} u_{1,i-1}^{n}}{\Delta x} - \frac{h_{2,i}^{n} u_{2,i}^{n} - h_{2,i-1}^{n} u_{2,i-1}^{n}}{\Delta x},
\end{aligned} \tag{3.1}$$

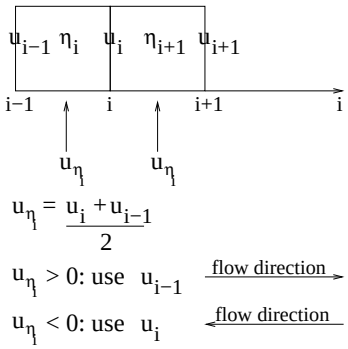

Figure 3.3: The first order upstream scheme for horizontal momentum advection in two layer model. The first oder upstream scheme investigates the flow direction at the actual grid box to guarantee that information is passed from the correct grid point in flow direction.

whereas the thicknesses $h^n_{1,i}$, $h^n_{2,i}$ of the upper and lower layer at the interval position i for the velocity grid points are explicit calculated by:

$$\begin{aligned} h^n_{1,i} &= 0.5(\eta^n_{1,i+1} + \eta^n_{1,i}) + H(x), \\ h^n_{2,i} &= 0.5(\eta^n_{2,i+1} - \eta^n_{1,i+1} + \eta^n_{2,i} - \eta^n_{1,i}), \end{aligned} \tag{3.2}$$

and in implicit form:

$$\begin{aligned} h^n_{1,i} &= 0.25(\eta^n_{1,i+1} + \eta^n_{1,i} + \eta^{n-1}_{1,i+1} + \eta^{n-1}_{1,i}) + H(x), \\ h^n_{2,i} &= 0.25(\eta^n_{2,i+1} - \eta^n_{1,i+1} + \eta^n_{2,i} - \eta^n_{1,i} + \eta^{n-1}_{2,i+1} - \eta^{n-1}_{1,i+1} + \eta^{n-1}_{2,i} - \eta^{n-1}_{1,i}). \end{aligned} \tag{3.3}$$

3.2.2 Horizontal momentum advection

The discretisation of horizontal momentum advection is done by first order upstream (Fig. 3.3). The first order upstream scheme applied for the differential form of momentum equations is the following:

$$\frac{u^{n+1}_{1/2,i} - u^n_{1/2,i}}{\Delta t} = -\frac{1}{\Delta x} \begin{cases} u^n_{1/2,i}(u^n_{1/2,i} - u^n_{1/2,i-1}) & : \quad u^n_{1/2,i} > 0 \\ u^n_{1/2,i}(u^n_{1/2,i+1} - u^n_{1/2,i}) & : \quad u^n_{1/2,i} \leq 0 \end{cases} \tag{3.4}$$

The first order upstream scheme for the conservative form of the momentum equations is as follows:

$$U^{adv}_{1/2,i} = \frac{\Delta t}{\Delta x} 0.5(U^n_{1/2,i} + U^n_{1/2,i}) \begin{cases} \dfrac{U^n_{1/2,i-1}}{h^n_{1/2,i-1}} & : \quad U^n_{1/2,i-1} + U^n_{1/2,i} \geq 0 \\ & : \\ \dfrac{U^n_{1/2,i}}{h^n_{1/2,i}} & : \quad U^n_{1/2,i-1} + U^n_{1/2,i} < 0 \end{cases} \tag{3.5}$$

so that horizontal momentum advection is discretized with:

$$\frac{U_{1/2,i}^{n+1} - U_{1/2,i}^{n}}{\Delta t} = -\frac{U_{1/2,i+1}^{adv} - U_{1/2,i}^{adv}}{\Delta x}. \tag{3.6}$$

3.2.3 Horizontal density advection

The equation for advection of density (2.51) is discretied with the first order upstream scheme:

$$\varrho_{1,i}^{n+1} = \frac{\varrho_{1,i}^{n} h_{1,i}^{n} - \frac{\Delta t(\varrho_{1,i}^{adv} - \varrho_{1,i-1}^{adv})}{\Delta x}}{h_{1,i}^{n+1}} \tag{3.7}$$

with the $\varrho_{1,i}^{adv}$-term being calculated with first order upstream:

$$\varrho_{1,i}^{adv} = \begin{cases} u_{1,i} h_{1,i} \varrho_{1,i} & : \quad u_1 > 0 \\ u_{1,i} h_{1,i} \varrho_{1,i+1} & : \quad u_1 \leq 0 \end{cases} \tag{3.8}$$

3.2.4 Horizontal momentum diffusion

The diffusion equation is as follows:

$$\frac{\partial u}{\partial t} = A_H \frac{\partial^2 u}{\partial x^2} \tag{3.9}$$

with A_H being the diffusion coefficient. This is a problem of secondary derivative and can be discretized as follows:

$$\frac{U_{1/2,i}^{n+1} - U_{1/2,i}^{n}}{\Delta t} = - A_H \frac{U_{1/2,i+1}^{n} - 2U_{1/2,i}^{n} + U_{1/2,i-1}^{n}}{(\Delta x)^2}. \tag{3.10}$$

3.2.5 Bottom friction

The influence of bottom friction to the lower layer is discretized with:

$$\frac{u_{1,i}^{n+1} - u_{1,i}^{n}}{\Delta t} = C_D \mid u_{1,i}^{n} \mid \frac{u_{1,i}^{n}}{h_{1,i}^{n}}, \tag{3.11}$$

with C_D being the drag coefficient.
The explicit bottom drag formulation is now being formed to implicit formulation. For the calculation of the horizontal velocity component in the lower layer with:

$$\begin{aligned} \hat{u} &= u_i^{n+1} \\ u &= u_i^{n} \end{aligned} \tag{3.12}$$

and A being the velocity term without consideration of bottom drag the equation is manipulated by the following steps:

$$\partial_t u_1 = A - \frac{C_D \; u_1 \mid u_1 \mid}{h}, \tag{3.13}$$

that can be transformed into:

$$\begin{aligned} \frac{\hat{u_1} - u_1}{\Delta t} &= A - \frac{C_D \; \hat{u_1} \mid u_1 \mid}{h} \\ \hat{u_1}(1 + C_D \frac{\Delta t}{h} \mid u_1 \mid) &= u_1 + \Delta t \; A \\ \hat{u_1} &= \frac{u_1 + \Delta t A}{1 + \frac{C_D}{h} \Delta t \mid u_1 \mid}. \end{aligned} \tag{3.14}$$

The benefit of the implicit formulation is that for all variations of h, C_D, Δt and u_1 the retarding effect of friction is maintained.

3.3 Full discretized two layer model equations

The explicit discretisation for η_1 and η_2 is formulated by:

$$\begin{aligned} \frac{\eta_{1,i}^{n+1} - \eta_{1,i}^n}{\Delta t} &= -\frac{h_{1,i}^n u_{1,i}^n - h_{1,i-1}^n u_{1,i-1}^n}{\Delta x}, \\ \frac{\eta_{2,i}^{n+1} - \eta_{2,i}^n}{\Delta t} &= -\frac{h_{1,i}^n u_{1,i}^n - h_{1,i-1}^n u_{1,i-1}^n}{\Delta x} - \frac{h_{2,i}^n u_{2,i}^n - h_{2,i-1}^n u_{2,i-1}^n}{\Delta x}. \end{aligned} \tag{3.15}$$

The discretized model equations for the horizontal velocity in vertical integrated form (Section 2.3) with advection (3.4) and (3.6) and diffusion (3.12) are of the following form for explicit drag:

$$\begin{aligned}
\frac{U_{1,i}^{n+1}-U_{1,i}^{n}}{\Delta t} &= \underbrace{-h_{1,i}^{n} g \frac{\eta_{2,i+1}^{n}-\eta_{2,i}^{n}}{\Delta x}}_{PRESSE_i^n} + \underbrace{A_H \frac{U_{1,i+1}^{n}-2U_{1,i}^{n}+U_{1,i-1}^{n}}{(\Delta x)^2}}_{DIFF_i^n} \underbrace{-h_{1,i}^{n} g' \frac{\eta_{1,i+1}^{n}-\eta_{1,i}^{n}}{\Delta x}}_{PRESSI_i^n} \\
&\quad \underbrace{-\frac{U_{1,i+1}^{adv}-U_{1,i}^{adv}}{\Delta x}}_{ADV_i^n} \underbrace{-C_D \frac{\mid U_{1,i}^{n} \mid U_{1,i}^{n}}{(h_{1,i}^{n})^2}}_{FRIC_i^n} \underbrace{-\frac{g}{\varrho_2}\frac{(h_{1,i+1}^{n})^2}{2}\frac{\varrho_{1,i+1}^{n}-\varrho_{1,i}^{n}}{\Delta x}}_{RHO_i^n} \\
\frac{U_{2,i}^{n+1}-U_{2,i}^{n}}{\Delta t} &= -h_{2,i}^{n} g \frac{\eta_{2,i+1}^{n}-\eta_{2,i}^{n}}{\Delta x} \\
&\quad + A_H \frac{U_{2,i+1}^{n}-2U_{2,i}^{n}+U_{2,i-1}^{n}}{(\Delta x)^2} - \frac{U_{2,i+1}^{adv}-U_{2,i}^{adv}}{\Delta x}
\end{aligned} \tag{3.16}$$

with ADV being the term for horizontal momentum advection, $FRIC$ the term due to bottom friction, $DIFF$ the horizontal momentum diffusion term, $PRESSI$ the internal pressure gradient term, $PRESSE$ the external pressure gradient term and RHO the term reproducing dynamics due to horizontal density gradients. The formulation of (3.16) with (3.14) for implicit drag is the following:

$$U_{1,i}^{n+1} = \frac{U_{1,i}^{n} + \Delta t(-PRESSI_i^n + DIFF_i^n - PRESSE_i^n - ADV_i^n - RHO_i^n)}{1 + \Delta t C_D \frac{\mid U_{1,i}^{n} \mid}{(h_{1,i}^{n})^2}} \tag{3.17}$$

3.4 Discretisation and numerical implementation for the 3D case

This section shows the model discretisation of the dynamic equations, advective terms, bottom friction and diffusion given in Chapt. 2. Some discretisations are formulated in implicit and explicit form while finally the model uses, when assigned, the implicit form. The numerical discretisation is implemented with the Arakawa-C-Grid (*Mesinger and Arakawa* [1976]). The staggered grid is represented by Fig. 3.2. The discrete values $U_{1/2}$ are given on the interval interfaces in i alternatively x-direction and the discrete values $V_{1/2}$ are given on the interval interfaces in j alternatively y-direction. All η_i are given in the centres of these intervals.

3.4.1 Dynamic equations for surface and interface

The discretized dynamic equations for the surface η_2 and interface elevation η_1 can be written as:

$$\begin{aligned}
\frac{\eta_{1,i,j}^{n+1} - \eta_{1,i,j}^{n}}{\Delta t} &= -\frac{h_{1,i,j}^{n} u_{1,i,j}^{n} - h_{1,i-1,j}^{n} u_{1,i-1,j}^{n}}{\Delta x} - \frac{h_{1,i,j}^{n} u_{1,i,j}^{n} - h_{1,i,j-1}^{n} u_{1,i,j-1}^{n}}{\Delta y}, \\
\frac{\eta_{2,i,j}^{n+1} - \eta_{2,i,j}^{n}}{\Delta t} &= -\frac{h_{1,i,j}^{n} u_{1,i,j}^{n} - h_{1,i-1,j}^{n} u_{1,i-1,j}^{n}}{\Delta x} - \frac{h_{2,i,j}^{n} u_{2,i,j}^{n} - h_{2,i-1,j}^{n} u_{2,i-1,j}^{n}}{\Delta x} \\
&\quad - \frac{h_{1,i,j}^{n} u_{1,i,j}^{n} - h_{1,i,j-1}^{n} u_{1,i,j-1}^{n}}{\Delta y} - \frac{h_{2,i,j}^{n} u_{2,i,j}^{n} - h_{2,i,j-1}^{n} u_{2,i,j-1}^{n}}{\Delta y},
\end{aligned} \tag{3.18}$$

whereas the thicknesses $hu_{1/2,i,j}^{n+1}$ and $hv_{1/2,i,j}^{n+1}$ of the upper and lower layer for the U and V grid points at the position (i,j) are implicit calculated by:

$$\begin{aligned}
hu_{1,i,j}^{n} &= 0.25(\eta_{1,i+1,j}^{n} + \eta_{1,i,j}^{n} + \eta_{1,i+1,j}^{n-1} + \eta_{1,i,j}^{n-1}) + H(x,y), \\
hu_{2,i,j}^{n} &= 0.25(\eta_{2,i+1,j}^{n} - \eta_{1,i+1,j}^{n} + \eta_{2,i,j}^{n} - \eta_{1,i,j}^{n} \\
&\quad + \eta_{2,i+1,j}^{n-1} - \eta_{1,i+1,j}^{n-1} + \eta_{2,i,j}^{n-1} - \eta_{1,i,j}^{n-1}) \\
hv_{1,i,j}^{n} &= 0.25(\eta_{1,i,j+1}^{n} + \eta_{1,i,j}^{n} + \eta_{1,i,j+1}^{n-1} + \eta_{1,i,j}^{n-1}) + H(x,y), \\
hv_{2,i,j}^{n} &= 0.25(\eta_{2,i,j+1}^{n} - \eta_{1,i,j+1}^{n} + \eta_{2,i,j}^{n} - \eta_{1,i,j}^{n} \\
&\quad + \eta_{2,i,j+1}^{n-1} - \eta_{1,i,j+1}^{n-1} + \eta_{2,i,j}^{n-1} - \eta_{1,i,j}^{n-1})
\end{aligned} \tag{3.19}$$

3.4.2 Dynamic equations of motion for horizontal velocities in transport form

To show the complete dynamic equations of motion for $U_{1/2}$ and $V_{1/2}$, advection schemes for horizontal momentum advection, horizontal momentum diffusion and horizontal density advection are demonstrated. Additionally the coriolis force is being considered for the 3D flow.

Rotation: Coriolis force

The Coriolis force under use of the Arakawa grid (Fig. 3.2) has the following discretisation:

$$
\begin{aligned}
\frac{U^{n+1}_{1,j,j} - U^n_{1,i,j}}{\Delta t} &= f0.25(V^n_{1,i,j} + V^n_{1,i+1,j} + V^n_{1,i,j-1} + V^n_{1,i+1,j-1}) \\
\frac{U^{n+1}_{2,j,j} - U^n_{2,i,j}}{\Delta t} &= f0.25(V^n_{2,i,j} + V^n_{2,i+1,j} + V^n_{2,i,j-1} + V^n_{2,i+1,j-1}) \\
\frac{V^{n+1}_{1,j,j} - V^n_{1,i,j}}{\Delta t} &= -f0.25(U^n_{1,i,j} + U^n_{1,i,j+1} + U^n_{1,i-1,j} + U^n_{1,i-1,j+1}) \\
\frac{V^{n+1}_{2,j,j} - V^n_{2,i,j}}{\Delta t} &= -f0.25(U^n_{2,i,j} + U^n_{2,i,j+1} + U^n_{2,i-1,j} + U^n_{2,i-1,j+1})
\end{aligned}
\tag{3.20}
$$

3.4.3 Horizontal momentum advection

The calculation of $h_1\partial_x(U^2_{1/2,i,j})$ is demonstrated with (3.6), the discretisation of horizontal momentum advection in spatial $x-$direction. Thus the discretisation of $h_1\partial_x(V^2_{1/2,i,j})$ is equivalent to (3.6).
The discretisation of $h_1\partial_y(U_1V_1)$ and $h_1\partial_x(U_1V_1)$ with first oder upstream is:

$$
\begin{aligned}
U^{adv}_{1/2,i,j} = 0.5(U^n_{1/2,i,j+1} + U^n_{1/2,i,j}) &\begin{cases} \frac{V^n_{1/2,i,j}}{h^n_{1/2,i,j}} & : \quad U^n_{1/2,i,j+1} + U^n_{1/2,i,j} \geq 0 \\ & : \\ \frac{V^n_{1/2,i+1,j}}{h^n_{1/2,i+1,j}} & : \quad U^n_{1/2,i,j+1} + U^n_{1/2,i,j} < 0 \end{cases} \\
V^{adv}_{1/2,i,j} = 0.5(V^n_{1/2,i,j+1} + V^n_{1/2,i,j}) &\begin{cases} \frac{U^n_{1/2,i,j}}{h^n_{1/2,i,j}} & : \quad V^n_{1/2,i,j+1} + V^n_{1/2,i,j} \geq 0 \\ & : \\ \frac{U^n_{1/2,i+1,j}}{h^n_{1/2,i+1,j}} & : \quad V^n_{1/2,i,j+1} + V^n_{1/2,i,j} < 0 \end{cases}
\end{aligned}
\tag{3.21}
$$

so that advection is calculated by:

$$
\begin{aligned}
\frac{U^{n+1}_{1/2,i,j} - U^n_{1/2,i,j}}{\Delta t} &= \frac{(V^{adv}_{1/2,i,j} - V^{adv}_{1/2,i-1,j})}{\Delta x} \\
\frac{V^{n+1}_{1/2,i,j} - V^n_{1/2,i,j}}{\Delta t} &= \frac{(U^{adv}_{1/2,i,j} - U^{adv}_{1/2,i-1,j})}{\Delta y}
\end{aligned}
\tag{3.22}
$$

3.4.4 Horizontal density advection

For the discretisation of the horizontal density advection (2.69) no further information must be given as the discretisation in y-direction is the same as in x direction shown in (3.7).

3.4.5 Horizontal momentum diffusion

The discretisation of $\partial_x(A_H\partial_x u)$ is shown in 3.2.4. The same applies for the spatial y-direction. The term $\partial_y(A_h(\partial_y u+\partial_x v))$ and $\partial_x(A_h(\partial_y u+\partial_x v))$ of (2.70) are discretized with the central difference scheme as follows:

$$\begin{aligned}
\frac{U^{n+1}_{1/2,i,j}-U^{n}_{1/2,i,j}}{\Delta t} &= \frac{0.5*A_H}{\Delta y}\Big(\frac{U^{n}_{1/2,i,j+1}-U^{n}_{1/2,i,j-1}}{\Delta y}+ \\
&\quad \frac{V^{n}_{1/2,i+1,j}+V^{n}_{1/2,i+1,j-1}-V^{n}_{1/2,i,j}-V^{n}_{1/2,i,j-1}}{\Delta x}\Big) \\
\frac{V^{n+1}_{1/2,i,j}-V^{n}_{1/2,i,j}}{\Delta t} &= \frac{0.5*A_H}{\Delta x}\Big(\frac{V^{n}_{1,i+1,j}-V^{n}_{1,i-1,j}}{\Delta x}+ \\
&\quad \frac{U^{n}_{1,i,j+1}+U^{n}_{1,i-1,j+1}-U^{n}_{1,i,j}-U^{n}_{1,i-1,j}}{\Delta y}\Big)
\end{aligned} \tag{3.23}$$

3.4.6 Bottom friction

The discretisation of bottom friction is shown in section 3.2.5. The same discretisation is made for the 3D case so that it is not given here any more.

3.5 Full discretized two layer model equations

The explicit discretisation for η_1 and η_2 is formulated by:

$$\begin{aligned}
\frac{\eta^{n+1}_{1,i,j}-\eta^{n}_{1,i,j}}{\Delta t} &= -\frac{h^n_{1,i,j}u^n_{1,i,j}-h^n_{1,i-1,j}u^n_{1,i-1,j}}{\Delta x}-\frac{h^n_{1,i,j}u^n_{1,i,j}-h^n_{1,i,j-1}u^n_{1,i,j-1}}{\Delta y}, \\
\frac{\eta^{n+1}_{2,i,j}-\eta^{n}_{2,i,j}}{\Delta t} &= -\frac{h^n_{1,i,j}u^n_{1,i,j}-h^n_{1,i-1,j}u^n_{1,i-1,j}}{\Delta x}-\frac{h^n_{2,i,j}u^n_{2,i,j}-h^n_{2,i-1,j}u^n_{2,i-1,j}}{\Delta x} \\
&\quad -\frac{h^n_{1,i,j}u^n_{1,i,j}-h^n_{1,i,j-1}u^n_{1,i,j-1}}{\Delta y}-\frac{h^n_{2,i,j}u^n_{2,i,j}-h^n_{2,i,j-1}u^n_{2,i,j-1}}{\Delta y},
\end{aligned} \tag{3.24}$$

The discretized model equations for the horizontal velocity in vertical integrated form (2.71) are of the following form for explicit drag:

$$
\begin{aligned}
\frac{U^{n+1}_{1,i,j}-U^{n}_{1,i,j}}{\Delta t} &= -\underbrace{h^{n}_{1,i,j}g\frac{\eta^{n}_{2,i+1,j}-\eta^{n}_{2,i,j}}{\Delta x}}_{PRESSE^{n}_{i}}+\underbrace{A_H\frac{U^{n}_{1,i+1,j}-2U^{n}_{1,i,j}+U^{n}_{1,i-1}}{(\Delta x)^2}}_{DIFF^{n}_{i}} \\
&+\underbrace{\frac{0.5*A_H}{\Delta y}\Big(\frac{U^{n}_{1,i,j+1}-U^{n}_{1,i,j-1}}{\Delta y}+\frac{V^{n}_{1,i+1,j}+V^{n}_{1,i+1,j-1}-V^{n}_{1,i,j}-V^{n}_{1,i,j-1}}{\Delta x}\Big)}_{DIFFM^{n}_{i}} \\
&+\underbrace{0.25f(V^{n}_{1,i,j}+V^{n}_{1,i+1,j}+V^{n}_{1,i,j-1}+V^{n}_{1,i+1,j-1})}_{COR^{n}_{i}} \\
&-\underbrace{h^{n}_{1,i,j}g'\frac{\eta^{n}_{1,i+1,j}-\eta^{n}_{1,i,j}}{\Delta x}}_{PRESSI^{n}_{i}}-\underbrace{\frac{U^{adv}_{1,i+1,j}-U^{adv}_{1,i,j}}{\Delta x}}_{ADV^{n}_{i}} \\
&-\underbrace{\frac{(V^{advm}_{1,i,j}-V^{advm}_{1,i-1,j})}{\Delta x}}_{ADVM^{n}_{i}}-\underbrace{C_D\frac{\mid U^{n}_{1,i,j}\mid U^{n}_{1,i,j}}{(h^{n}_{1,i,j})^2}}_{FRIC^{n}_{i}}-\underbrace{\frac{g}{\varrho_2}\frac{(h^{n}_{1,i,j})^2}{2}\frac{\varrho^{n}_{1,i+1,j}-\varrho^{n}_{1,i,j}}{\Delta x}}_{RHO^{n}_{i}} \\
\frac{U^{n+1}_{2,i,j}-U^{n}_{2,i,j}}{\Delta t} &= -h^{n}_{2,i,j}g\frac{\eta^{n}_{2,i+1,j}-\eta^{n}_{2,i,j}}{\Delta x}+A_H\frac{U^{n}_{2,i+1,j}-2U^{n}_{2,i,j}+U^{n}_{2,i-1,j}}{(\Delta x)^2} \\
&+\frac{0.5*A_H}{\Delta x}\Big(\frac{V^{n}_{2,i+1,j}-V^{n}_{2,i-1,j}}{\Delta x}+\frac{U^{n}_{2,i,j+1}+U^{n}_{2,i-1,j+1}-U^{n}_{2,i,j}-U^{n}_{2,i-1,j}}{\Delta y}\Big) \\
&+0.25f(V^{n}_{2,i,j}+V^{n}_{2,i+1,j}+V^{n}_{2,i,j-1}+V^{n}_{2,i+1,j-1}) \\
&-\frac{U^{adv}_{2,i+1,j}-U^{adv}_{2,i,j}}{\Delta x}-\frac{V^{advm}_{2,i,j}-V^{advm}_{2,i-1,j}}{\Delta x}.
\end{aligned}
\tag{3.25}
$$

In addition the vertically integrated dynamic equations of motion with the implicit form for the discretisation of bottom friction (3.14) is as follows:

$$
\begin{aligned}
X &= -PRESSE_i^n + DIFF_i^n + DIFFM_i^n + COR_i^n - PRESSI_i^n \\
&\quad -ADV_i^n - ADVM_i^n - FRIC_i^n - RHO_i^n \\
U_{1,i}^{n+1} &= \frac{U_{1,i,j}^n + \Delta t X}{1 + \Delta t C_D \frac{\mid U_{1,i,j}^n \mid}{(h_{1,i,j}^n)^2}}
\end{aligned}
\tag{3.26}
$$

The dynamic equations for the vertically integrated transports in upper and lower layer $V_{1,i,j}^{n+1}$ and $V_{2,i,j}^{n+1}$ in spatial $y-$direction are obtained with (3.25) by the following transformations for the indices:

$$
\begin{aligned}
\text{term}_{i,j} &\rightarrow \quad \text{term}_{i,j} \\
\text{term}_{i,j+1} &\rightarrow \quad \text{term}_{i+1,j} \\
\text{term}_{i+1,j} &\rightarrow \quad \text{term}_{i,j+1} \\
\text{term}_{i-1,j+1} &\rightarrow \quad \text{term}_{i+1,j-1} \\
COR_i^n &\rightarrow \quad (-1) * COR_i^n
\end{aligned}
\tag{3.27}
$$

3.6 Numerics

This section covers the description of the implemented drying and flooding algorithm, individual model problems, that occur due to previously given two layer model equations and discretisation, and consequences that appears while using specified algorithms and principles.
The simulations with the two layer model dealt within this thesis were implemented with closed lateral boundaries where the following applies for the model domain boundaries:

$$\begin{aligned} u_1 &= 0 \\ u_2 &= 0 \\ v_1 &= 0 \\ v_2 &= 0 \end{aligned} \tag{3.28}$$

The model is not well-appointed with a 'sponge-layer' (e.g. *Roed and Cooper* [1986]), an outer dissipative domain, that would have a dissipative effect on waves or disturbances that leave the inner model domain due to an successive coarsening of the grid box length and increasing internal friction. Thus the appearance of disturbances or waves will cause dynamics within the model domain that are active due to reflections at the boundaries until they are dissipated within the model domain. Consequences of this not yet included feature of the two layer model and the impact on internal waves or gravity currents are not investigated within this thesis.

3.6.1 The lateral boundaries of the plume - drying and flooding algorithm

The implemented drying and flooding algorithm (Fig. 3.4) guarantees that for sloping bathymetry and non-stationary flows the interface η_1 does not sink below the sea bed. The interface can be figured as a membrane that lies on the bottom with the reference to an arbitrarily chosen minimum thickness of $D_{min}/2 = 0.01m$. Whenever dynamics occur that will lead to thickness values of $h_1 < D_{min}/2$ (see Fig. 3.4) for the lower layer the velocities of the adjacent velocity points are set to zero. While setting velocity values at only one certain grid box to zero, the adjacent grid points could also sink below the sea bed. Hence this algorithm has to check the thickness values of the lower layer until all velocities leading to $h_1 < D_{min}/2$ at the elevation grid points are of value zero. This will prevent further fading of the sea level. Consequently a grid box can be considered as dry when $h_1 \leq D_{min}/2$.
Dynamics that produce an increase of interface elevation turn a 'dry' grid box into a 'flooded' grid box. This drying and flooding algorithm easily allows to split and merge plumes due to topographic barriers like sills.
It is assumed that the major process for thicknesses h_1 of a few centimetres for the lower layer is the balance between bottom friction (Sect. 2.2.3) and pressure gradient (Sect. 3.6.2). The used formulation for the calculation of the bottom drag coefficient (2.46) is exponentially growing for small thickness values h_1 (see Fig. 2.2). Hence this

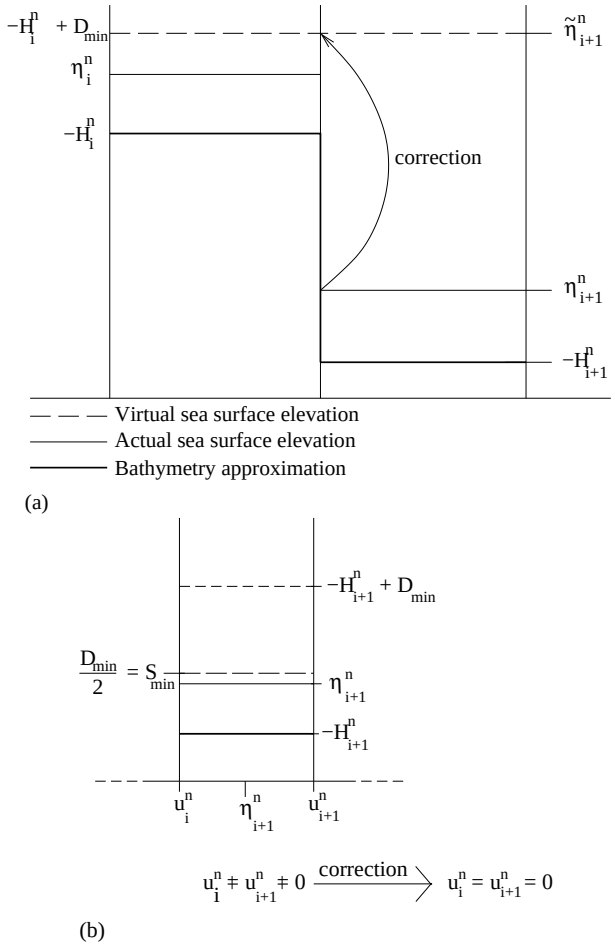

Figure 3.4: (a) Pattern showing the principle of pressure gradient minimization (*Burchard et al.* [2004]) during drying and flooding over sloping bathymetry. The pressure gradient calculated by the difference of η_i^n and η_{i+1}^n is un-physically high. This would cause too much water running out of the left grid cell. The corrected pressure gradient is now represented by the difference of $\tilde{\eta}_{i+1}^n = -H_i + D_{min}$ and η_i^n. Another Problem that occurs with this principle of pressure gradient minimization is, that in the case shown here where already too much water ran out of the left grid cell, water is even flowing back. With further grid refinement this problem is negligible. (b) Second sketch shows the grid box of the elevation with the adjacent velocity points. In this case the sea level η_{i+1}^n is less than $S_{min} = 0.5 D_{min}$. To prevent further fading of the interface level, with the potentially resulting situation of a negative thickness of the lower layer, the adjacent velocities will be set to the value of zero. This step in box η_{i+1}^n perhaps will affect the adjacent boxes. So these boxes have to be checked under use of the emergency brake, too.

is additionally limiting flow dynamics and avoiding negative thickness values for the lower layer.

3.6.2 Principle of pressure gradient minimization

The principle of pressure gradient minimization (*Burchard et al.* [2004]) during drying and flooding over sloping bathymetry represents a method to circumvent a special numerical problem. That could occur while using the implemented drying and flooding algorithm (Sect. 3.6.1). This Problem occurs when the sea surface of the cell at position $i+1$ is below the sea bed of the cell at position i or contrariwise. In this case the pressure gradient will be un-physically high. As a consequence too much water is running out of cell i. Fig. 3.4b is explaining this numerical problem and the solution in detail.

3.6.3 Individual model problem: interface touching surface

Due to the problem, that the interface η_1 can touch or even penetrate the surface elevation η_2 whenever waves with a high amplitude within the plume or the plume itself reaches shallow waters, arrangements must be considered to circumvent this in the model equations not intended case. Because of the calculation of the thickness of the upper layer h_1 with the difference between the interface η_1 and the surface elevation η_2 (3.2) negative values for h_1 can occur.
The solution suggested here is not momentum conserving due to the fact that the velocities have to be set to zero whenever a situation occurs that will rise the interface elevation above the surface elevation (Fig. 3.4). Hence the solution considered here is called 'emergency brake'. Compared with the method of checking the depth of the interface with regard to the sea bed for the drying and flooding algorithm (Sect. 3.6.1) the 'emergency brake' has a similar implementation: all velocities of the adjacent grid boxes are set to zero. This procedure is repeated as often as dynamics could produce situations with $\eta_2 - \eta_1 \leq D_{min}$.
Problems at shallow water at coastal areas where potential high velocities and unsteady flows cause problems with the case spoken to, the bathymetry is smoothed and shallow grid boxes with $H < 3m$ are changed to depth values of $H = 3m$. During test runs this depth value has been considered as satisfying to avoid using the 'emergency brake'.
Consequences of both smoothing the bathymetry and using the 'emergency brake' on the model results are not being investigated within this thesis.

3.6.4 Implementation of Entrainment

Because of the entrainment process, see (2.62), being a local process, the entrainment is implemented into the model without any further sophistication. This process only depends on the local values at a certain grid box as they are velocity, plume thickness and density for a whole water column of the lower layer (plume).
After calculation of the entrainment rate with (2.62), adaptations of interface elevation, horizontal velocities u_1 and u_2 and density ϱ_1 in the lower layer have to be done, which are for $\partial\varrho_2/\partial_x = 0$ as follows for density:

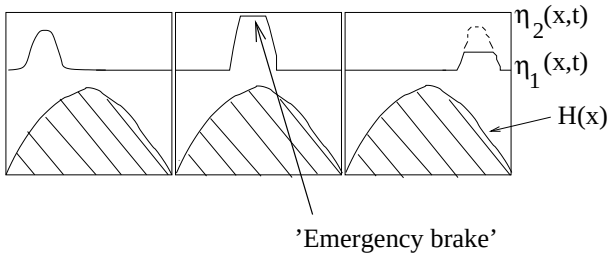

Figure 3.5: This series of propagation an internal wave illustrates how momentum can get lost when applying the 'emergency brake'. When the velocities are zero because of the 'emergency brake', further rising of the interface is being averted and the wave loses some of it's momentum. To guarantee momentum conservation, the depth at for the two layer model critical points is being heightened up to an value that with the help of some test cases with complex bathymetry has been considered as satisfying to avoid using the 'emergency brake'.

$$\begin{aligned} \varrho_{1,i}^{n+1} &= \frac{h_{1,i}^n \varrho_{1,i}^n + H_{E,i}^{n+1} \varrho_2}{h_{1,i}^n + H_{E,i}^{n+1}}, \\ \lim_{H_E \to 0} \varrho_{1,i}^{n+1} &= \varrho_{1,i}^n, \end{aligned} \tag{3.29}$$

With H_E:

$$H_E = w_E \Delta t \tag{3.30}$$

with Δt denoting the applied time-step in the simulation.
The interface elevation has to be updated as follows:

$$\eta_{1,i}^{n+1} = \eta_{1,i}^n + H_{E,i}^{n+1}, \tag{3.31}$$

whereas no changes to the surface elevation have to be done because the turbulent exchange between lower and upper layer only takes place as a mixing of the upper layer into the lower layer.
On the other hand the vertically integrated transports must be adapted for both upper and lower layer:

$$\begin{aligned} U_1^{n+1}(i,j) &= U_1^n(i,j) + \frac{H_E^{n+1} U_2^n(i,j)}{h_2^n(i,j)}, \\ U_2^{n+1}(i,j) &= \frac{U_2^n(i,j)}{h_2^n(i,j)} (h_2^n(i,j) - H_E^{n+1}(i,j)). \\ \lim_{H_E \to 0} U_{1,i}^{n+1} &= U_{1,i}^n \end{aligned} \tag{3.32}$$

Chapter 4

Basic test experiments

In this chapter basic test experiments under mainly idealized conditions are implemented for testing and validation of the two layer model. At the beginning the two layer model equations are linearized to get comparable results with analytical solutions derived for standing internal waves and plumes in a closed rectangular basin with vertical walls.
The implemented idealized experiments are very helpful in understanding the output of the two layer model during simulations of more complex model results as obtained and discussed in Chapt. 5 with the idealized simulation of the Arkona inflow event.
Most of the test cases with simulations in a closed rectangular basin with vertical walls are done with a constant value for the bottom drag coefficient with $C_D = 0.0025$ as suggested in Sect. 2.2.3. The drying and flooding algorithm is not being applied as this algorithm is not needed for non-sloping bathymetries. As a matter of fact the output of the two layer model is restricted only to mean physical values for a single water column of the upper and lower layer. Consequences are for example that the process of light water shifting above dense water can not be reproduced. This limitation of the two layer model is being shown by means of model results discussed in Sect. 4.2.3

4.1 Experiments without entrainment

4.1.1 Experiments with linearized two layer model equations

In this section we run the existing model with an immiscible, inviscid, and incompressible fluid with constant but different densities with the application to standing internal waves (Fig. 4.1). Horizontal momentum advection and momentum diffusion is switched off during this simulation.

To prepare the two layer model for the validation with analytical solutions, the model equations (2.64) have to be linearized. To show that the differences in simulation results of the linearized two layer model equations compared to the non-linear equations are small, it is switched between linearity and non-linearity and between a one and a two

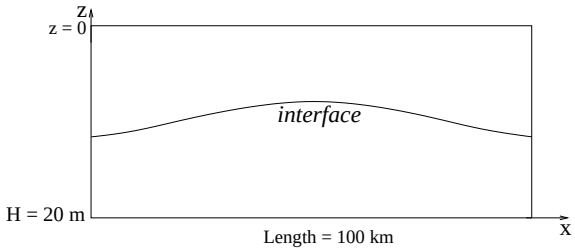

Figure 4.1: Schematic illustration of initial condition of standing internal wave.

layer system. The difference among linearity with $\partial_x h_1 = 0$ and non-linearity with $\partial_x h_1 \neq 0$ can be shown with (2.17) and applies as well to (2.18):

$$\begin{array}{lll} \text{non-linear:} & \partial_t \eta_1 & = -\partial_x (h_1 u_1), \\ \text{linear:} & \partial_t \eta_1 & = -h_1 \partial_x (u_1). \end{array} \tag{4.1}$$

Under these conditions there are four different situations to be plotted in this section:

Case	Number of participating layers	Linearity/Non-linearity
(1)	one	linear
(2)	one	non-linear
(3)	two	linear
(4)	two	non-linear

Fig. 4.2 points out how small the differences of the simulation results between linear assumption and non-linear model equations are for the simulation of standing internal waves. Fig. 4.2 shows the elevation of the standing internal wave in centre plotted over time for the four different cases. Differences of the solutions between linearity and non-linearity for both layer switched on are negligible. Small differences are obtained for the case that the upper layer is switched off. The analytical solutions derived in the next sections are only valid for the case of the upper layer switched off. Thus the differences for the one layer system in linear and non-linear case has to be investigated more closely. With a difference of around two hours after 16 days of simulation time both solutions for standing internal waves with an amplitude of 0.1 m arrive at the same state. The difference after these 16 days of simulation is below 0.6% and hence small enough to be negligible.

4.1.2 Application to standing internal wave

In this section the analytical solution of standing internal waves in a closed rectangular basin with vertical walls is being derived and compared with the linearized two layer model equations.
During this experiment the upper layer is switched off and bottom friction as well as

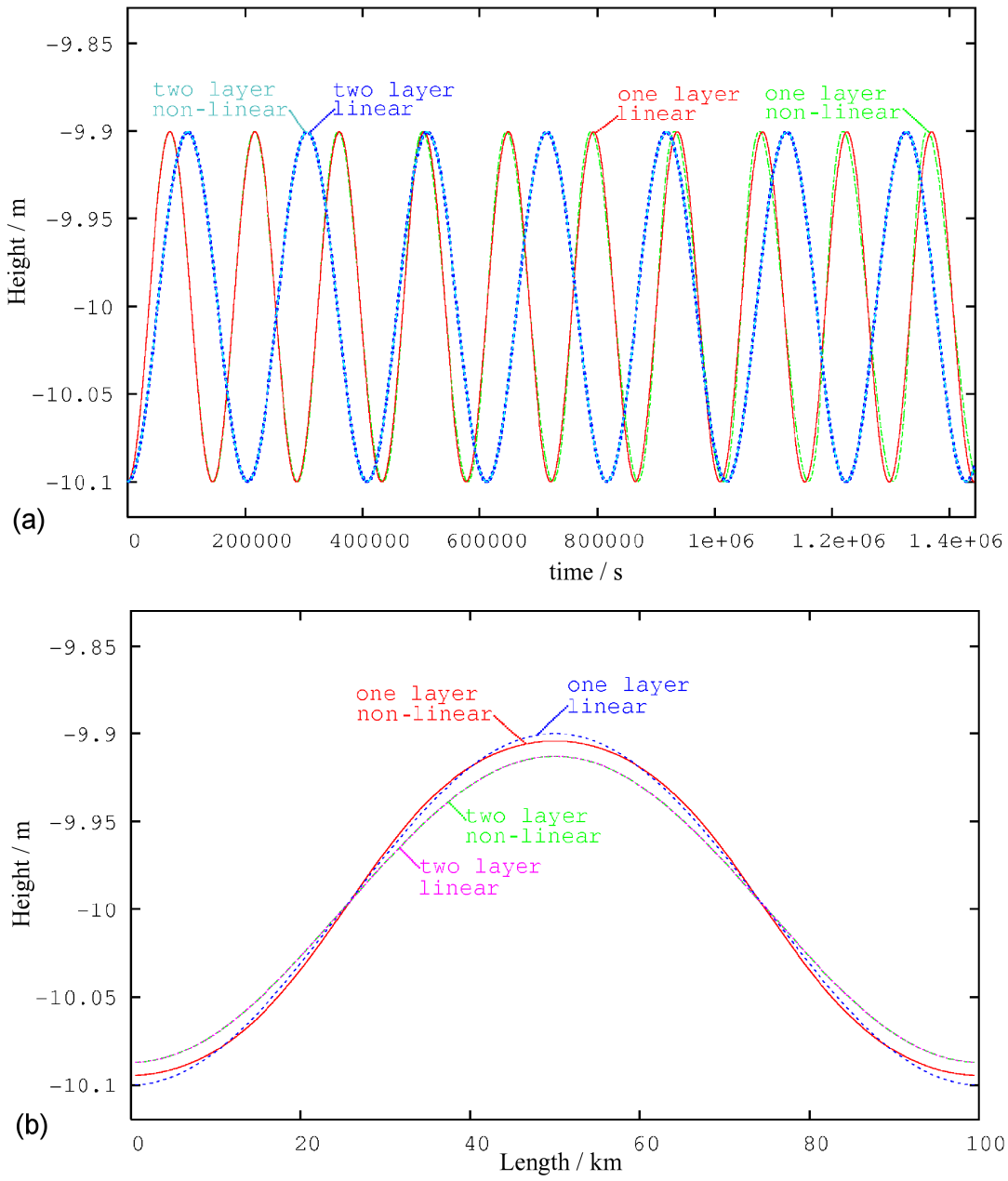

Figure 4.2: (a) Elevation plotted over time under modification of linearity and number of participating layers. (b) Elevation of lower layer at simulation end, after 10.5 periods.

horizontal momentum advection are not implemented. To obtain comparable results of analytical and numerical solution, the linear assumption (4.1) between elevation and velocity is used. A validation of the two layer model equations is accomplished with the help of an error calculation (Fig. 4.3) between analytical and numerical solution.

Derivation of analytical solution for standing waves

The linearized shallow water equations in one spatial dimension are of the following form:

$$\begin{aligned} \partial_t \eta &= -H \partial_x u \\ \partial_t u &= -g \partial_x \eta \end{aligned} \tag{4.2}$$

with the elevation $\eta(x,t)$, velocity $u(x,t)$, the constant gravitational acceleration g and the constant water depth H.
Equations (4.2) are now formulated as wave equations for η and u. These wave equations will help us to obtain the wave propagation speed c. First of all equations (4.2) are differentiated with respect to t and x:

$$\begin{aligned} \partial_x \partial_t \eta &= -H \partial_x \partial_x u \\ \partial_t \partial_t u &= -g \partial_t \partial_x \eta. \end{aligned} \tag{4.3}$$

In both equations the term $\partial_x \partial_t \eta$ occurs, so that the wave equation for u is the following:

$$\partial_t^2 u - Hg \partial_x^2 u = 0. \tag{4.4}$$

The wave equation for η is derived with the same procedure and is as follows:

$$\partial_t^2 \eta - Hg \partial_x^2 \eta = 0. \tag{4.5}$$

Using (4.4) and (4.5), the general wave equations in one spatial dimension, the wave propagation speed is obtained:

$$c = \sqrt{gH}, \tag{4.6}$$

that is a function of gravitational acceleration g and height H. Equation (4.6) applies for waves with $\lambda > 20H$ in wave theory. This means that the wave propagation speed c of such waves only depend on the depth H and not on the wavelength λ.
Now the analytical solution for the elevation η_a and velocity u_a for standing waves is derived. Here the spatial coordinate x is of the range $0 \leq x \leq L$ and L being the length of the domain. Consequently the boundary conditions are:

$$u_a(0,t) = u_a(L,t) = 0. \tag{4.7}$$

with u_a representing the analytically obtained horizontal velocity.
For the initial condition we set arbitrarily:

$$\eta_a(x,0) = 0, \tag{4.8}$$

which means that we have no elevation at simulation start with $t = 0$ s for the analytically calculated elevation η_a.
An assumption for $u_a(x,t)$ will be:

$$u_a(x,t) = 0,5(U_1 \sin(k(x+ct)) + U_2 \sin(k(x-ct))) \tag{4.9}$$

with unknown velocity amplitudes for the wave traveling to the left and to the right, U_1 and U_2, and wave number k. With (4.7), for the case of standing internal waves, the wave number k is:

$$k = n2\pi/L, \text{ for } n = 1,2,3,... \tag{4.10}$$

With the postulation of standing waves we can derive the relation between U_1 and U_2. With (4.9) we have:

$$u_a(0,t) = 0,5(U_1 \sin(kct) + U_2 \sin(-kct)) = 0, \tag{4.11}$$

that is consequently only fulfilled for:

$$U_1 = U_2 = U. \tag{4.12}$$

With the help of previous equations the analytical solution for horizontal velocity $u_a(x,t)$ and elevation $\eta_a(x,t)$ are derived with regard to the initial condition (4.8). For $u_a(x,t)$ we can write with the help of (4.9):

$$\begin{aligned} u_a(x,t) &= 0,5U(\sin(kx+kct) + \sin(kx-kct)) \\ &= 0,5U(2\sin(kx)\cos(kct)) \\ &= U\sin(kx)\cos(kct), \end{aligned} \tag{4.13}$$

where kc is the angular frequency ω.
To get the equation for $\eta_a(x,t)$ we use (4.13). On this note we have to differentiate $u_a(x,t)$ with regard to x:

$$\partial_x u_a = kU\cos(kx)\cos(kct), \tag{4.14}$$

thus the first equation of (4.2) is as follows:

$$\begin{aligned} \partial_t \eta_a &= -H\partial_x u_a \\ &= -HkU\cos(kx)\cos(kct). \end{aligned} \tag{4.15}$$

With integration of (4.15) between t_1 and t_2 we consequently have:

$$\int_{t_1}^{t_2} \partial_t \eta_a(x,t)\mathrm{d}t = HkU\cos(kx)\int_{t_1}^{t_2}\cos(kct)\mathrm{d}t. \tag{4.16}$$

With $t_1 = 0$ s because of initial condition (4.8) and $t_2 = t$, the solution for $\eta_a(x,t)$ finally is:

$$\begin{aligned} \eta_a(x,t_2) - \eta_a(x,t_1) &= -\frac{HkU}{kc}\cos(kx)(\sin(kct_2) - \sin(kct_1)) \\ \eta_a(x,t) &= -\frac{HU}{c}\cos(kx)\sin(kct) \end{aligned} \tag{4.17}$$

We now remember the initial conditions (4.8) used for our validation. The initial-condition $u_a(x,0)$ is obtained if we solve (4.13) for $t = 0$ s, so that that the initial conditions for u_a and η_a are:

$$\begin{aligned} u_a(x,0) &= U\sin(kx), \\ \eta_a(x,0) &= 0. \end{aligned} \tag{4.18}$$

The analytical solutions of standing internal waves with the help of the linearized shallow water equations (4.2) are:

VARIABLE	EQUATION
u_a	$u_a(x,t) = U\sin(kx)\cos(kct),$
η_a	$\eta_a(x,t) = -\frac{HU}{c}\cos(kx)\sin(kct).$

Validation of general model equations with analytical solution of standing internal wave

We will proceed with the validation of the numerical solution of the linearized two layer model equations. This is done by a direct comparison to the analytical equations for standing internal waves derived above. Hence the deviation between numerical and analytical solution is calculated and plotted (Fig. 4.3) with the help of an error calculation. On this note the L_2 norm is applied based on the number of measurements n to calculate the error E_{err}:

$$\begin{aligned} L_2 \text{ norm:} \quad & || \, u_n - u_a \, ||_0 = \left(\textstyle\sum_i (u_n(i) - u_a(i))^2\right)^{1/2}, \\ \text{Error } E_{err}: \quad & E_{err} = \left(\tfrac{1}{n}\textstyle\sum_i (u_n(i) - u_a(i))^2\right)^{1/2} \end{aligned} \tag{4.19}$$

with u_a being the analytical calculated velocity and u_n being the numerical calculated velocity.
The numerical calculation of standing internal waves is done and the conditions $\partial_x \varrho_1 = 0$ and $\partial_t \varrho_1 = 0$ with the following simplified equations of the two layer model:

$$\begin{aligned} \eta_{1,i}^{n+1} &= \eta_{1,i}^{n} - \Delta t h_1 \frac{u_{1,i}^{n} - u_{1,i-1}^{n}}{\Delta x}, \\ u_{1,i}^{n+1} &= u_{1,i}^{n} - \Delta t g' \frac{\eta_{1,i+1}^{n} - \eta_{1,i}^{n}}{\Delta x}. \end{aligned} \tag{4.20}$$

The Error E_{err} is plotted against a reduction of time-step in the simulation. It is essential to vary the time-step in consultation with the Courant-Friedrich-Levy(CFL) condition. This condition implements that no information should pass more than one grid box per time step.
With the wave propagation speed c:

$$c = \sqrt{gH} \tag{4.21}$$

we see that the CFL condition for our problem is:

$$\frac{\Delta x}{\Delta t} \geq \sqrt{gH}. \tag{4.22}$$

For the initial conditions in our simulation a CFL condition of approximately 0.7 m s^{-1} is obtained. An error plot is provided while the time-step and the box length are varied under the following arbitrarily chosen relation:

$$\frac{\Delta x}{\Delta t} = 1.8\mathrm{CFL}. \tag{4.23}$$

In a double logarithmic plot, see Fig. 4.3, the relation between time-step and Error E_{err} is shown. The deviation between both simulations decreases for decreasing time step. The non-linearity in the graph results from the machine accuracy. We can prove this motivation if we change the codomain from *double precision* to *real* in the Fortran source code. A decrease of time step for *real* can not reproduce the same results as with the accuracy of *double precision*. Thus the non-linearity in the double logarithmic plot (Fig. 4.3) is due to machine accuracy and is not founded due to certain numerical problems with the model equations.

4.1.3 Application to plume propagation

In this section an analytical solution for a plume (*Burchard* [1995]) is derived. This analytical solution is being compared with the linearized two layer model equations. It is shown that the analytical solution is similar compared to the numerical solution with respect to the horizontal coordinate x and the time t.
A difference to the analytical solution for standing internal waves is that bottom friction is implemented in the analytical solution derived in this section.

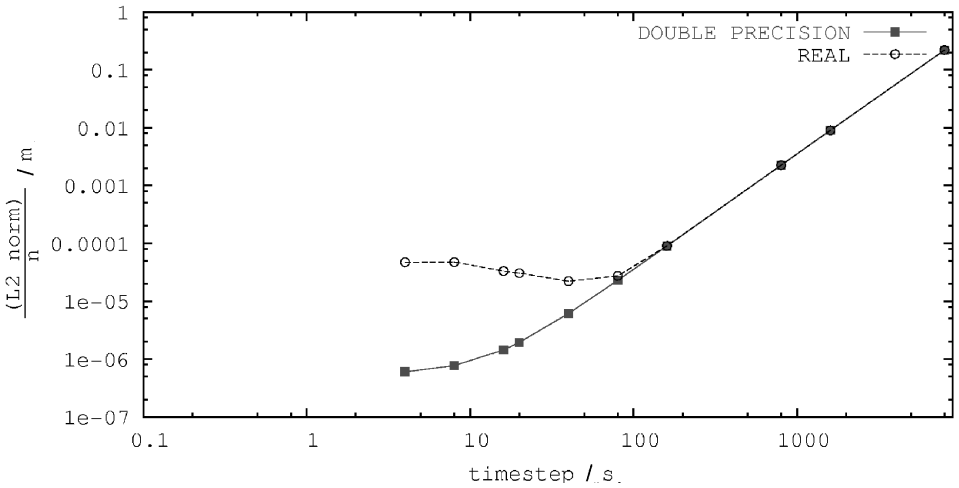

Figure 4.3: Error between numerical and analytical solution with $\Delta x/\Delta t = 1.8$ CFL. Sketch showing that further resolution of the model could only give correct results up to a certain degree. The non-linearity symbolizes inaccuracies as a result of machine accuracy. This motivation is proved with changing the codomain from double precision to real. The same non-linearity occurs earlier.

Derivation of analytical plume solution

With equation (2.40) we switch off the upper layer ($\partial_x \eta_2 = 0$) and add the bottom friction (Section 2.2.3) to the model:

$$\partial_t u_1 + u_1 \partial_x u_1 = -g' \partial_x \eta_1 - C_D \frac{u_1 \mid u_1 \mid}{h_u}, \tag{4.24}$$

with $h_u = h_u(x,t)$ being the height of the plume and C_D being constant. For equation (2.17) we can write:

$$\partial_t \eta_1 + \partial_x (h_u u_1) = 0. \tag{4.25}$$

Assuming that $u_1 = \text{const.}$ and $h_u = \eta_1$ will turn (4.25) into:

$$\partial_t \eta_1 + u \partial_x \eta_1 = 0, \tag{4.26}$$

and (4.24) can be simplified for positive velocity values which implies that this analytical solution only applies for a propagation in one direction:

$$0 = -g' \partial_x \eta_1 - C_D \frac{u_1^2}{\eta_1}. \tag{4.27}$$

With our assumption that the horizontal velocity u_1 is constant, a coordinate system moving with the flow has a constant water level with respect to t:

$$\eta_1 = \eta_1(\xi); \text{ where: } \xi = x - u_1 t. \tag{4.28}$$

According to (4.26) we have the following relation for $\partial_\xi \eta$:

$$\partial_t \eta_1 = -u_1 \partial_\xi \eta_1, \text{ with: } \partial_x \eta_1 = \partial_\xi \eta_1. \tag{4.29}$$

With (4.27) and $\partial_\xi = \partial_x$ we get the differential equation for η_1:

$$\partial_\xi \eta_1 \quad = -\frac{C_D}{g'} u_1^2 \eta_1^{-1}. \tag{4.30}$$

Solving (4.30) will lead to the analytical plume solution, with $u_1 = u_{plume} = \text{const.}$ being the velocity of propagation of the plume and $\eta_a = \eta_1$ we have:

$$\begin{aligned}
\frac{d\eta_a}{d\xi} &= -\frac{C_D}{\eta_a g'} u_{plume}^2 \\
\eta_a d\eta &= -\frac{C_D}{g'} u_{plume}^2 \mathrm{d}\xi \\
\int \eta_a d\eta_a &= -\frac{C_D}{g'} u_{plume}^2 \int \mathrm{d}\xi \\
\frac{\eta_a^2}{2} &= -\frac{C_D}{g'} u_{plume}^2 \xi + C \\
\eta_a &= \sqrt{\left(-\frac{2C_D}{g'} u_{plume}^2 \xi + C \right)} \\
\eta_a &= \sqrt{\left(-\frac{2C_D}{g'} u_{plume}^2 (x - u_{plume} t) + C \right)}.
\end{aligned} \tag{4.31}$$

The derivation of an analytical solution for the propagation of a plume in a rectangular box with vertical walls with given boundary conditions for the inflow area is now being compared with the results of the numerical solution of the linearized two layer model equations.

Validation of general model equations with analytical plume solution

For the validation of the model equations with the analytical plume solution, the simulation starts at $t = 0$ s with the first velocity grid cell being 'flooded', see Fig. 4.4. The constant value C of (4.31) can now be calculated by using (4.31) together with the initial condition shown in sketch (4.4):

$$C = -\frac{2C_D}{g'} u_{plume}^2 \Delta x, \tag{4.32}$$

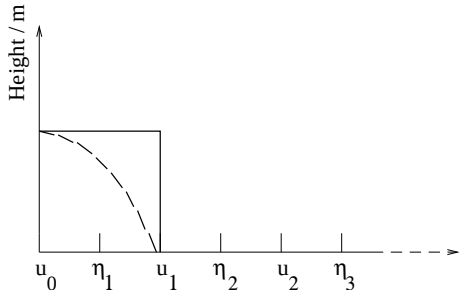

Figure 4.4: This figure is showing the initial condition for the plume test case. The first u grid cell is flooded.

where Δx is the length of one grid cell in the C-Grid.
For the numerical calculation of the plume elevation $\eta_a(x,t)$ we have the following conditions during the whole simulation time:

$$\begin{aligned} \eta_{numerical}(t,0) &= \eta_a(t,0), \\ u_{numerical}(t,0) &= u_{plume}. \end{aligned} \tag{4.33}$$

The boundary conditions at the left side are a constant horizontal inflow velocity: $v_{plume} = 0.2\text{m s}^{-1}$ and the height of plume given by the analytical plume solution derived in this chapter. Figure 4.5a shows that numerical and analytical solution are similar. To show the impact of the upper layer on the lower layer, the upper layer is switched on and the results are plotted in Fig. 4.5b together with the result of the upper layer switched off. The difference between both situations is significant. The surface elevation η_2 is lifted above the front of the plume and water is flowing back. This effect of lifting of the upper layer and backward flowing water with $u_2 < 0$ m s $^{-1}$ is also demonstrated and obtained in Sect. 4.1.6 shown in Fig. 4.10.

4.1.4 Application to lock exchange experiment

In this section a more realistic fluid mechanical test case, the lock exchange test, with bottom friction, horizontal momentum diffusion and horizontal momentum advection is investigated. In this test case a 20 m deep closed rectangular basin of 100 km length with vertical walls containing two fluids with a density difference of 15 kg m^{-3} is separated by a vertical interface in the centre. This interface is removed at $t = 0$. Due to the internal pressure gradient term $PRESSI$ in (2.64) the dense water is layering under the lighter water. The initial condition can be seen in Fig. 4.6. A plot of the result showing the flow at four different times can be seen in Fig. 4.7. Furthermore the different impact of horizontal momentum advection, horizontal momentum diffusion and bottom friction is observed.

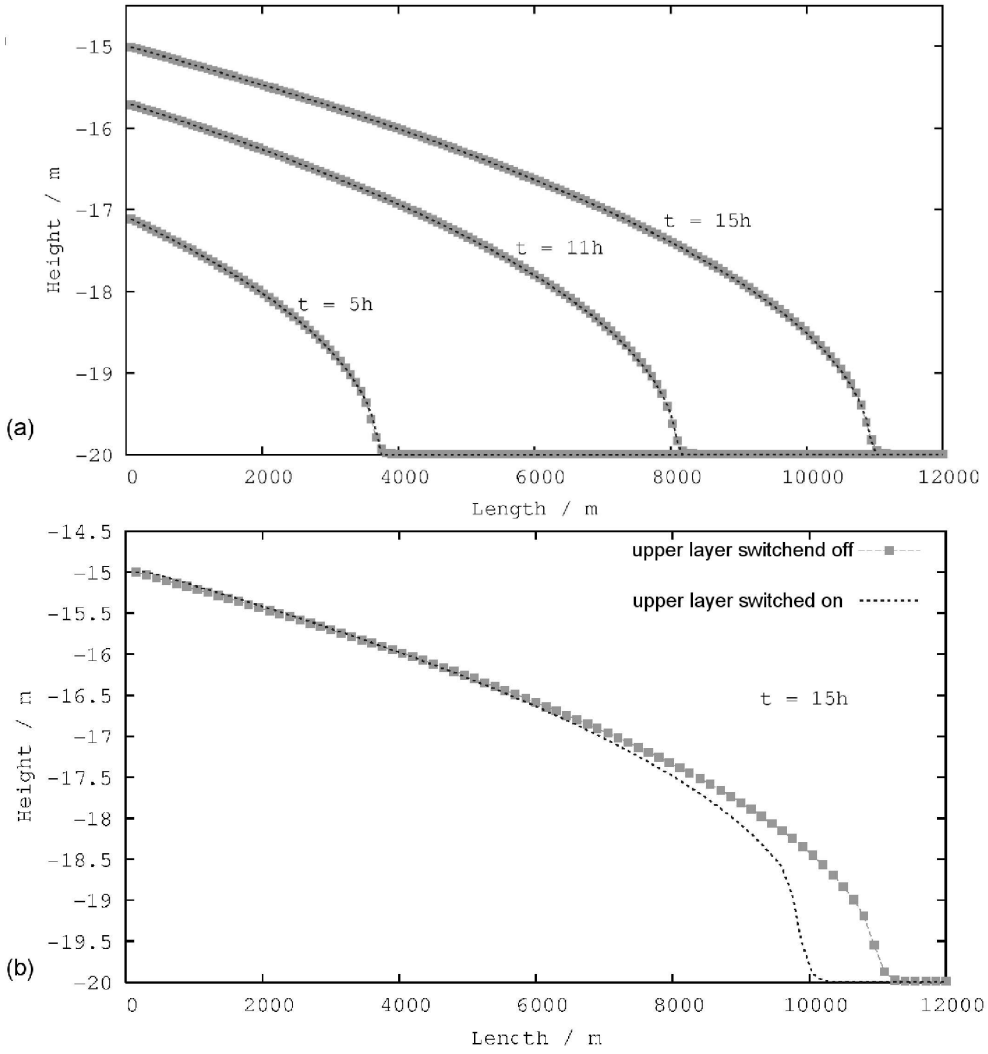

Figure 4.5: (a) Plume propagation with friction: Analytical solution (dashed) compared with model results (points) for $t = 5h$, $t = 11h$ and $t = 15h$. $C_D = 0.0025$, $\Delta t = 0.5s$, $\Delta x = 75m$. (b) This sketch reflects the difference between the solutions of plume propagation with upper layer switched on and off. $H = 20m$, $\varrho_1 = 1014$, $\varrho_2 = 1005$, $C_D = 0.0025$, $\Delta t = 0.5$s, $\Delta x = 150m$.

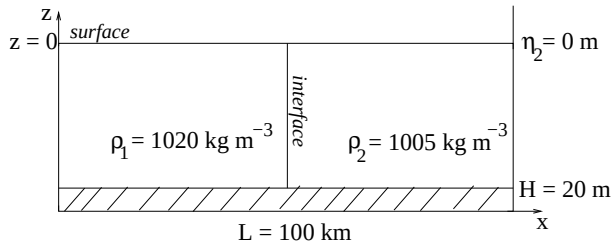

Figure 4.6: Schematic illustration of initial conditions for lock exchange experiment

Model equations for lock exchange experiment

In this section we add horizontal momentum diffusion, horizontal momentum advection and bottom friction to the model equations and use the explicit drag formulation (3.16). A simulation of the lock exchange experiment modeled with the equations given in Sect. 2.3 verified the expectation that the layer with greater density propagates like a plume below the lighter fluid (Fig. 4.7). A simulation of the lock exchange experiment without horizontal momentum advection and diffusion (Fig. 4.7) shows a numerical instability in the modeled interface. Diffusion smoothes the numerical result.

Impact of horizontal momentum advection, horizontal momentum diffusion and bottom friction to model result

To show the different impact of advection, diffusion ($A_H = 10$ m^2 s^{-1}) and bottom friction to the model results the front velocity of the plume is calculated under the following different conditions:

hor. mom. advection	hor. mom. diffusion	bottom friction	front velocity / m s^{-1}
on	off	on	0.2779
off	off	on	0.2983
off	on	on	0.2984
on	off	off	0.4794
on	on	off	0.4796
off	off	off	0.4916
off	on	off	0.4955

As expected the bottom friction has the biggest retarding impact on the current. A comparable but smaller impact has the horizontal momentum advection that decreases the front velocity. On the other hand the diffusion slightly increases the velocity of propagation.

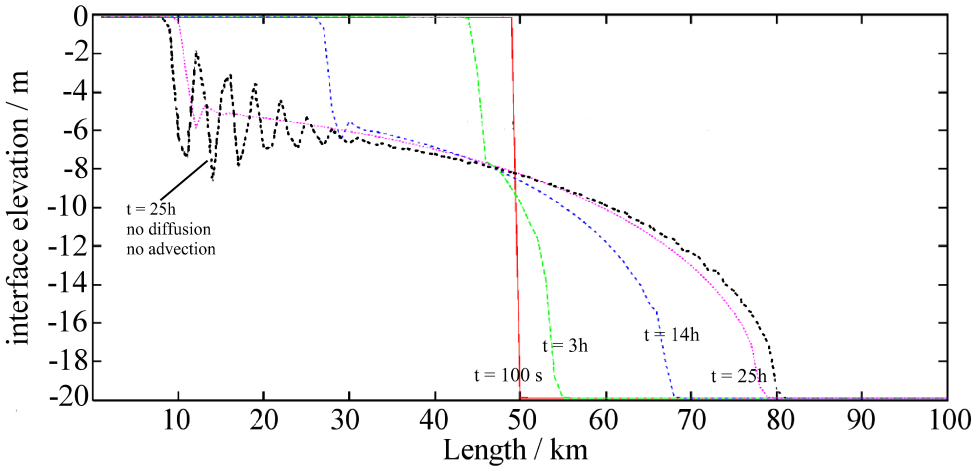

Figure 4.7: Propagation of plume in lock exchange experiment with bottom friction, horizontal momentum advection, horizontal momentum diffusion and the following parameters: Length = 100km, $H = 20$ m, $\Delta x = 1$ km, $\Delta t = 10$ s, $A_H = 10$ m^2 s^{-1}, $C_D = 0.0025$.

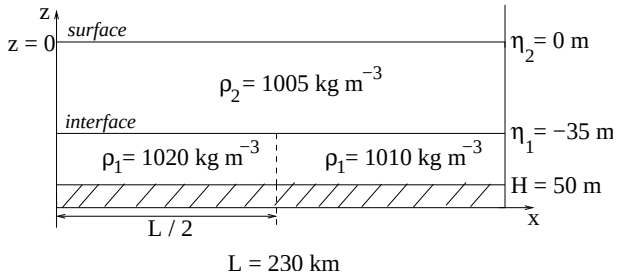

Figure 4.8: Schematic illustration of initial condition of density lock exchange experiment with the two layer model.

4.1.5 Lock exchange experiment with horizontal density gradient

In this section a test case with horizontal density gradient is implemented with the two layer model. This test shows how un-physically the model results can be with the assumption of mean physical values for a whole water column. For the simulation all terms of (2.64) are inserted and the entrainment process is neglected.

The initial condition (Fig. 4.8) is a surface elevation with $\eta_2(x, t = 0\text{ s}) = 0$m and a interface elevation with $\eta_1(x, t = 0\text{ s}) = -35$m. The model domain is a rectangular box with vertical walls with a depth of $H(x, t) = 50$ m and a length of 230 m. The first half of the lower layer ranging from $l = 0$ km to $l = 115$ km is filled with a fluid of $\varrho = 1020$ kg m^{-3} and the second half consists of water with $\varrho = 1005$ kg m^{-3} as shown in Fig. 4.8.

At $t = 0$ s the interface that separates the different fluids in the lower layer is removed. Instantly the first half of the interface between upper and lower layer ranging from 0 to 115 km declines from $\eta_1 = -35$ m to $\eta_1 = -38$m during the first 1.5 days. The second half of the interface between upper and lower layer ranging from $115 - 230$ km rises up from $\eta_1 = -35$ m to $\eta_1 = -30$ m. The pressure gradient, due to the initial condition with heavy water columns at the right and lighter at the left, produces a circulation from heavy to lighter water. Hence the strongest horizontal density gradient is displaced to the right. As a result of the initial condition of the sharp interface within the lower layer an internal wave with an amplitude of around 3 m and a surface wave with an amplitude of 25 mm as shown in Fig. 4.9b are generated. After only a few days of simulation the surface wave has not more than an amplitude of 2 mm. Due to the retarding effect of mainly bottom friction these waves are nearly eliminated after 20 days of simulation. After $t = 30$ days the simulation has reached a quasi-steady state as shown in Fig. 4.9a with a sharp gradient for the interface elevation and horizontal density contrast. Thus this state is balanced by the horizontal density gradient and internal pressure gradient. Low velocities from $u_1 = 0.2$ m s^{-1} down to $u_1 = 0.014$ m s^{-1} after $t = 30$ days do not allow any further advective or diffusive processes that could significantly change the interface elevation or horizontal density contrast.
A realistic result of a comparable simulation would not produce such a sharp gradient for the interface elevation and horizontal density distribution as stratification processes are not sufficiently resolved with this two layer model. A water column of the lower layer water of lighter water is for example directly mixed into a dense water column and not, as it is physically, expected flowing above the heavier fluid.

4.1.6 Application to Baltic Slice scenario

Within this section the model is being prepared for the so-called Baltic Slice scenario. This scenario represents a slice through the western Baltic Sea with corresponding basins, sills and channels as already shown in Fig. 1.3. This is also a very idealized but more practical test case as the previous ones where already some investigations about the Arkona inflow event can be done.
To run the model for Baltic Slice scenario some further adaptations should be made. For sloping bathymetry, the already introduced drying and flooding algorithm (Sect. 3.6.1) has to be inserted. With this algorithm it is guaranteed that the sea surface does not sink below the sea bed (Section 3.6.1). Additionally bottom friction is inserted under assumption of the logarithmic law at the bottom while previous chapter have used the constant value of 0.0025 for the bottom drag coefficient.
Some experiments with the Baltic slice bathymetry are shown in Fig. 4.10, Fig. 4.11 and Fig. 4.12. Fig. 4.10 demonstrates the different velocity of propagation under variation of the density contrast between the upper and the lower layer. The reason for this is the dependency on the reduced gravity parameter in the term $PRESSI$ in (2.64) that represents dynamics due to internal pressure gradients:

$$g^{'} = g\frac{\varrho_1 - \varrho_2}{\varrho_0} \tag{4.34}$$

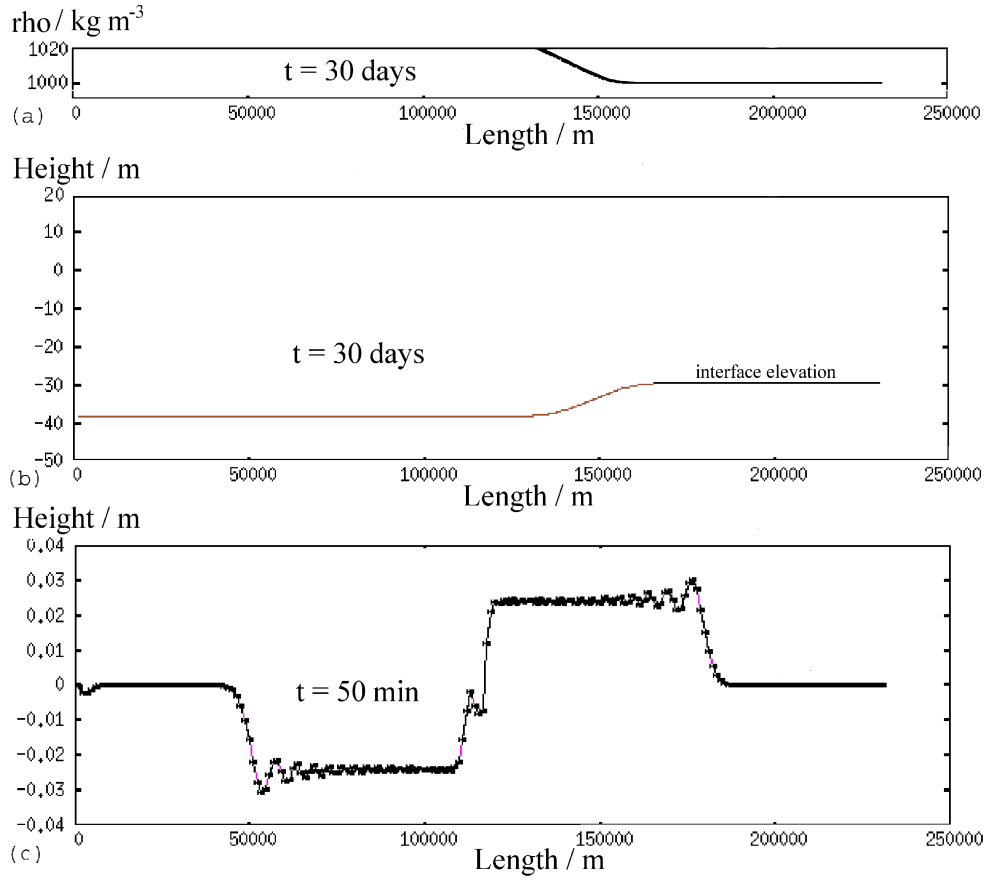

Figure 4.9: Plots after lock exchange test case with horizontal density contrast in the lower layer. (a) Density in lower layer. (b) The quasi-steady state after 30 days of simulation time for interface elevation and horizontal density distribution. (c) Picture showing the impact of the flow in the lower layer on the active upper layer.

where smaller density differences causes decreasing values for the reduced gravity parameter and hence for the velocity of propagation.
In Fig. 4.11 the surface elevation is shown with the corresponding velocities in Fig. 4.12. The surface elevation after 8.6 days very descriptive shows the influence of the lower layer on the upper layer. When the plume achieves higher velocities for the first time at the steep slope into the Arkona Basin, a hydraulic effect suddenly produces a decrease of surface elevation. Generally the surface elevation is lifted to the eastern side of the rectangular basin and decreasing to the western side. This makes the water even flowing back within the upper layer. This can be seen with a plot of the horizontal velocities u_2 after 93 days. But this effect is very small with surface elevations below half a millimeter and mean horizontal velocities of around -4 cm s^{-1}. The state after 79 days of simulation represents the surface elevation when the plume has already reached the Gotland Basin.
The velocities in the simulated plume as demonstrated in Fig. 4.12 are in the range of: $u_1 = 0.05...0.34$ m s^{-1} with the expected significant higher velocities at the steep slopes in the west of each basin. Interesting are the maximum values for the horizontal velocities in the lower layer. Even at the relatively long and steep inflow into the Gotland Basin the same maximum values for the horizontal velocity occurs for the lower layer compared with the inflow into the Arkona and Bornholm Basin. This indicates the balance between internal pressure gradient and bottom friction.

4.2 Experiments with Entrainment

In this chapter the entrainment assumption (2.62) is being inserted into the model and consequences to plume dynamics, horizontal and vertical distribution of the bottom current are shown.

4.2.1 Gravity current on linear slope topography

A basic test experiment with a gravity current on a linear slope topography is shown within this section. The impact of entrainment and consequences to the plume properties are demonstrated.
At the left boundary a fixed density contrast of $\Delta\varrho = 15$ kg m^{-3} between gravity current and ambient water is given. The interface elevation with $\eta_1 = -10$ m at the left boundary is fixed too.
The experiment simulates a gravity current with entrainment switched on and off. With entrainment and increasing time a head is forming that reaches nearly twice the layer thickness at the end of the slope (Fig. 4.13a). *Jungclaus* [1994] has shown that the thickness of the front of the plume for increasing slope angles reaches nearly four to five times the value of the following current. The effect of mixing in the head of the plume is being shown in Fig. 4.13c with plotting the density distribution every 8.3 hours. The difference between entrainment switched on and off is shown in Fig. 4.13a with the expected result, that the plume without entrainment is faster (*Jungclaus* [1994])

because the entrainment has a retarding effect dur to the entry of mass and momentum from the ambient lighter water. Generally the gravity current is driven by the downhill-slope force but the acceleration locally differs from the downhill-slope force due to the pressure gradient behind the head that even slows down the velocity of the plume. For both experiments with and without entrainment no decrease of velocity has been observed because of the balance between friction and pressure gradient.
Jungclaus [1994] has shown that for increasing slope angles from values of 0° to 1.25° the relation between front velocity and time tends to obtain constant slopes as seen in Fig. 4.14 (see also *Britter and Linden* [1980]). This means that for increasing slope angles the pressure gradient force is in balance with the retarding effects of bottom friction and entrainment. Values of up to 90° can not be reproduced with this hydrostatic numerical model. But the work of *Britter and Linden* [1980] has provided some noteworthy experiments for bigger slope angles ($5° - 90°$) as shown in Fig. 4.14. It is demonstrated that the front velocity of a plume under constant volume flux in the inflow area is nearly invariant with the variation of the slope angle. An increase of the slope angle induces a stronger entrainment rate E due to increasing acceleration on the slope while the entrainment on the other hand slows down the speed of the plume. Additionally the head of a plume as shown in Fig. 4.13 moves approximatively with 60% of the advective velocity of the following current (*Britter and Linden* [1980]). Thus the form of the head is mainly driven by the advection of water from behind the head into the head and the entrainment directly at the front of the plume with transport of mass and momentum from the comparatively less active lighter ambient water into the plume.

4.2.2 Lock exchange experiment with entrainment

This section covers a simulation of the so-called lock exchange experiment as it has already been discussed in Sect. 4.1.4 for a lock exchange experiment without entrainment. The simulation consists of a closed rectangular basin with a depth of 20 m and a length of 64 km. At $t = 0$ s the interface separating both fluids with a density difference of 5 kg m^{-3} is removed and the heavier water is flowing below the lighter water.
A simulation result of the lock exchange experiment with entrainment and the two layer model is shown in Fig. 4.15b together with the comparable GETM result (Fig. 4.15a). It can be seen very descriptive how different the results of the two layer model compared to the GETM simulation are. The disadvantage of the two layer model is the impossibility of a stratification consisting of more than only two layer in the vertical. Hence there is a strong mixing at the front over each water column representing the front of the plume. Heavier water from the left is directly advected into a water column of lighter water and not flowing below the lighter water. Thus the smaller vertical salinity gradient representing the GETM result is not being reproduced with the two layer model and mixing due to entrainment occurs mainly in the front of the plume.

4.2.3 Running Baltic slice scenario with two layer model and GETM

The Baltic slice scenario of chapter 4.1.6 is applied to show differences in the physics of the two layer model and the General Estuarine Ocean Model GETM (*Burchard and Bolding* [2002];*Burchard et al.* [2004]) for a simulation with entrainment. The GETM is a three-dimensional free-surface primitive equation model using the Boussinesq and boundary layer approximations. The model uses general vertical coordinates (see *Burchard and Bolding* [2002]) with the advantage that, especially for the simulation of bottom currents like plumes, these can smoothly advect along the bed.
Whereas the two layer model results are obtained with vertically integrated values for horizontal velocity and salinity within the plume, GETM for example resolves the vertical velocity shear in the bottom current due to the different impact of bottom friction or interfacial friction in vertical direction. These physical properties are included in the two layer model equation by in vertically integrated form. Turbulence to be generated because of denser water flowing above lighter water and contrariwise can also not be reproduced with the two layer model. A lighter water column in the lower layer is advected directly into a heavier water column. A consequence of this limitation of the two layer model is shown with the simulation of the Baltic slice scenario after one year of simulation (Fig. 4.16). In the Bornholm Basin a strong horizontal density gradient is observed that ranges from values of $S = 12$ psu at the left side of the Bornholm Basin to $S = 21$ psu at the right border. This horizontal density gradient is balanced by the pressure gradient force as seen with a steep slope in the values for the interface elevation η_1. This state after one year of simulation can be considered as a quasi-steady state. The horizontal velocities u_1 in the basins are very small with values of about $u_1 = 1\text{mm s}^{-1}$. Thus no further diffusive or advective processes can affect this balance between horizontal density gradient and pressure gradient.
Due to increasing velocities and small plume thicknesses of the plume flowing over the sills into the next basin, the impact of entrainment is high. Hence lighter water is being transported into the next basin. This effect is demonstrated in Fig. 4.16 for the one year simulation especially for the Bornholm and the Arkona Basin.
A dynamical investigation of the GETM result compared to the two layer model result is shown in Fig. 4.16b and Fig. 4.16c. It takes twice the time for the two layer simulated plume to reach the Gotland Basin as for the GETM-simulated plume. A conclusion would be that the rate of entrainment is not strong enough to lift the interface and makes the plume more easily pass the sills at the entrance of each basin. On the other hand, additional mixing causes decreasing values for the density contrast between plume and ambient water and is consequently reducing the velocity of propagation of the plume. The relation between velocity of propagation and density contrast has already been demonstrated in Fig. 4.10. Nevertheless the entrainment rate E is modified under multiplication by the factor 2.7 for test purposes. Astonishingly the same dynamic results for the GETM simulated (Fig. 4.16c) and the two layer model simulated plume (Fig. 4.16a) are obtained. But as expected, the salinity has not been improved simultaneously. With less entrainment, each basin is filled slowly with water and not until the median interface height within the basin reaches the top of the next

sill, the water is propagating further into the next basin. This tuning of the entrainment equation is made only for test purposes and not used for further simulations due to the fact that the entrainment formulation has been proved successfully with a set of experiments and observations.
The bathymetry of the Baltic slice scenario is far from realistic conditions and is only qualitatively showing the propagation and mixing of the plume trough the western basins of the Baltic Sea while propagating from basin to basin separated by shallow sills. The water passing the Bornholm Channel between the Arkona and the Bornholm Basin does not have such an unrealistic barrier as shown in Fig. 4.16.
The unexpected higher density values in the Bornholm Basin compared to the Arkona Basin (Fig. 4.16b) are due to the fact that the bottom water in the Bornholm Basin creates a more stable dense bottom pool compared to the Arkona Basin, as the effect of the Sill is much stronger than for the Arkona Basin and hence more volume is fixed in the Bornholm Basin (*Kõuts and Omstedt* [1993]). This salinity differences have also been observed in nature because the Bornholm Basin has a sill that the Arkona Basin does not have. The sill of the Arkona Basin in the Baltic slice scenario is much too disproportionated. Meanwhile the water in the first basin is delivered with very shallow water from the plane at the left border that is, while running down the first slope, being mixed with the ambient water of $S = 8$ psu from $S = 25$ psu to $S = 12$ psu. Meantime the water in the second basin remains nearly in the same state like it has been at the beginning because of reduced dynamics and high amounts of heavier water lying in the Bornholm Basin.
A deeper investigation of the entrainment of the two layer model plume compared with the GETM simulated plume needs to identify the interface in the GETM result. Therefor the highest salinity gradient in a water column must be identified. The result is plotted in Fig. 4.16c with black dots for the obtained interface in the GETM simulation. A comparison with Fig. 4.16b shows a very good agreement in interface elevation and salinity values in the Arkona Basin with mean salinity values of 20 psu for the GETM result and 21 psu for the two layer model result. The assumption of a two layer system makes the two layer model results completely different to the GETM result. The red arrow in Fig. 4.16c shows with the help of the obtained interface how heavier water is moving below lighter water, a process not being resolved with the two layer model.
With a 3D bathymetry for an idealized simulation of the inflow event it is demonstrated in Chapt. 5 that it took about 10 days for the plume to cross the Arkona Basin and enter the Bornholm Basin. The Baltic Slice scenario predicts less than 4 days for this propagation. Due to additional pressure gradients in zonal direction the plume and hence the spreading in two horizontal directions, the Baltic Slice is not comparable with a simulation under use of a 3D bathymetry.

4.3 Basic test experiments with 3D model

This section covers a set of basic test experiments with the 3D two layer model. All these experiments are implemented under use of a linear slope topography as shown in Fig. 4.17. The impact of Entrainment, Bottom Friction and Rotation on plume dynamics and properties is being demonstrated and discussed.

4.3.1 Propagation of plume with entrainment and without rotation

For the simulation of the intrusion of dense water without entrainment on a slope with the 3D two layer model a density contrast of 5 kg m^{-3} and a plume thickness of 100 m is given at the inflow area. Contour plots of the current velocity, density contrast and plume thickness are shown in Fig. 4.18.
Due the the additional zonal pressure gradient in zonal direction the plume dispreads laterally. A head is forming with a significantly higher plume thickness. The mushroom-shaped front (Fig 4.18)a of the plume is a commonly obtained state for intrusion experiments.
On the basis of the output of this experiment the symmetry of the model equations in spatial $x-$ and $y-$ direction can be demonstrated with the results of density distribution, current velocity and plume thickness in Fig. 4.18a-d.
The highest velocity values (Fig. 4.18c-d) are obtained in the inflow area with corresponding highest values for the density contrast (Fig. 4.18). Due to the dependency of the entrainment rate E with the current velocity (2.52), the entrainment process is very strong in the inflow region.
The contour lines in Fig. 4.18b are not in correlation with the plume thickness shown in Fig. 4.18a. This indicates that the head of the plume mainly develops due to the advection of water mass from behind the plume head (*Britter and Linden* [1980]) and less due to the entrainment process.

4.3.2 Variation of bottom friction with rotation and without entrainment

The effect of bottom friction on a dense bottom current driven by Coriolis force and pressure gradient force is investigated. Therefor the same initial conditions as in the previous section are applied. The entrainment is not implemented as this test case wants only to extract the consequences of bottom friction to gravity current dynamics without having additional interactions and dynamics due to vertical mixing.
While changing the values for the bottom drag coefficient C_D, as seen in Fig. 4.19, the dissipative effect of friction under increasing values for C_D is clearly demonstrated. The more interesting effects for increasing bottom drag coefficients are the main propagation direction and obtained smaller thickness values at the left lateral boundary of the flow. The main propagation direction of the plume depends on the impact of the bottom friction force. The dissipation due to bottom friction reduces the propagation velocity and hence causing a decrease of the Coriolis force. For a flow along a continental shelf

the geostrophic balance:

$$\begin{aligned} -fv &= -\frac{1}{\varrho_0}\frac{\partial p}{\partial x} \\ fu &= -\frac{1}{\varrho_0}\frac{\partial p}{\partial y} \end{aligned} \tag{4.35}$$

induces a propagation direction along lines of constant depth. In nature the descent of this current crossing lines of constant depth occurs due to bottom friction. For realistic values for the density contrast of such bottom currents at continental shelfs *Griffiths* [1986] has shown that only very huge slope angles could induce a flow down the slope. Thus the test case of this section shows that bottom friction can stop a bottom boundary current from attaining geostrophic balance (*Smith* [1975]). Recapitulating this means that for small friction the flow is mainly geostrophically driven and for strong friction the flow sets on down the slope under decreasing velocity of propagation.
Due to the downhill-slope force the isolines for the plume thickness at the right lateral boundary of the plume in flow direction are very close to each other while the isolines at the left lateral boundary are diversified.
The impact of the bottom friction force is stronger for smaller plume thicknesses. Thus different directions for the current velocity close to the bottom are obtained compared to the upper parts of the plume. This distribution for the horizontal velocity component can not directly be reproduced with the two layer model. But this physics is included in vertically integrated form.
It is also noteworthy that the propagation angle of these bottom currents balanced by pressure gradient, Coriolis force and bottom friction have been used to obtain the bottom drag coefficient (*Bowden* [1960]). But the qualitative result of these investigations is problematic concerning the problems measuring the density contrast, propagation angle and plume thickness not only because of the different gradients of density and plume thickness at the lateral boundaries.

4.3.3 Conclusions

The basic test experiments have demonstrated that the two layer model resolves the basic properties of a gravity current. The dense bottom current is being diluted by the ambient water and is hence reducing the velocity of propagation due to decreasing values of the density contrast. At the front of the plume a head is forming due to entrainment. This mixing in the head decreases the velocity in the front and advects water from behind the head into the head. This has also been demonstrated with the the 1 1/2 layer reduced gravity model (inactive upper layer) of *Jungclaus* [1994] and in the work of *Britter and Linden* [1980]. For a gravity current in a rotating frame the is balanced between pressure gradient force, Coriolis force and bottom friction force. Increasing influence of the bottom friction force drives the plume down the slope across contours of constant depth.
It is noteworthy that some experiments have shown a significant impact of the bottom current on the upper layer and contrariwise (Fig. 4.5; Fig. 4.11; Fig. 4.12). The

obtained values for the velocities in the upper layer during the Baltic Slice scenario (Fig. 4.12) have shown that even for a relation of $h_2/h_1 = 2.5$ between the thicknesses of the upper and the lower layer in the Bornholm Basin the interaction between both layers is not negligible. The Arkona Basin, where the interaction is even stronger due to maximum depth values of only 48 m (max. depth in Bornholm basin: 92 m), is the basis for closer investigations of inflow events within this thesis (Chapt. 5). Thus the application of a two layer model with two active layers might be forceful necessary. The use of a 1 1/2 layer model with an inactive upper layer as applied for the Denmark Strait Overflow (*Jungclaus* [1994]), where the ratio between the thickness of the lower and upper layer is small and interaction can be neglected, is not suited to simulate inflow events in the Baltic Sea (mean depth: 52 m) and observed plume thicknesses between 5 and 15 m (*Lass and Mohrholz* [2003];*Burchard et al.* [2005]) for the plume in the Arkona Basin.

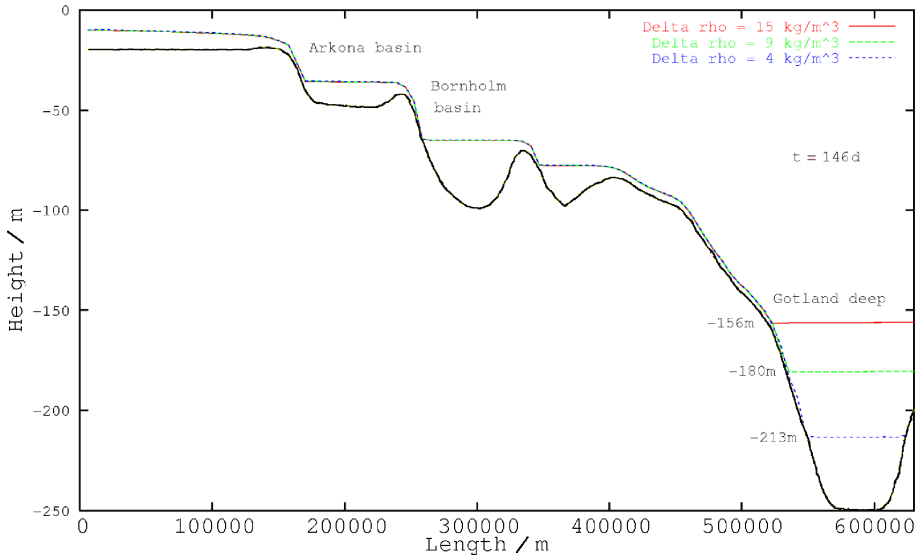

Figure 4.10: Plume after 146 days of simulation under variation of the density contrast between upper and lower layer.

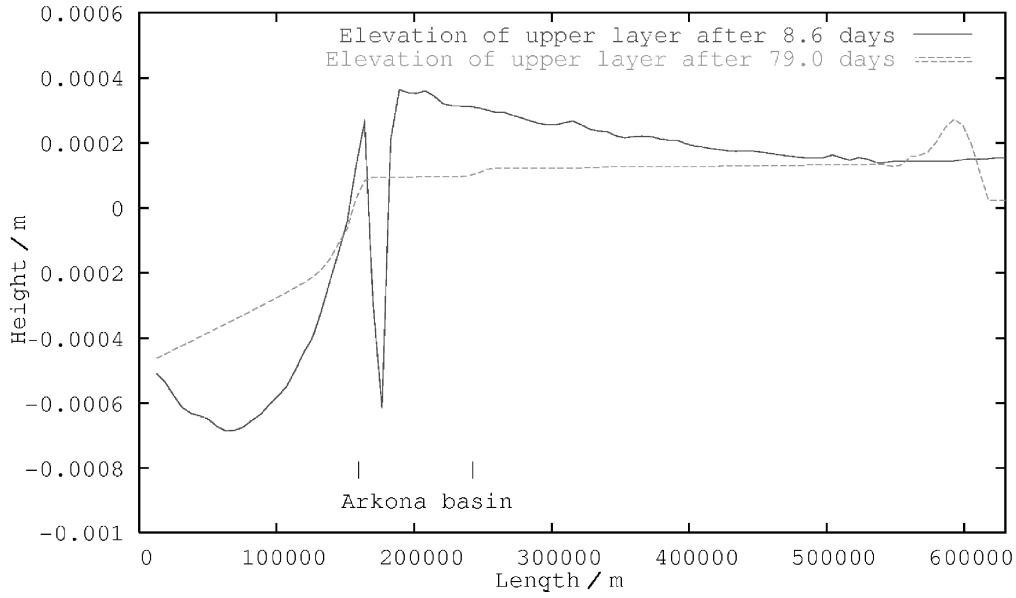

Figure 4.11: Sketch showing the elevation of the surface during the Baltic Slice scenario.

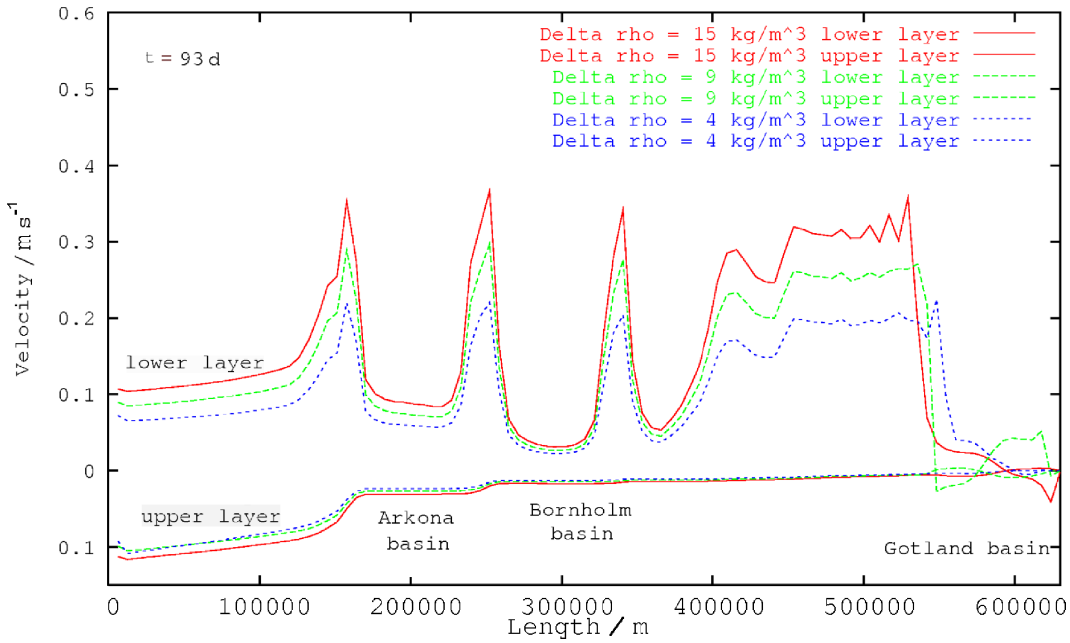

Figure 4.12: In this pattern the velocities of both layers after a simulation time of 93 days are shown. Significantly higher velocities at every steep point of the bottom topography can be seen. For illustration there are some basins given in the sketch. Also the interaction between upper and lower layer is well demonstrated for the area of the Arkona Basin.

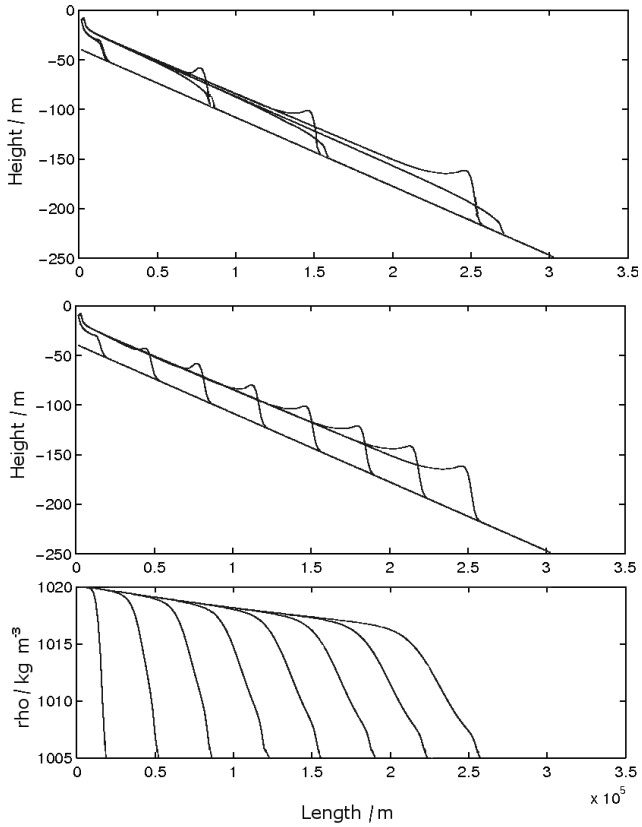

Figure 4.13: Gravity current on a slope with the latest state after $t = 2.4$d. (a) Sketch showing the plume with and without entrainment. (b) With entrainment: Formation of a head that increases with time (used time interval for plot: $\Delta t = 8.3$ h). (c) Time series of densities for simulation with entrainment. The mixing process directly at the front of the plume, where densities close to the density values of the ambient water can be found, is shown. Interesting is the nearly linear increase of density from $\varrho = 1006\text{kg m}^{-3}$ up to $\varrho = 1014\text{kg m}^{-3}$.

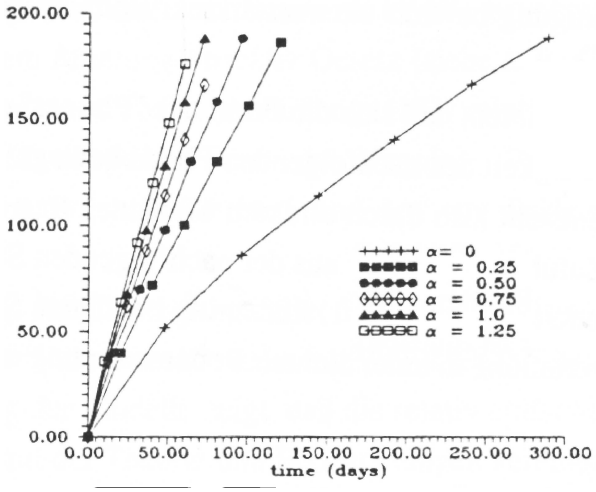

Figure 4.14: Front position of a plume under different slope angles plotted over time. Picture taken from *Jungclaus* [1994].

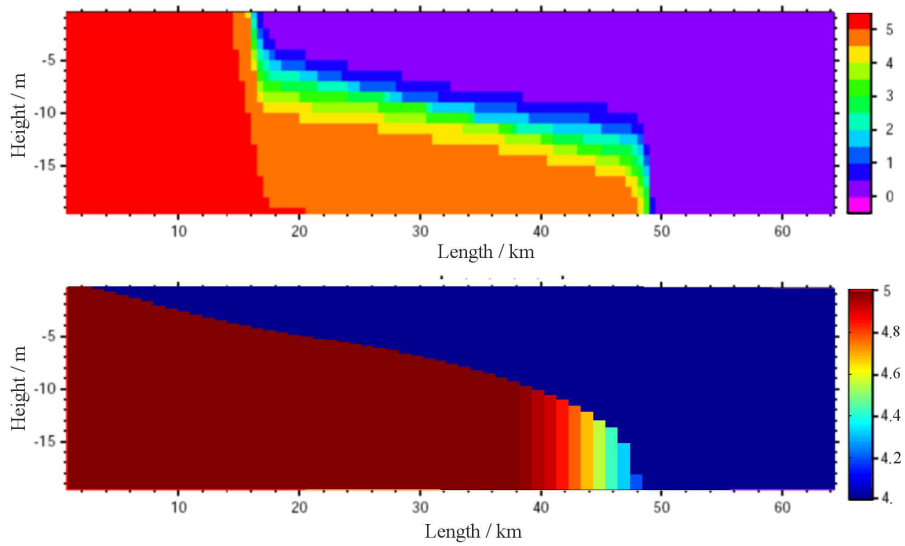

Figure 4.15: Lock exchange experiment with GETM (upper panel; picture taken from *Burchard and Bolding* [2002]) and the two layer model (lower panel) for a density contrast of 5 kg m^{-3} at $t = 0$ s.

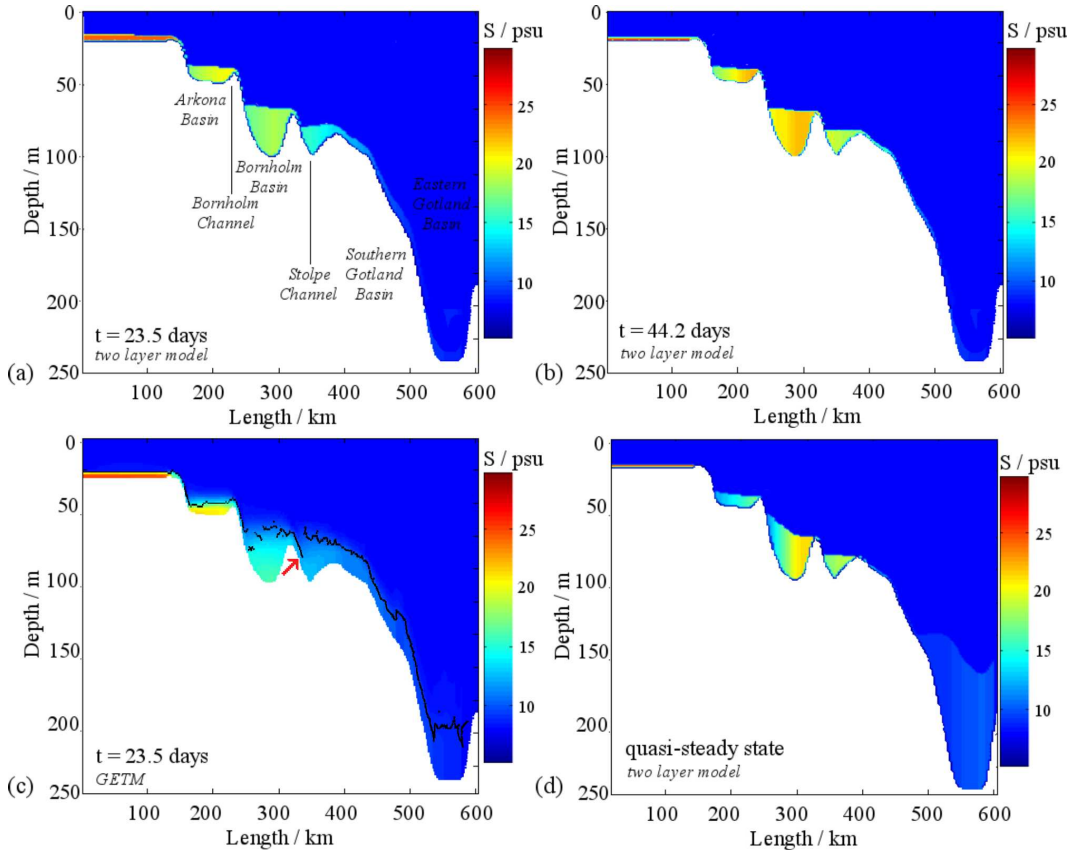

Figure 4.16: (a) Baltic slice scenario after 44.2 days of simulation with the two layer model under modification of the implemented entrainment formulation. (b) Baltic slice scenario after 22.6 days of simulation with the two layer model. (c) Baltic slice scenario after 22.6 days of simulation with GETM together with obtained interface (black dots). (d) Quasi-steady state after one year of simulation with the two layer model. Additionally the horizonal velocity in the plume is plotted.

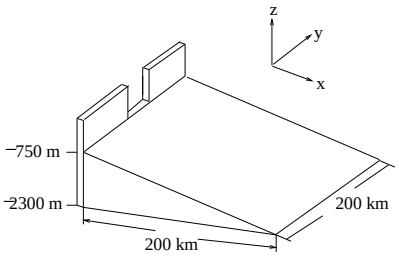

Figure 4.17: Linear slope topography for basic model experiments with 3D two layer model.

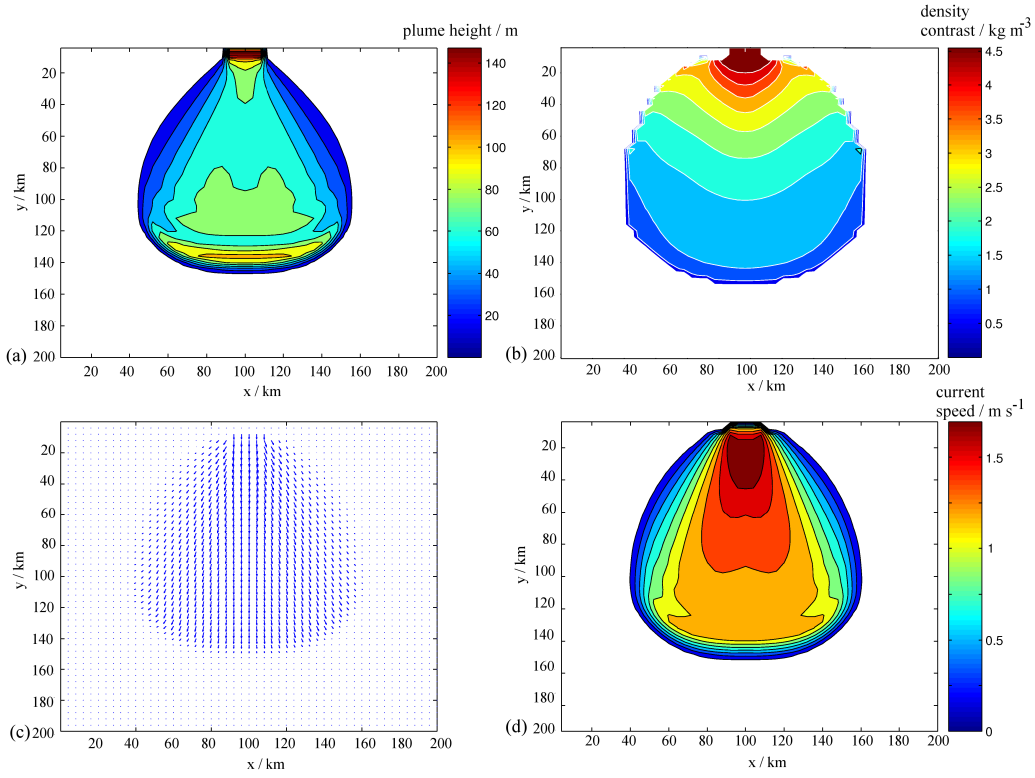

Figure 4.18: Picture showing the propagation of a bottom current after 4 days of simulation time. (a) Plume height; (b) Density contrast between upper and lower layer; (c) Vectors of current speed and (d) Current speed in lower layer.

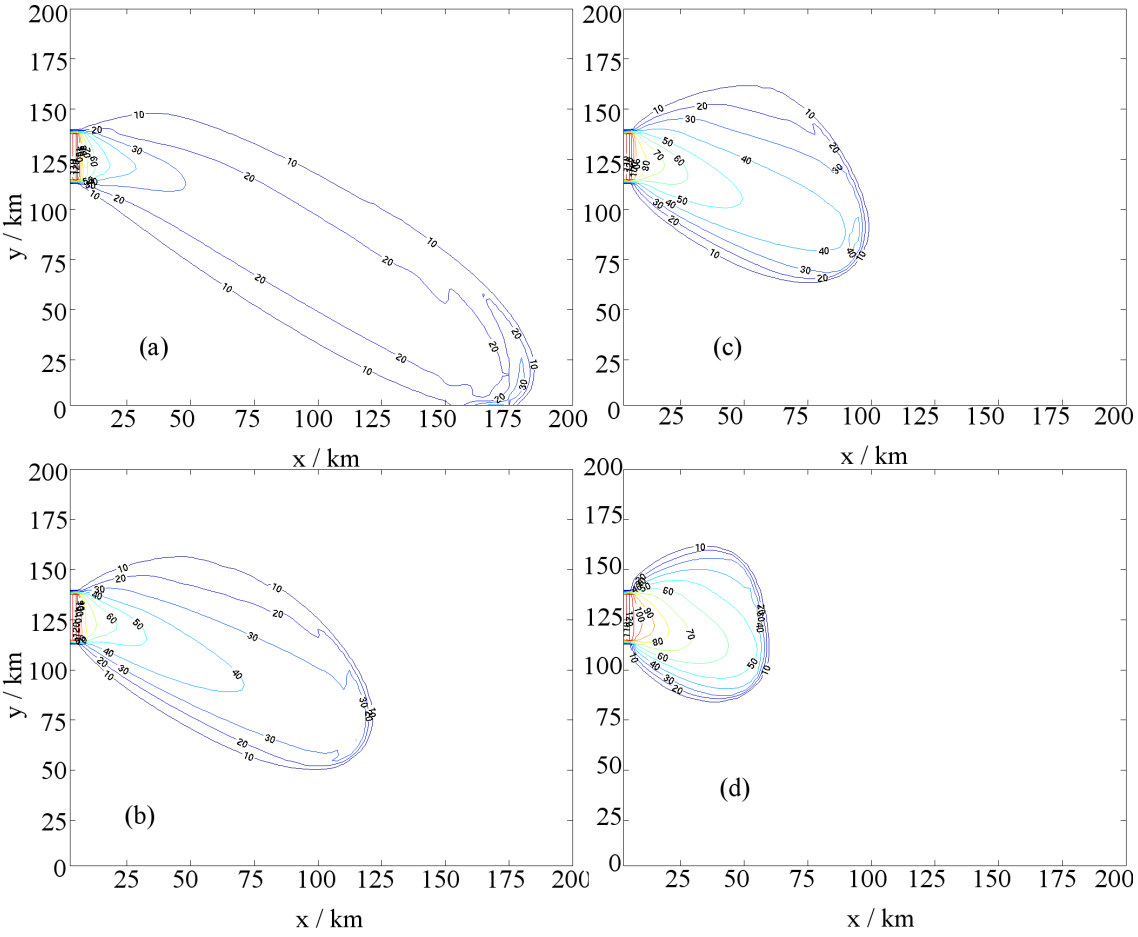

Figure 4.19: Interface elevation of plume on linear slope topography with rotation under variation of the bottom drag coefficient with values of: (a) $C_D = 0.001$, (b) $C_D = 0.005$, (c) $C_D = 0.01$ and (d) $C_D = 0.05$.

Chapter 5

Simulation of Baltic Sea inflow event

The reduced gravity and Boussinesq-approximated 3D two layer model is now applied to simulate an idealized Baltic Sea inflow event. The importance of plumes for the ecosystem Baltic Sea has been discussed in Chapt. 1. Hence various investigations of inflow events exist with the help of measurements (*Lass and Mohrholz* [2003];*Burchard et al.* [2005];*Kõuts and Omstedt* [1993];*Matthäus and Franck* [1992];*Liljebladh and Stigebrandt* [1996]) and theoretical considerations (*Burchard et al.* [2005];*Kõuts and Omstedt* [1993]). These are compared with two layer model results to demonstrate accordances and nonconformities.
Additionally some experiments under variation of model parameters like $Froude$ number (2.54) and bottom roughness length z_0 are demonstrated to point out the sensitivity of the model results on these model parameters. Furthermore two different assumptions for the calculation of the bottom drag coefficient are compared.

5.1 Model setup and initial conditions

The bathymetry now used for the simulation of the Baltic Sea inflow event is shown in Fig. 5.1a. The model domain covers a range of around $315x165$ km from $11.0° - 16.0°$ East and $54.0° - 55.8°$ North. This model domain has a resolution of $0.5x0.5$ nm (nautical miles) and is applied to obtain two layer model results that can be compared directly with the recent work of *Burchard et al.* [2005]. Observations together with model simulations for this bathymetry have been demonstrated and discussed there.
Later on the bathymetry is extended to a bathymetry ranging from $9.0° - 15.0°$ East and from $53.5° - 56.5°$ North as shown in Fig. 5.1b. A resolution of $0.5x0.5$ nm is used for discretizing the model equations. This bathymetry is additionally applied to obtain model results that also identify plumes crossing the Danish Belts. These are excluded during simulations with the smaller bathymetry as shown in Fig. 5.1a.
The initial condition for the simulation of the Arkona inflow event is a constant interface elevation with $\eta_1 = -D_{min} = -0.02$ m (see Sect. 3.6.3) at the northern model

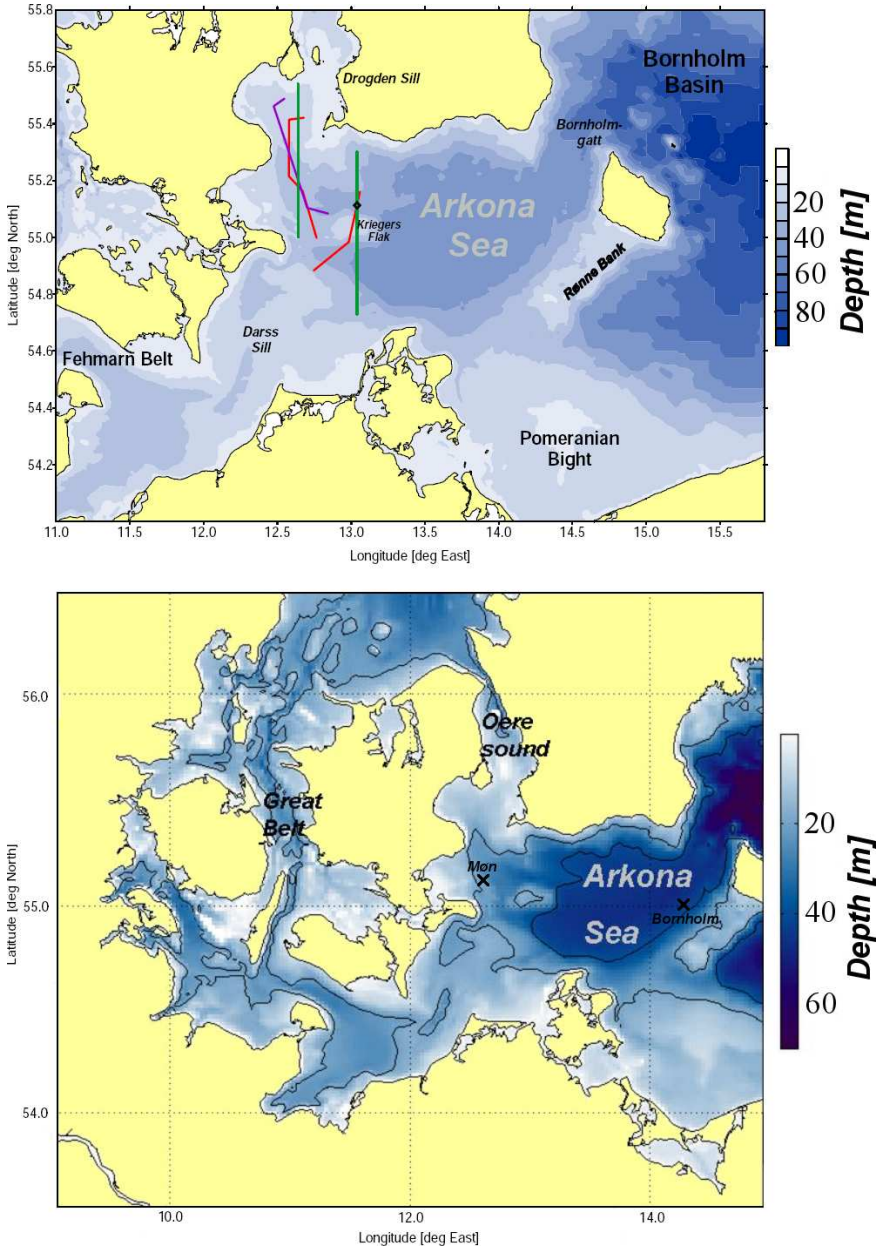

Figure 5.1: (a) Bathymetric maps of the Arkona Sea with the two cross sections south of Drodgen Sill and across Kriegers Shoal indicated by the two green lines. These slices are part of a model comparison in Sect. 5.2 of the two layer and the GETM (*Burchard and Bolding* [2002]). The purple and red lines show the tracks for the observational sections (purple line: Feb 1 from 16:20 to 20:41 h; western red line: Feb 2 from 10:24 to 14:47 h; eastern red line: Feb 5 from 10:45 to 15:31 h). Picture taken from *Burchard et al.* [2005]. (b) Extended bathymetry for model simulations that additionally resolves the plume crossing the Great Belt and Fehmarn Belt and finally the Darss Sill into the Arkona Basin. The crosses mark the hydrographic stations Møn and Bornholm.

domain boundary in the Oeresound. It simulates an inflow event with a fresh water inflow of 25 psu. The rest of the domain is filled with water of 8 psu which is a realistic assumption for the brackish surface water of the Arkona Sea (*Liljebladh and Stigebrandt* [1996]; *Burchard et al.* [2005]).

5.2 Comparison of two layer model results to GETM

Based on the work of *Burchard et al.* [2005] direct comparisons between the GETM (*Burchard and Bolding* [2002];*Burchard et al.* [2004]) and the two layer model for cross sections of the plume are made for a region south of Drodgen Sill at 12°30′E and a north-south transect across Kriegers Shoal at 13°E. On this note, differences in plume velocity, salinity and thickness are pointed out and reasons for different model results are discussed.
For a direct comparison of the two layer model results with model results from a different ocean model, the idealized Arkona inflow event is additionally simulated with the GETM (*Burchard and Bolding* [2002]). The GETM is a three-dimensional free-surface primitive equation model using the Boussinesq and boundary layer approximations. The model uses general vertical coordinates (*Burchard and Bolding* [2002]). The advantage is a more smoothly advection of saline bottom currents moving along the bed. Furthermore the GETM model results are interesting, because they additionally deliver informations about velocity shear and stratification within the plume. On the other hand the GETM resolves the sharp salinity gradients in the interface not as observed, as it can be seen in 1.4. The two layer model reproduces the sharp gradient more sufficiently.
The idealized simulations have been compared with recent observations investigated in January and February 2004 in the work of *Burchard et al.* [2005]. Additionally the two layer model is applied to confirm with or even enlarge the results at hand. For the discretisation of the Arkona inflow event, a high-resolution bathymetry with 0.5 nm (nautical miles) is used for the GETM as well as for the two layer model. The GETM setup has been implemented under disregard of surface and boundary heat fluxes. A vertical resolution of 25 layers has been applied. Bottom- and surface-fitted coordinates (*Burchard and Bolding* [2002]) are used and the bottom layer thickness is horizontally homogeneous with a value of 0.4 m. As it has already been mentioned this allows a good resolution of plumes on slopes.
Open boundaries can be found at the northern end of the Sound, towards the West across the Fehmarn Belt and towards the East along 14°46′E.
The model forcing for the idealized simulation with GETM is nearly the same as for the two layer model. At the North of the Oeresound towards the Kattegat the surface elevation is slightly increased by 0.02 m whereas the surface elevation at the other open boundaries is set to zero-level. The whole domain is filled with water of 8 psu whilst the inflowing water in the North of the Sound has a salinity of 25 psu. The only difference between the model forcing of both the GETM and the two layer model is, that for

the GETM a spatially and temporally homogeneous wind stress of 0.22 N m^{-2} from south-west (240°) is assumed. For the two layer model no wind stress is applied to the model equations. This feature was not included at this state of the two layer model. Further investigations about the influence of surface stress τ_s on the two layer system have to be done.

5.2.1 Modeling the Arkona inflow event

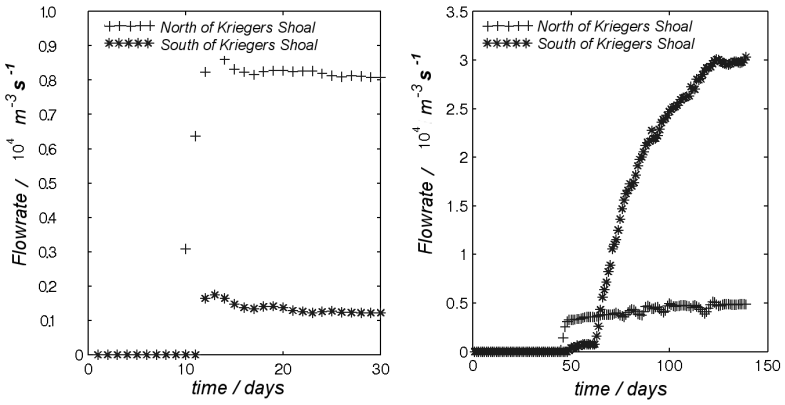

Figure 5.2: (a) Time series of flowrates north and south of Kriegers Shoal for the plume from Drodgen Sill (a) without and (b) with involvement of the bottom current crossing Drodgen Sill.

Within the first five days of simulation (Fig. 5.3), the plume has already passed the Drodgen Sill and filled the Sound with high-salinity water of $22 - 25$ psu. The lateral boundaries of both modeled plumes are very similar to each other with some less significant salinity differences in the region of the Drodgen Sill.
After 15 days of simulation a merging and splitting process of the bottom current occurred due to Kriegers Shoal. Kriegers Shoal itself is fully surrounded by saline bottom water of 12 psu (GETM: 15 psu) in the south and 18 psu (GETM: 22) psu in the north. There seems to be a big difference, but as Fig. 1.4 proves, the interspace of both GETM and two layer model graph to the observations is nearly equal. As it can be seen further on with the help of the contour lines, the geographical region of the merging process of the northern and southern branch takes place in the south-east of Kriegers Shoal.
At the same time significant differences in the salinity values of both model solutions are apparent. The Drodgen Sill seems to be a comparatively bigger barrier for the two layer simulated bottom current. A weaker plume thickness on top of Drodgen Sill induces stronger entrainment rates, which might be an explanation. Moreover the horizontal salinity gradient at the front and lateral boundaries of the plume is much higher for the GETM-simulated plume. Nevertheless both model solutions are still in agreement with respect to the velocity of propagation and lateral broadening of the plume. An inspec-

tion of the salinity of the northern compared to the southern branch around Kriegers Shoal shows, that most of the flow propagates north of Kriegers Shoal. This flow regime is unexpected, because a mainly geostrophic propagation of the plume would result in a current with a stronger southern branch. Due to the narrow channel west of Kriegers Shoal the flow in the southern branch is hydraulically limited. Referring to this, the GETM-simulated flow and the two layer simulated flow are in agreement. For a direct comparison of the transports north and south of Kriegers Flak see Fig. 5.2a.
Fig. 5.2a and 5.2b demonstrate the difference in flowrates for the northern and southern branch of Kriegers Shoal simulated with the two different bathymetries (see Sect. 5.1). Fig. 5.2b additionally resolves the flow over the Danish Belts that finally has to pass the Darss Sill to fill the Arkona Basin with saline water. After 65 days of simulation with the extended bathymetry a suddenly increased flowrate for the southern branch south of Kriegers Shoal (Fig. 5.2b) occurs. It is noteworthy that the northern branch is not affected. The difference in flowrates for the northern branch with 8000 $m^3\ s^{-1}$ in Fig. 5.2a and 5000 $m^3\ s^{-1}$ in Fig. 5.2b is due to the different plume thicknesses at Drodgen Sill. The initial condition for the simulation with the smaller bathymetry has a fixed interface elevation in the north of the Oeresound. This interface elevation is not reached for the simulation under use of the extended bathymetry (Fig. 5.1) in quasi-steady state. Consequently the flow rates for the bottom current crossing the Drodgen Sill are smaller. The ratio of the flowrate between the northern and southern branch has a relation of 6.75 : 1 for the process of saline water coming from the Oeresund. The result with the additional plume from the Darss Sill, that joins the flow southern of Kriegers Shoal, turns over the ratio to the relation of 1 : 6.
It is noteworthy that the GETM-simulated plume advects more along the Danish coast (see yellow arrow in Fig. 5.3). The reason might be that the GETM-simulated plume is comparatively more geostrophically driven with less influence of bottom friction.
The velocities within the plume after 17 days are plotted in Fig. 5.5. Fig. 5.5 demonstrates that the lateral broadening in the east of Kriegers Shoal slows down the plume in the Arkona Basin with mean velocities of 6 cm s^{-1}. At steep slopes, mainly to be found between Drodgen Sill and Kriegers Shoal, velocities of up to 0.35 m s^{-1} occur. Peak values for the velocities northern of Kriegers Shoal are nearly three times bigger than in the south.
After 30 days of simulation the plume covers most of the Arkona Sea and has already passed the Bornholm Channel. The state can be considered as a quasi-steady state (Fig. 5.4) as the lateral boundaries, transports and plume thicknesses (Fig. 5.4) have reached their maximum values. The state is now balanced by topographic (hydraulic limiting) features, the entrainment process, bottom friction, Coriolis force and pressure gradient. Both model solutions remain in agreement concerning lateral boundaries and velocity of propagation. Despite these similarities, the entrainment process is significantly different between both model solutions. Due to the fact that the GETM result represents the bottom salinity and the two layer model output represents the vertically averaged salinity, higher values of salinity for the GETM simulation are comprehendible. Hence relative differences between salinity values of the different plumes could give a more proper conclusion of the differences in the mixing processes. With arbitrarily cho-

sen points in the west of Kriegers Flak and close to the Bornholm Channel a salinity difference of 6 psu is obtained for the two layer model result and 5 psu for the GETM-simulated plume. Further investigations of the GETM result have to be done under calculation of vertically integrated values for salinity, velocity and plume thickness. A direct comparison of the bottom salinity of the GETM model result with the vertically averaged variables of the two layer model result is complicated. The velocities close to the sea bed within the plume are influenced by bottom friction. Ekman physics is included in the two layer model equations only in a vertically integrated form. Additionally, different assumptions for the entrainment rate E (see *Bo Pedersen* [1980a]; *Oguz et al.* [1990]; *Baringer and Price* [1990]) have to be tested with the model.
Another striking point of the model result is the flow around Kriegers Shoal with a depth of partially less than 20 m surrounded by water depths of more than 40 m. Over the whole simulation, the salinity on top of Kriegers Flak remains constant with values of 8 psu. These water masses are consequently not influenced by the plume when considering these idealized model simulations. Even the additional flow over the Darss Sill does not affect the water masses on top of Kriegers Shoal (Fig. 5.16).
Lass and Mohrholz [2003] assumed that for a mainly geostrophic propagation the plume propagates south of Drodgen Sill along the Danish coast and west of Kriegers Flak in order to propagate along the southern boundary of the Arkona Basin over the Bornholmgatt into the Bornholm Basin. As it has already been considered by *Burchard et al.* [2005] the flow must be assumed to be also significantly influenced by bottom friction. This conclusion is clearly confirmed by idealized two layer model experiments (Sect. 4.3). A significant impact of bottom friction will force the plume to cross lines of constant depth with a resulting flow down the slope.
As it was suggested in *Burchard et al.* [2005], the stationary model forcing may be to far from realistic conditions. In the following sections two slices south of Drodgen Sill and across Kriegers Flak are investigated for a direct comparison to observations.

5.2.2 Velocities of bottom track of the plume

Due to the main forces, as there are bottom friction, Coriolis force and pressure gradient force, the bottom current follows a specific track (Fig. 5.6) from south of the Drodgen Sill crossing the Arkona Basin up to the Bornholm Channel. With the help of the idealized Arkona inflow event simulation the main track of the plume is obtained by identifying the highest salinity values in the propagation direction. Hence the specific bottom track is obtained and shown in Fig. 5.6.
Fig. 5.7(a) shows a Hovmueller diagram of salinity plotted over time and distance during a realistic simulation implemented by *Janssen et al.* [2006]. A specific velocity of propagation (Fig. 5.7(b)) can be found for different intensive inflow events. As shown in Fig. 5.7(c) this is also reproduced quite well by the two layer model for the idealized inflow event simulation.

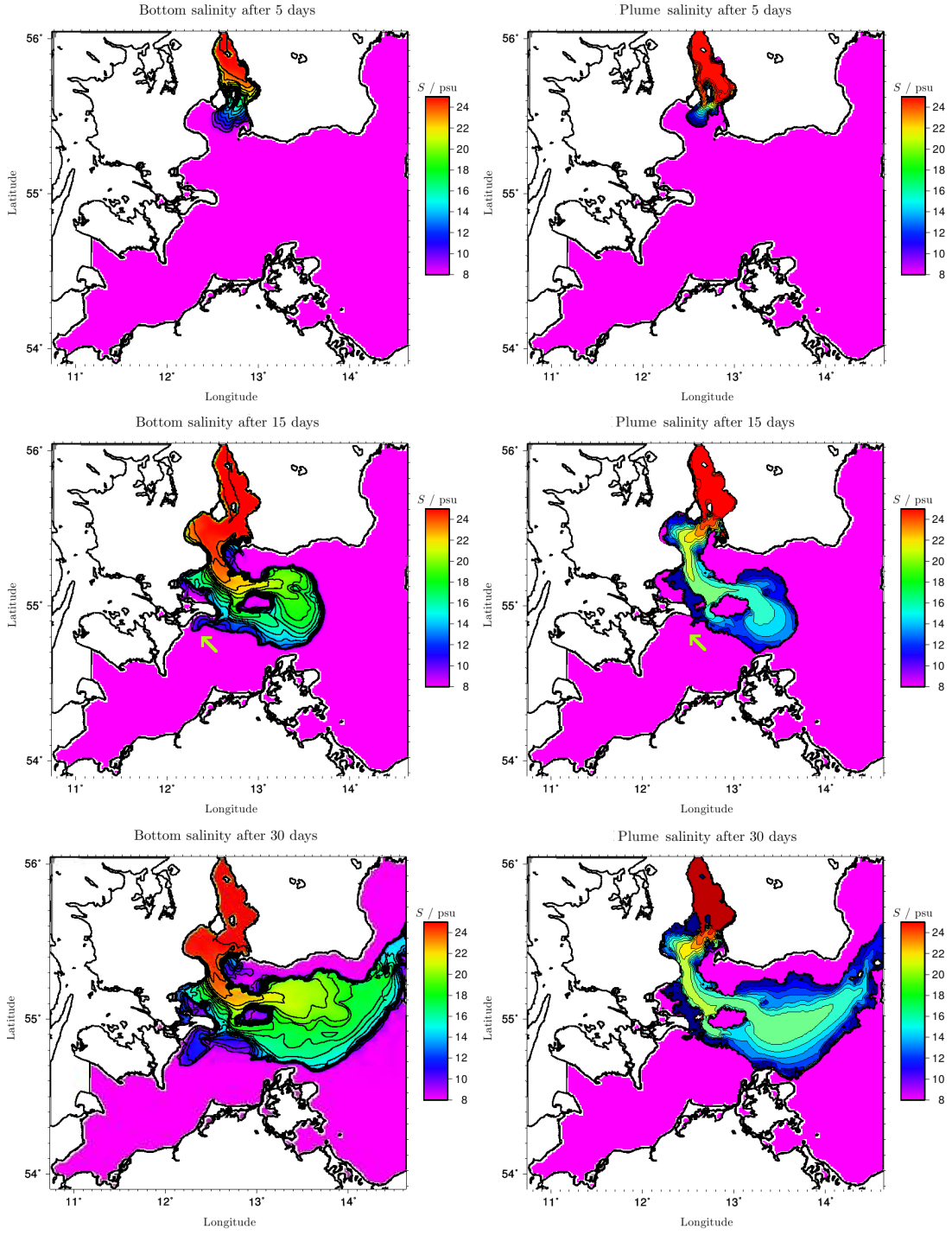

Figure 5.3: GETM-simulated near-bed salt distribution (left panels) and plume salinity simulated with the two layer model (right panels). Note the good agreement of both model solutions seen in comparison of the lateral boundaries of the plume.

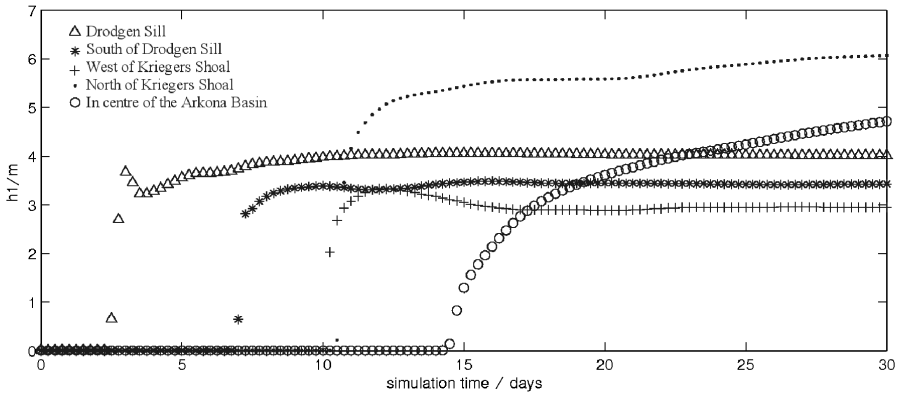

Figure 5.4: Simulated plume thickness at arbitrarily chosen points near Drodgen Sill, Kriegers Flak and the Arkona Basin to show that a quasi steady state occurs after about 30 days of simulation.

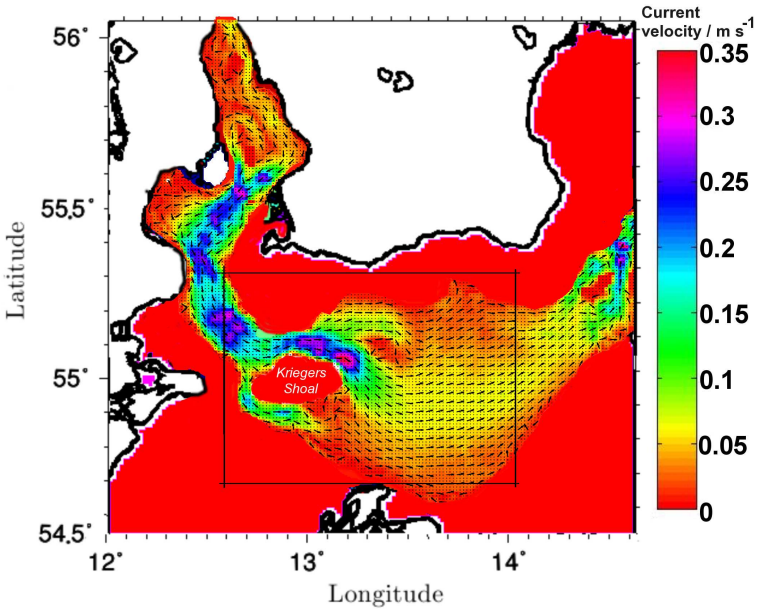

Figure 5.5: Current velocities of plume after 28 days of simulation. The framed area symbolizes the extracted region for further investigations of plume dynamics at around Kriegers Shoal in Sect. 5.3.1

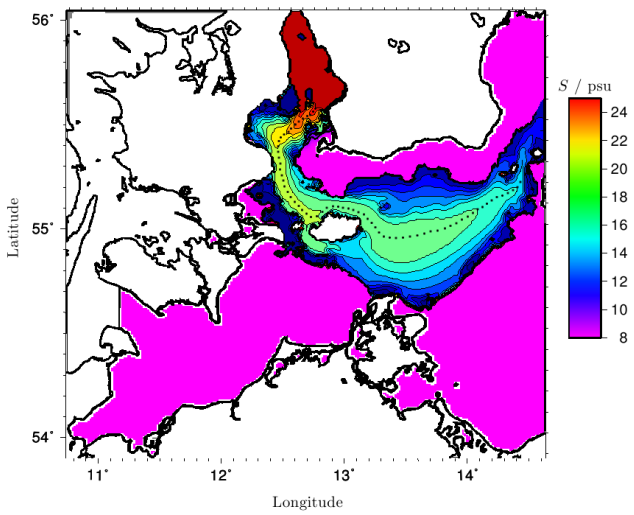

Figure 5.6: Picture showing the track of obtained maximum values for salinity of the plume during the Arkona inflow event.

5.2.3 Compare different bottom drag assumptions

The assumption of a logarithmic law at the bottom and the resulting dynamic calculation of the bottom drag coefficient 2.46 is now compared to a simulation under use of a constant bottom drag coefficient with $C_D = 0.0025$. The results of both model simulations are shown in Fig. 5.8 with the differences between both simulations being only marginal. As shown in Fig. 2.2, values of around $C_D = 0.0025$ are obtained for plume thicknesses of 5 m. This is a mean value for the plume thickness modeled with the two layer model. Hence the mean value for the bottom drag coefficients is very similar to $C_D = 0.0025$. Calculations of differences in salinity, plume thickness and flowrates have shown only small differences. Maximum salinity differences between both assumptions of only 0.4 psu occurred. Differences in values for the plume thickness were below 0.6 m.

Additionally the bottom roughness length has been changed from $z_0 = 0.001$ m to $z_0 = 0.01$ m. An inspection of Fig. 2.2 shows that for the same values of the plume thickness, the bottom drag coefficient is nearly doubled for a bottom roughness length of 1 cm. A simulation result has shown differences of more than 20% for the velocity of propagation between $z_0 = 0.1$ cm and $z_0 = 1$ cm. A consequence would be, that the two layer model results could be more realistic when applying different bottom roughness lengths within the model domain.

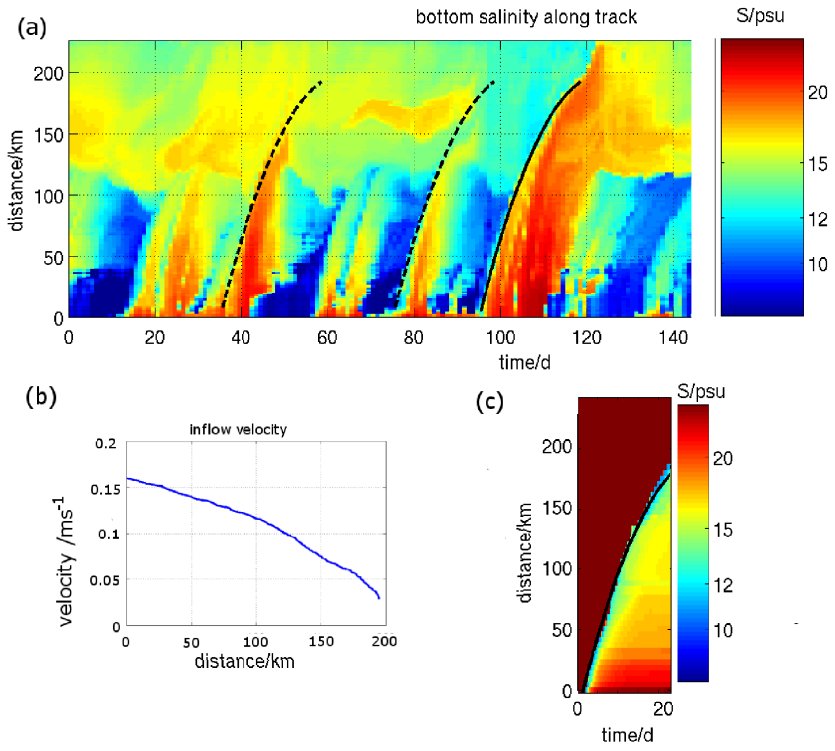

Figure 5.7: (a) Hovmueller plot for Arkona inflow events with different intensities during a realistic simulation (*Janssen et al.* [2006]). (b) With the slope shown in (a), the velocities for the salinity along track are obtained. (c) Hovmueller plot with velocity at the main bottom track plotted over time. Picture (a) and (b) were taken from *Janssen et al.* [2006].

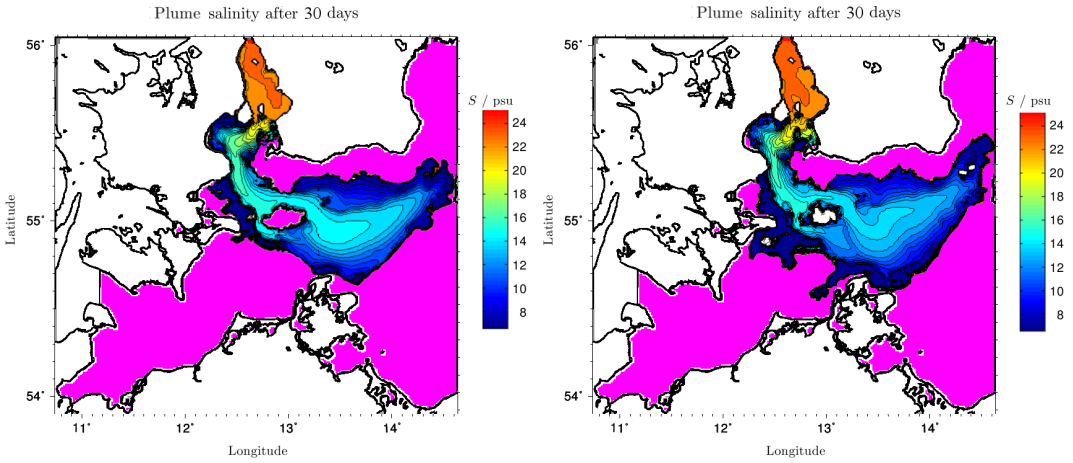

Figure 5.8: Simulation of the Arkona inflow event with different assumptions of the bottom drag coefficient. Left panel: C_D calculated under the assumption of a logarithmic velocity profile (2.46) and right panel: $C_D = 0.002$.

5.2.4 Variation of Froude number

A time series of the *Froude* number, required for the calculation of the entrainment rate E (Sect. 2.2.5), has shown that very unrealistic values of up to $Fr = 140$ were obtained at the front of the plume. This provides clear evidence that the implemented drying and flooding algorithm (Sect. 3.6.1) causes problems directly at the front of the plume where 'dry' grid boxes ($h_1 = D_{min}$) are instantly flooded. The motivation of this section is to find an appropriate maximum value for the *Froude* number. It is questionable, if the implemented entrainment formulation is guilty for *Froude* numbers above unity. Thus the value of $Fr = 1$ has been chosen for all model simulations. To demonstrate the dependency of the model results on a variation of the Froude number, two different simulations with a *Froude* number of $Fr = 0.7$ and $Fr = 1$ are compared (Fig. 5.9).
The differences shown in Fig. 5.9 are significant with a disagreement in both model results of one day. Increasing *Froude* numbers are connected to the Entrainment rate E with the following relation:

$$E \sim Fr^{2.77}, \tag{5.1}$$

that consequently induces a stronger mixing with ambient water. Thus the decreasing density contrast implicates a reduced velocity of propagation (see also Fig. 4.10).

5.2.5 Cross section of plume south of Drodgen Sill

The observational data from Feb 1 and Feb 2 in 2004 with a north-south transect south of Drodgen Sill (Fig. 5.1) is now compared with the idealized simulation of the Arkona

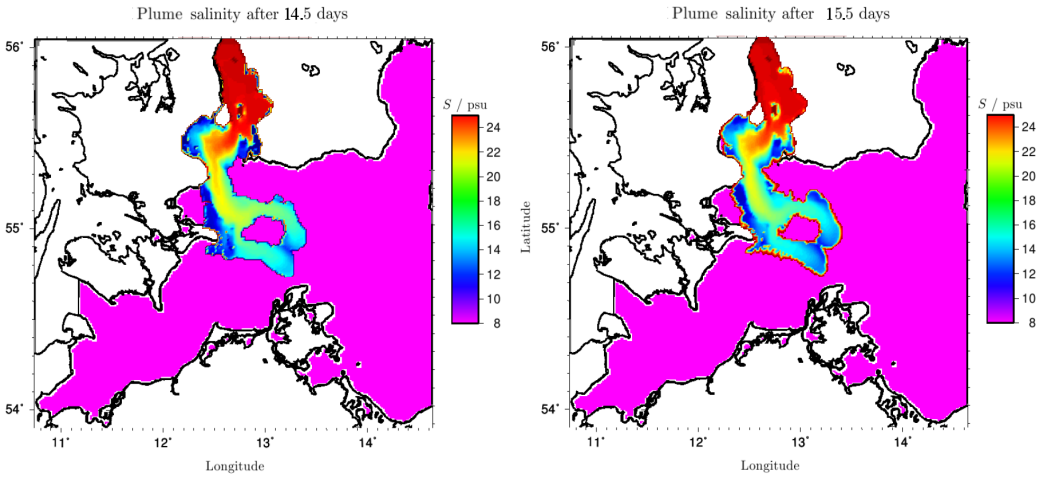

Figure 5.9: Propagation of plume after 14.74 and 15.74 days for Froude numbers of $Fr = 0.7$ (left panel) and $Fr = 1$ (right panel).

inflow event (Sect. 5.2.1). For the comparison with observations (Fig. 5.11) with the model results of the two layer model (Fig. 5.10) and GETM (Fig. 5.12) the eastern green line in Fig. 5.1 indicates the north-south transect used for the output of model data. With the help of the slices informations about salinity, eastward and northward velocity and plume thickness are obtained.
The observed data (Fig 5.11) shows salinities above 20 psu during the inflow event on Feb. 1 in 2004 that are reproduced by the two layer model result (Fig. 5.10) as well as by the GETM simulation (5.12). With southward velocities of up to 0.35 m s^{-1} for the two layer model result and maximum values of 0.35 m s^{-1} for the GETM result, both idealized simulations do not represent the observed southward velocities of 0.5 m s^{-1} over a broad band of the plume. The observed plume might be additionally driven by a barotrophic component over Drodgen Sill. Due to the stationary model forcing this is not resolved. Furthermore the observed peak fluxes of about $60,000$ m^3 s^{-1} and quasi-steady state fluxes of $5,500$ m^3 s^{-1} (5.20) for the two layer model simulation and $26,000$ m^3 s^{-1} for the GETM result (*Burchard et al.* [2005]) are not resolved. The direct comparison of both idealized model solutions corresponds well in velocity values of around 0.3 m s^{-1} eastward velocity at 55.45°N or $0.3-0.4$ m s^{-1} for the geographical position 55.1°N to 55.3°N.

5.2.6 Cross section of plume across Kriegers Shoal

The second observed dataset for a north-south transect across Kriegers Shoal is shown in Fig. 5.14. The obtained two layer model results for the eastern green line in Fig. 5.1 are presented in Fig. 5.13 and respectively for the GETM result in Fig. 5.15.
Fig. 5.13 shows the northern and southern channel of Kriegers Flak with the cor-

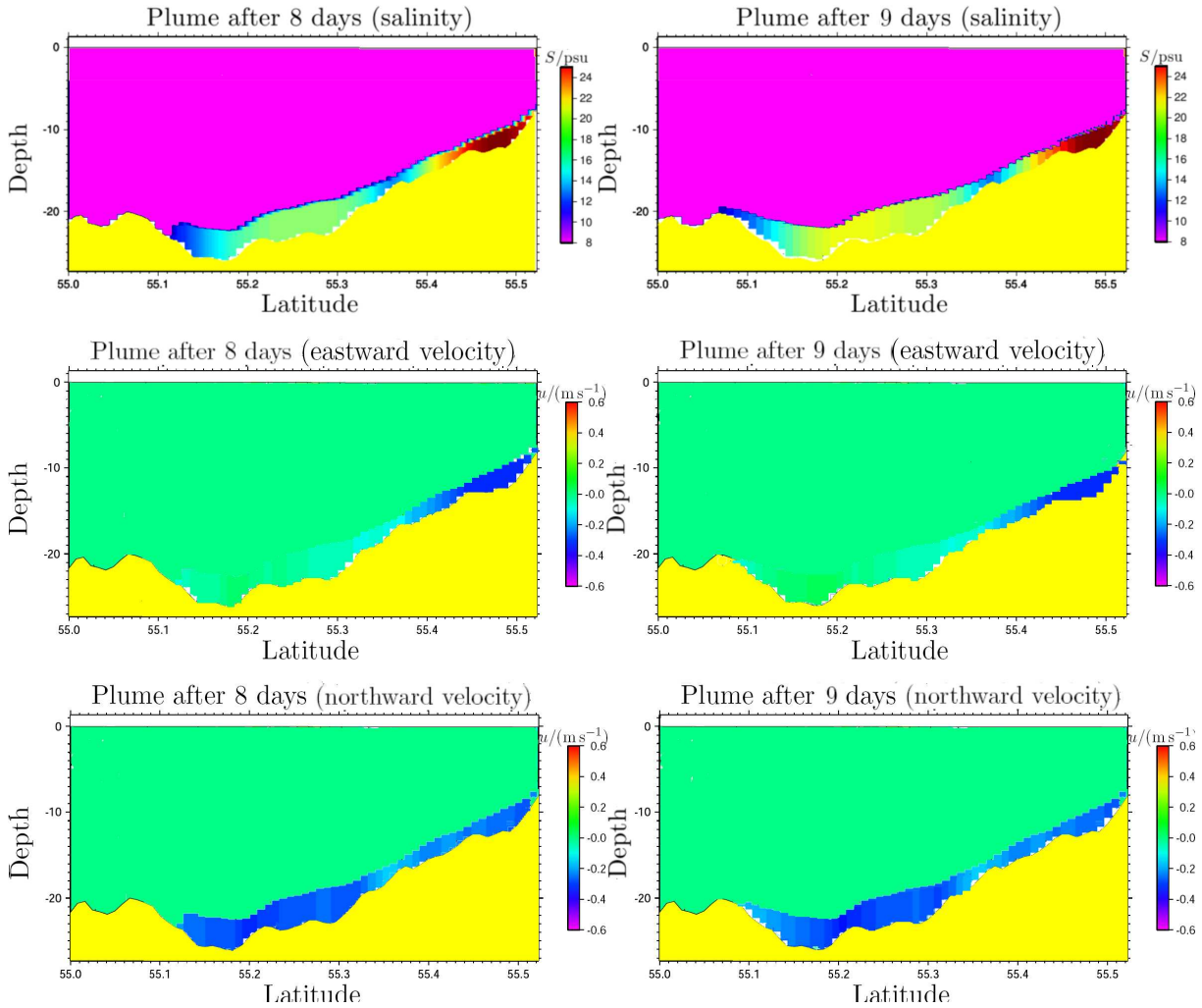

Figure 5.10: Simulated salinity and current velocity after 8 and 9 days with the two layer model on a north-south transect at 12°30′E south of Drodgen Sill.

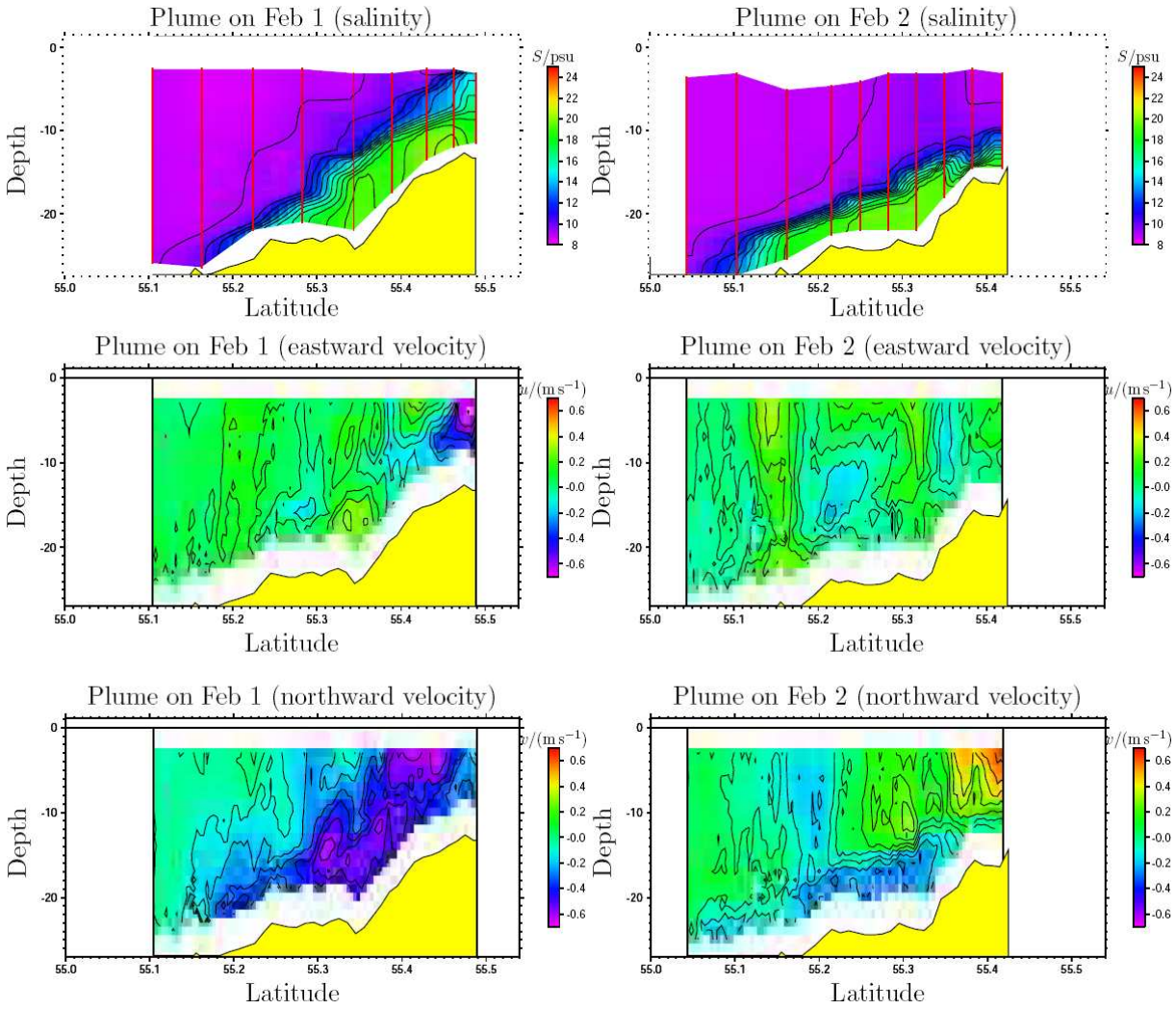

Figure 5.11: Observed salinity and current velocity on a north-south transect south from Drodgen Sill. Left panel: Feb 1 2004 from 16:20 to 20:41 h and right panel: Feb 2 from 10:24 to 14:47 h. The red lines in the upper two panels demonstrates the positions of the CTD (Conductivity, Temperature and Density) profiles. Picture taken from *Burchard et al.* [2005].

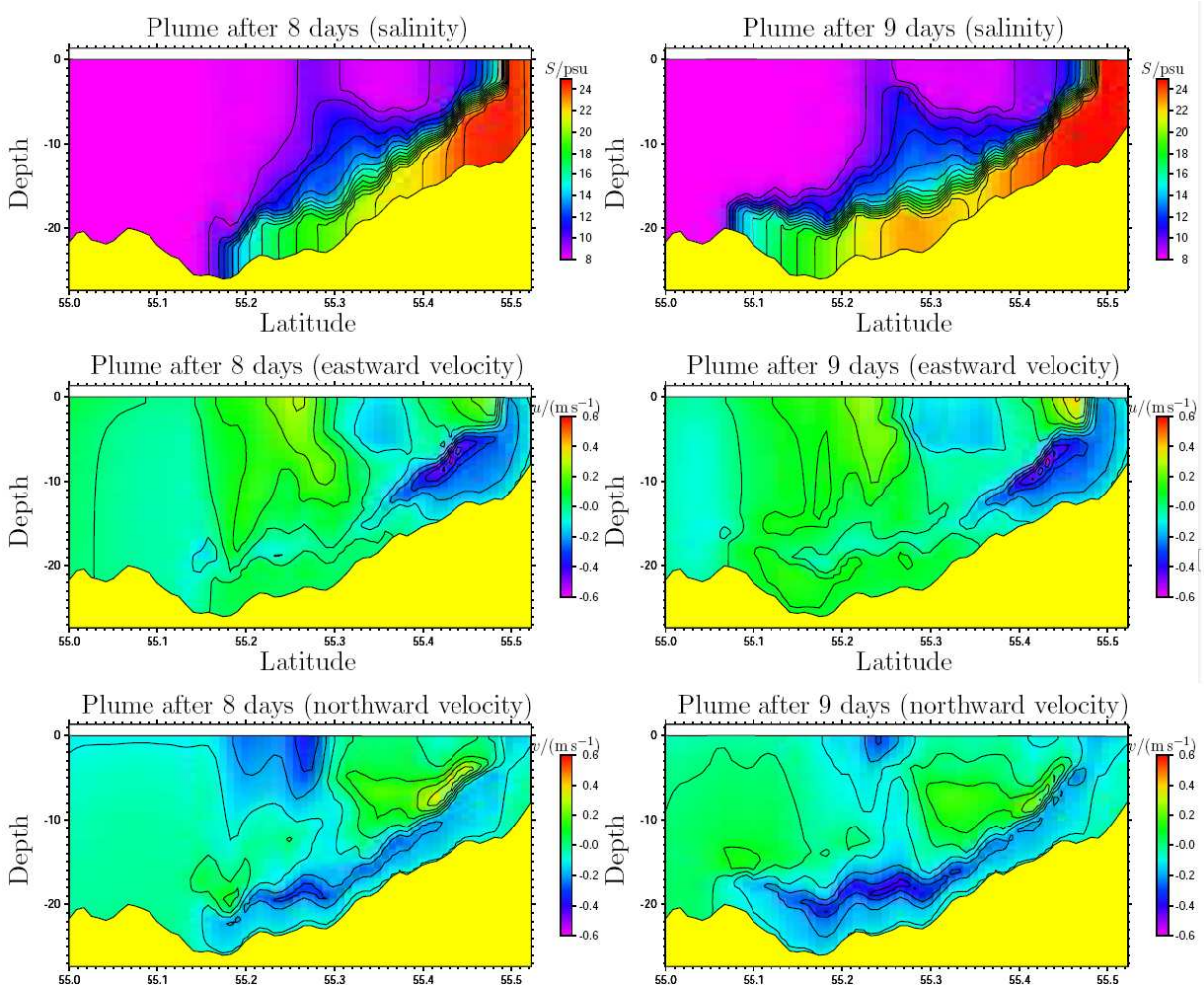

Figure 5.12: GETM-simulated salinity and current velocity after 8 and 9 days on a north-south transect at 12°30′E south of Drodgen Sill. Picture taken from *Burchard et al.* [2005].

responding branches at 35 m depth in the north and up to 40 m in the south. In both idealized simulations the northern and southern branch of the plume are not connected. As a consequence the additional mixing of dense water due to offshore wind farms planned to be built down to a depth of 25 m (Capt. 1) might only slightly increase. The two layer model basically reproduces the measurements from Feb 5 in 2004 (*Burchard et al.* [2005]) over Kriegers Flak with 17 psu (GETM: 21 psu) in the northern channel and 14 psu (GETM: 18 psu) in the southern channel. Water column measurements (*diamond* in Fig. 5.1a) as shown in Fig. 1.4 show the observed very sharp salinity gradients at the interface. The two layer model result is in good agreement with the salinity values but does not represent the measured plume thickness.
It must be considered that the two layer model result does only represent vertically averaged values for salinity and horizontal velocity component. Hence peak values for the horizontal velocity component, as they are obtained by the GETM result for northward and eastward velocity in the halocline (Fig. 5.15), that separates the plume from the ambient water, are not obtained. When considering mean values for a water column of the plume, the eastward velocity component of the two layer model simulated plume with up to 0.26 m s^{-1} represents the observations and the GETM result. For the northern branch the halocline is sloping down towards the north (Fig. 5.14). A result that is also obtained by both model simulations. Due to the geostrophic balance, the balance between Coriolis and pressure gradient force, the same applies for the southern branch of the plume. A major difference between the observations and the two layer model result is a very low southward velocity component with around 0.03 m s^{-1} whereas the observations show maximum values of 0.2 m s^{-1}. Although this can be justified by the vertically averaged values of the two layer model, it cannot describe different flow structures in vertical direction. Thus for example a bottom layer influenced by bottom friction cannot directly be shown by model results.

5.3 Baltic Sea inflow event with extended bathymetry

At the end of this thesis the bathymetry for the inflow event is spatially extended to the bathymetry used for the QuantAS-off project (Chapt. 1). The applied bathymetry (Fig. 5.1b) was kindly provided by Frank Janssen (BSH).
Simulations with this bathymetry might deliver improved results due to the fact that the plume crossing the Darss Sill is additionally resolved. As already shown in Fig. 5.2 the Darss Sill bottom current significantly changes the properties of the plume around Kriegers Shoal.
As it is obtained by the model results, the bottom current in the Arkona Sea significantly depends on the plume entering the Arkona Sea over the Darss Sill. The forcing of the model simulation is similar to Sect. 5.2 with a slightly increased surface elevation of $0.02m$ in the Kattegat and a surface level of 0 m at the other open boundaries. The salinity of inflowing water in the Kattegat is 25 psu. Furthermore the ambient brackish water has a salinity of 8 psu. The model domain consists of an open boundary in the east (Fig. 5.16).

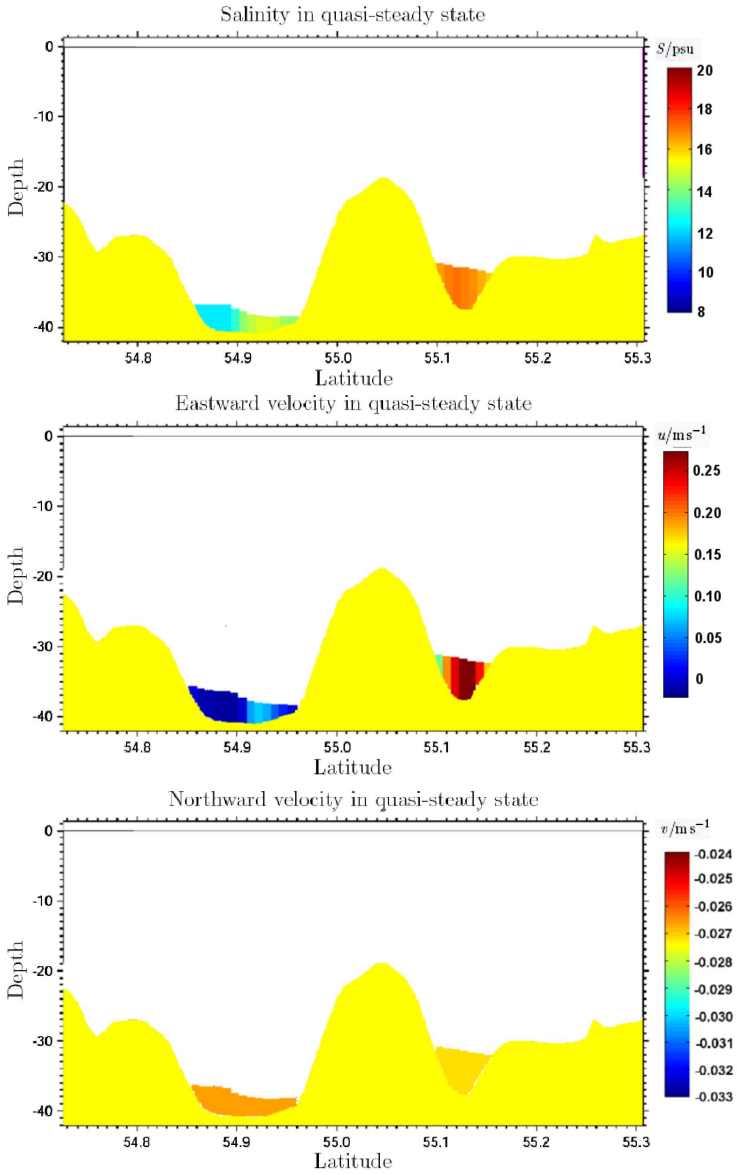

Figure 5.13: Simulated salinity and current velocity with the two layer model in quasi steady state on a north-south transect at 13°E across Kriegers Shoal.

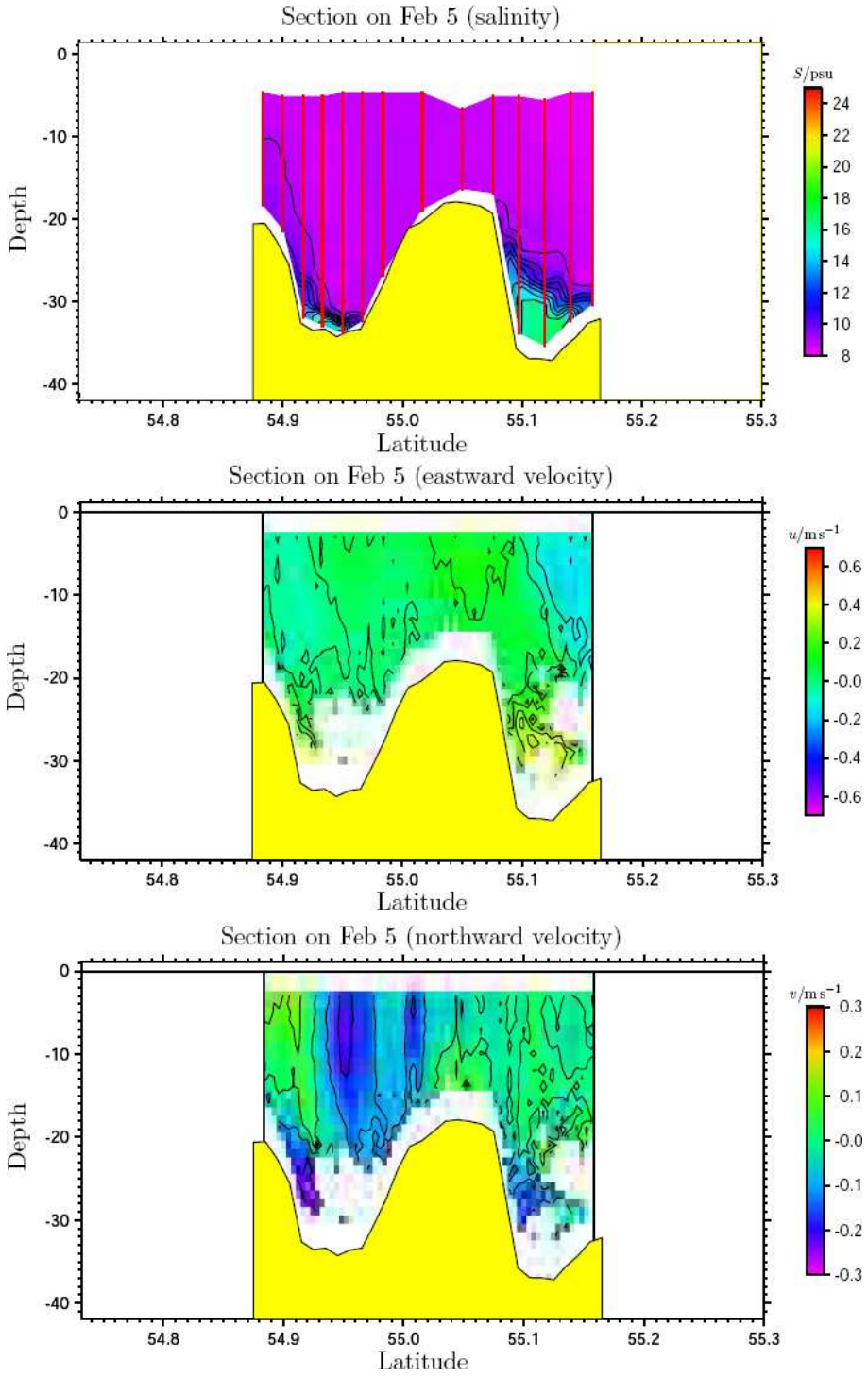

Figure 5.14: Observed salinity and current velocity on a north-south transect across Kriegers Shoal. With the help of CTD profiles and ADCP (Acoustic Doppler Current Profiler) measurements these observations were taken on Feb 5 from 10:45 to 15:31 h. The red lines in the upper panel shows the positions of the CTD (Conductivity, Temperature and Density) profiles. Picture taken from *Burchard et al.* [2005]

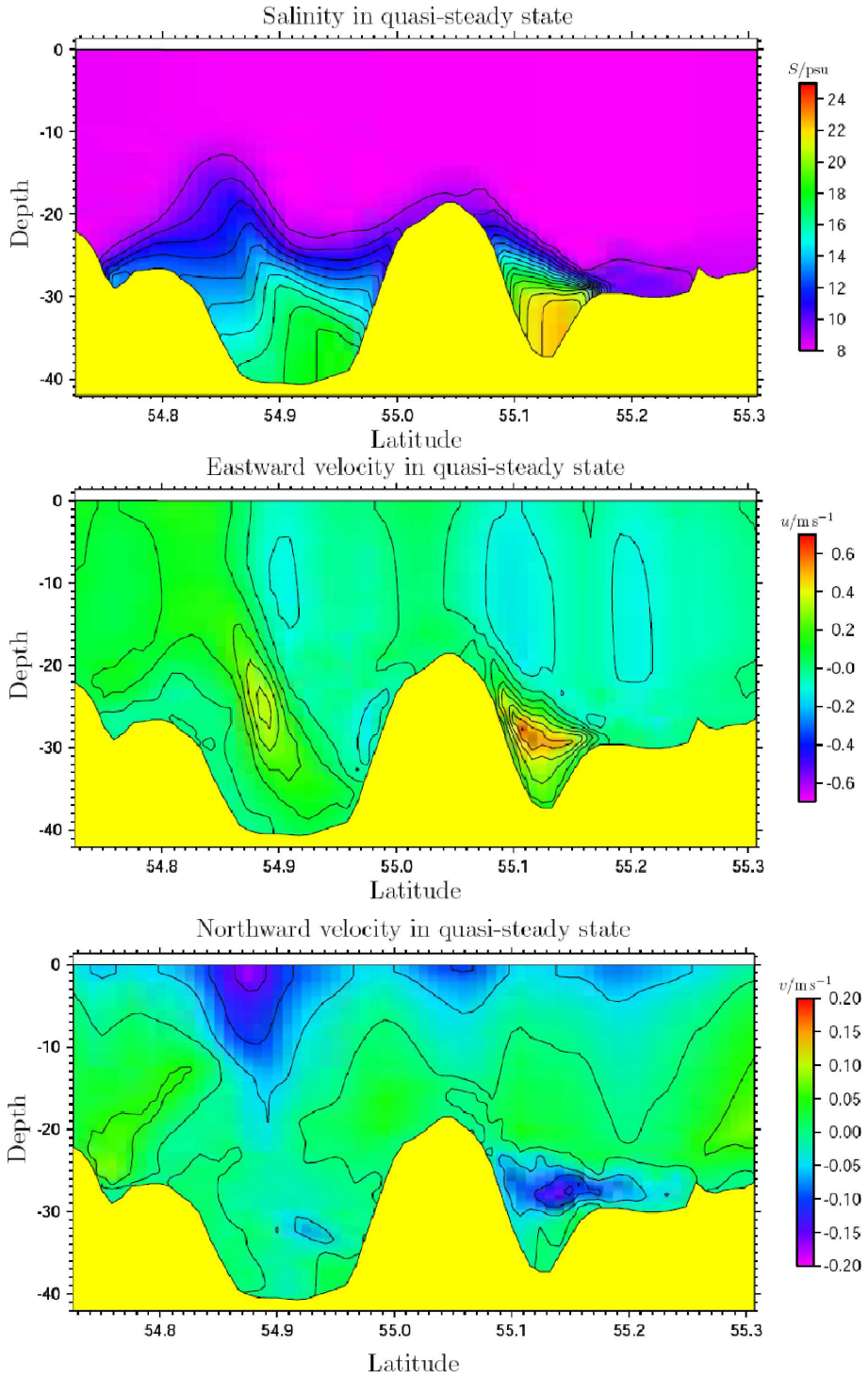

Figure 5.15: GETM-simulated salinity and current velocity in quasi steady state on a north-south transect at 12°30′E south of Drodgen Sill. Picture taken from *Burchard et al.* [2005]

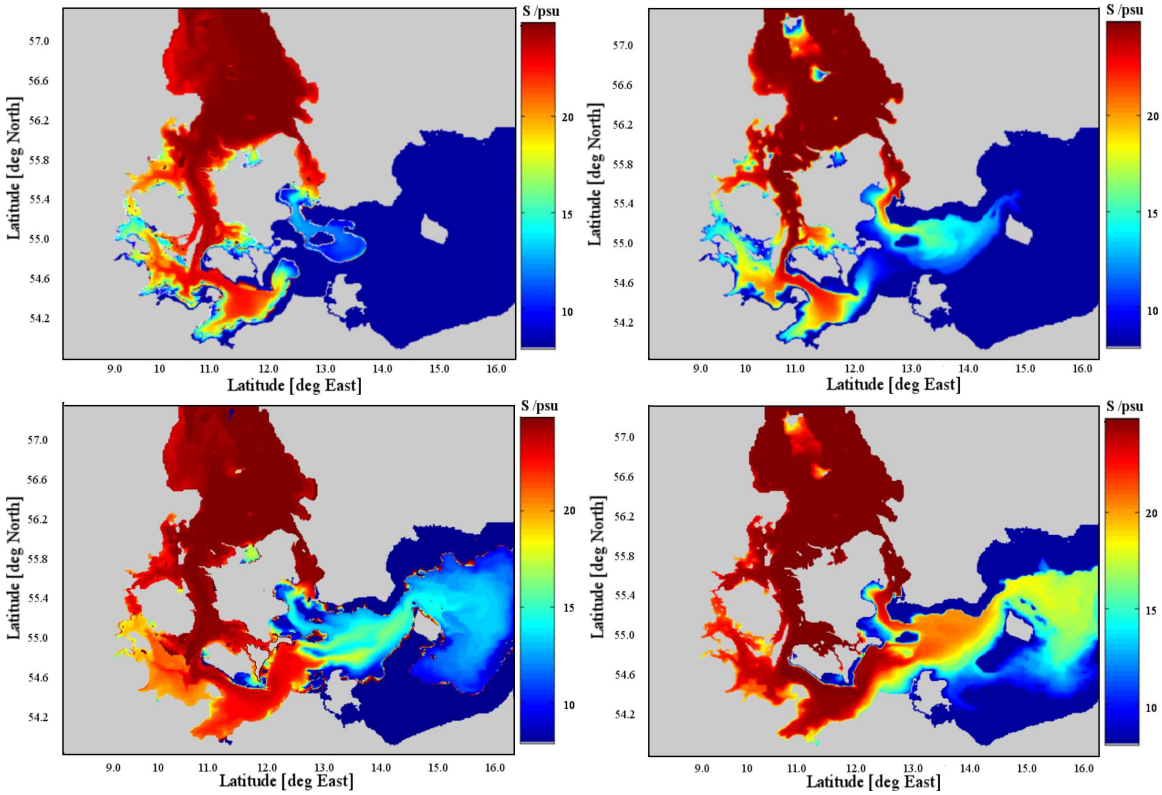

Figure 5.16: Idealized inflow event simulation with two layer model (upper left panel, plume salinity) and GETM (upper right panel, bottom salinity) after 60 days and respectively after 142 days (lower panels). Upper right and lower right panel taken from *Janssen et al.* [2006].

Astonishingly the plume crossing the Great Belt and the Fehmarn Belt reaching the Darss Sill after 60 days corresponds with only a difference of around one day for both the two layer simulated and the GETM simulated plume (Fig. 5.16). This may lead to the assumption that the plume can very well be assumed by gravity current dynamics and the main processes as there are Coriolis force, baroclinic and barotrophic pressure gradients and the entrainment rate as a local process that only depends on the state of a single water column. The distribution of salinity with around 21 psu at the Fehmarn Belt for the GETM as well as for the two layer model result is similar. A time-series of salinities is shown in Fig. 5.18. It is obvious that the mixing process from Drodgen Sill and Darss Sill on is very strong with salinities in the range of $23.5 - 25$ psu in the Danish Belts and the Oeresound and values of only $13.5 - 17.5$ psu in the Arkona Sea. South of Kriegers Shoal an area of low salinity values is obtained (Fig. 5.16). Both the two layer model simulation and the GETM simulation represent this state. The occurance of this area with density differences of up to 4 psu compared to the surrounding water masses is not only represented by idealized model simulations. Realistic simulations with GETM over a period of half a year have shown this effect, too (*Janssen et al.* [2006]). The bottom current is topographically stirred by the bathymetry forming two channels surrounding the low saline area.
The obtained flowrates during the inflow event are shown in Fig. 5.20. The ratio between the flowrate in the Great Belt and the Oeresound is 7.5 : 1. The flowrate through the Oeresound would have been expected as bigger. Observations that can be compared with this model result are difficult to obtain. The reason for the big flowrate at the Great Belt can be demonstrated with the model result as shown in Fig. 5.16. The plume crossing the Drodgen Sill with a depth of only 8 m is significantly slower than the GETM-simulated plume crossing Drodgen Sill. Closer investigations of the two layer model results for the dynamics at Drodgen Sill have shown, that it took nearly 7 days for the plume to cross Drodgen Sill. Thus only a little amounts of dense bottom water are crossing Drodgen Sill. Due to small plume thickness values at Drodgen Sill the vertical mixing is very effective and rapidly changing the salinity distribution of the plume as seen in Fig. 5.16. A run of the two layer model with more correct flowrates for the ratio between the Great Belt and the Oeresound requires the bathymetry to be modified especially at Drodgen Sill.
The calculated flowrate of $58,000$ m^3 s^{-1} for the quasi-steady state of the model simulation in the Bornholm Channel is in agreement with the calculated flowrates of *Kõuts and Omstedt* [1993] demonstrated in Fig. 5.21. A calculated time series of flowrates for positions in the Arkona Basin Fig. 5.20) and the flowrate in the quasi-steady state (Fig. 5.19) demonstrates that the flowrate increases to 87% from western of Kriegers Shoal up to the Bornholm Channel. *Kõuts and Omstedt* [1993] obtained a calculated flowrate of only 53% for the Arkona Basin.
Stigebrandt [1987] has shown that the plume crossing the Bornholm Channel has a mean salinity of 13.59 psu with a range between 12 and 16 psu. These values are in good accordance to the two layer model results shown in Fig. 5.21d and Fig. 5.18b.
Time series of measured salinities at the hydrographic stations Møn and Bornholm from Oct 10 1998 to Jan 8 1999 (Fig. 5.17a) *Lass and Mohrholz* [2003] have shown

that the delay between both stations is 12 days with salinity differences of 1.41 to 1.47 psu for the peak values of the corresponding events. The salinity values obtained by the idealized two layer model simulation predicts a different picture as demonstrated in Fig. 5.17a and 5.17b for the quasi-steady state. The simulated density difference between both stations is completely different to the obtained values with higher salinity values for station Bornholm than for station Møn with a density difference of 1.2 psu. The reason might be that the simulation result additionally represents the strong bottom current crossing the Darss Sill with higher salinity values. The station Møn is not influenced by this bottom current and only reflects the bottom current that has crossed the Drodgen Sill with smaller salinity values. Moreover the simulated delay between both stations is different from the observations. With a delay of 22 days the simulated bottom current is nearly 10 days slower than the observed bottom current. An inspection shows that the observed peak values for the salinity of around 22 psu (Fig. 5.17a) are higher than the simulated salinities for the quasi-steady state (Fig. 5.17a) with a peak value for the Bornholm station of only 15.5 psu. Thus the velocity of propagation of the simulated plume is less than observed due to smaller values for the density contrast west of Kriegers Shoal. Even in the south of Kriegers Shoal, where the merging process of the bottom current crossing the Darss Sill and the bottom current from Drodgen Sill takes place, the simulated peak salinity value in quasi-steady state of 17.5 psu is much smaller than the observed peak values for the salinities of 22.5 psu at station Møn and 21 psu at station Bornholm. A deeper investigation of the model results indicate that the geographical regions of the Darss Sill and the Drodgen Sill play a very important role for the dilution of the bottom current. This has also been shown by investigation of the corresponding transport rates in the Arkona Basin (Fig. 5.19). The strong decrease in salinity values can be seen with the help of the obtained salinity values after 60 and 142 days in Fig. 5.16 as well as with a plotted time series of plume salinities in Fig. 5.18. The salinity values for positions in the Great Belt, Fehmarn Belt, Drodgen Sill and Darss Sill are much higher than the salinities obtained for the bottom current that has already passed the Drodgen Sill and the Darss Sill (Fig. 5.18b).

5.3.1 Splitting and merging around Kriegers Shoal

Additional information about the splitting and merging process due to Kriegers Shoal in the area shown in Fig. 5.5 is obtained in this section. Fig. 5.22 represents the simulation results obtained by the idealized simulation with the smaller bathymetry (Fig. 5.1a) whereas Fig. 5.23 represents the model results while applying the bathymetry shown in Fig. 5.1b.
With depth values of less than 20 m Kriegers shoal is forming a barrier for the plume. Hence the bottom current is splitted in the west (Fig. 5.22) with the consequence of a northern and a southern branch. Fig. 5.22 is demonstrating what previous sections and investigations (*Burchard et al.* [2005]) have already shown. The main transport of saline bottom water occurs north of Kriegers Shoal with velocities up to 0.35 m s^{-1} and 0.22 m s^{-1} in the south. A time series of current velocity vectors (Fig. 5.22) points

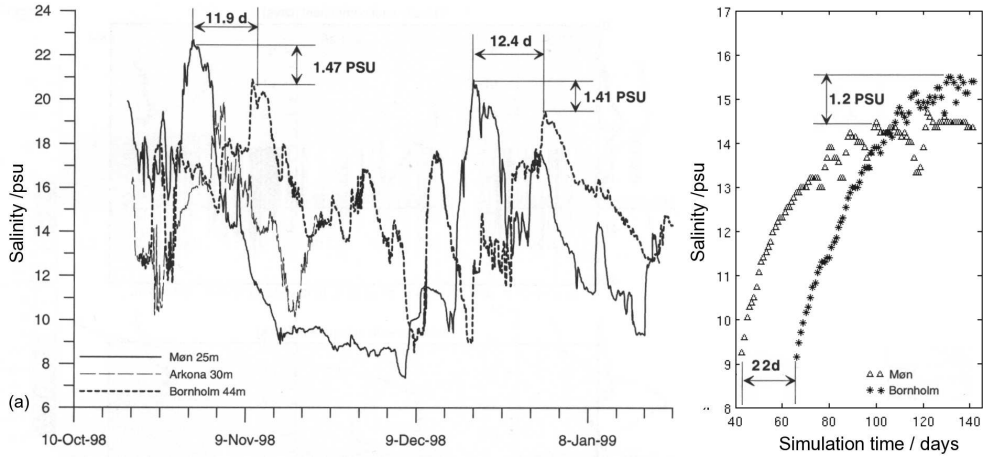

Figure 5.17: Observed (left panel) and two layer simulated (right panel) salinities at the hydrographic stations Møn and Bornholm. Left picture taken from *Lass and Mohrholz* [2003].

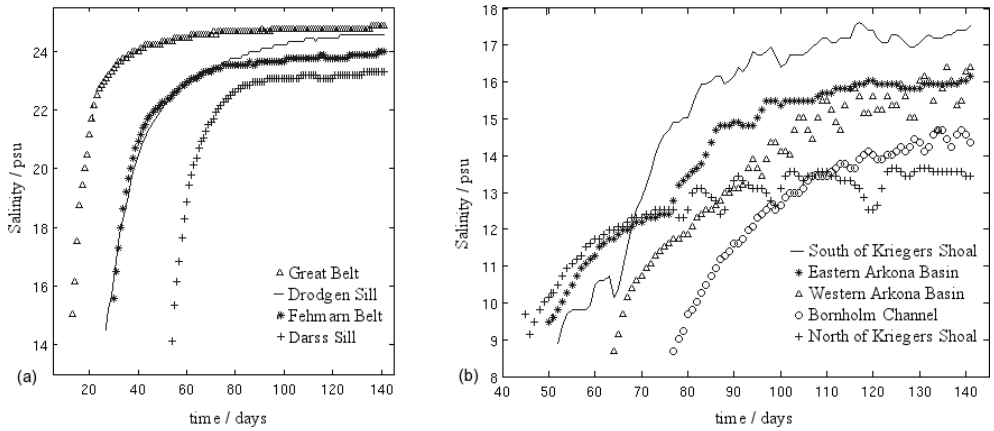

Figure 5.18: Time-series of simulated salinities at different regions in the western Baltic Sea.

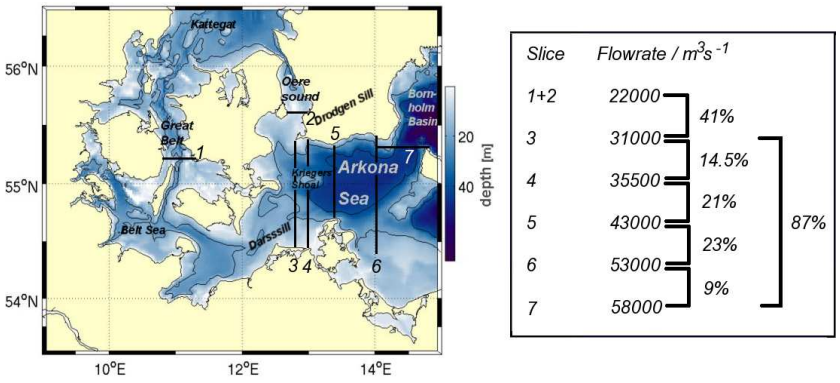

Figure 5.19: Picture showing the simulated flowrates for the quasi-steady state of the two layer model simulation for different slices through the western Baltic Sea.

out that the plume is splitted after 8.5 days and merged again three days later. South-east of Kriegers Shoal, where both branches join each other to flow into the Arkona Basin, two eddies, a cyclonal and an anti-cyclonal one, are forming. They remain stable over the simulated period of 30 days with a diameter of around 10 km. The current velocities in the eddies are weak with values below 7 cm s^{-1} (Fig. 5.22f). The mean plume thickness for the investigated area is in the range of $5 - 6$ m (Fig. 5.22e). The obtained values for the current velocity in the Arkona Basin are between 7 cm s^{-1} and 8 cm s^{-1}.

A completely different flow structure and plume distribution occurs when additionally the bottom current crossing the Darss Sill comes into account (Fig 5.23). The bottom current crossing the Darss Sill joins the southern branch of the bottom current south of Kriegers Shoal. Thus the directions of the current velocity east of Kriegers Shoal are significantly influenced. Peak values of 15 cm s^{-1} occur in the Arkona Basin. The current velocities south of Kriegers Flak increased from 0.18 m s^{-1} to 0.33 m s^{-1} for the bottom current under consideration of the plume crossing the Darss Sill. The plume thicknesses now reach values between 10 and 15 m in the Arkona Basin.

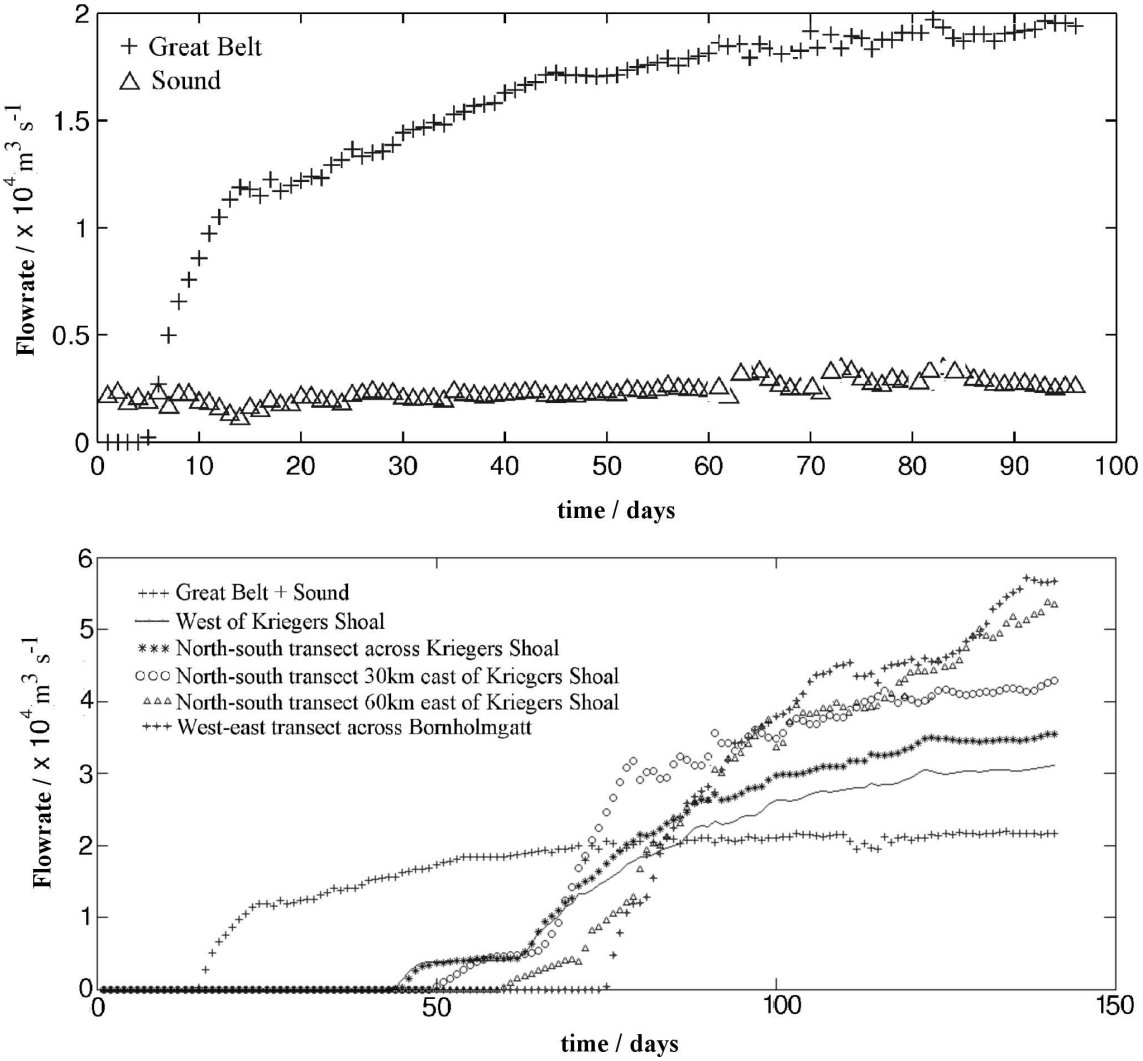

Figure 5.20: Upper panel: Water mass fluxes at the Sound ($2800 m^3 s^{-1}$) and the Great Belt ($19000 m^3 s^{-1}$) for the quasi steady state during the idealized inflow event with the two layer model. Lower panel: Water mass fluxes at different positions during the idealized inflow event.

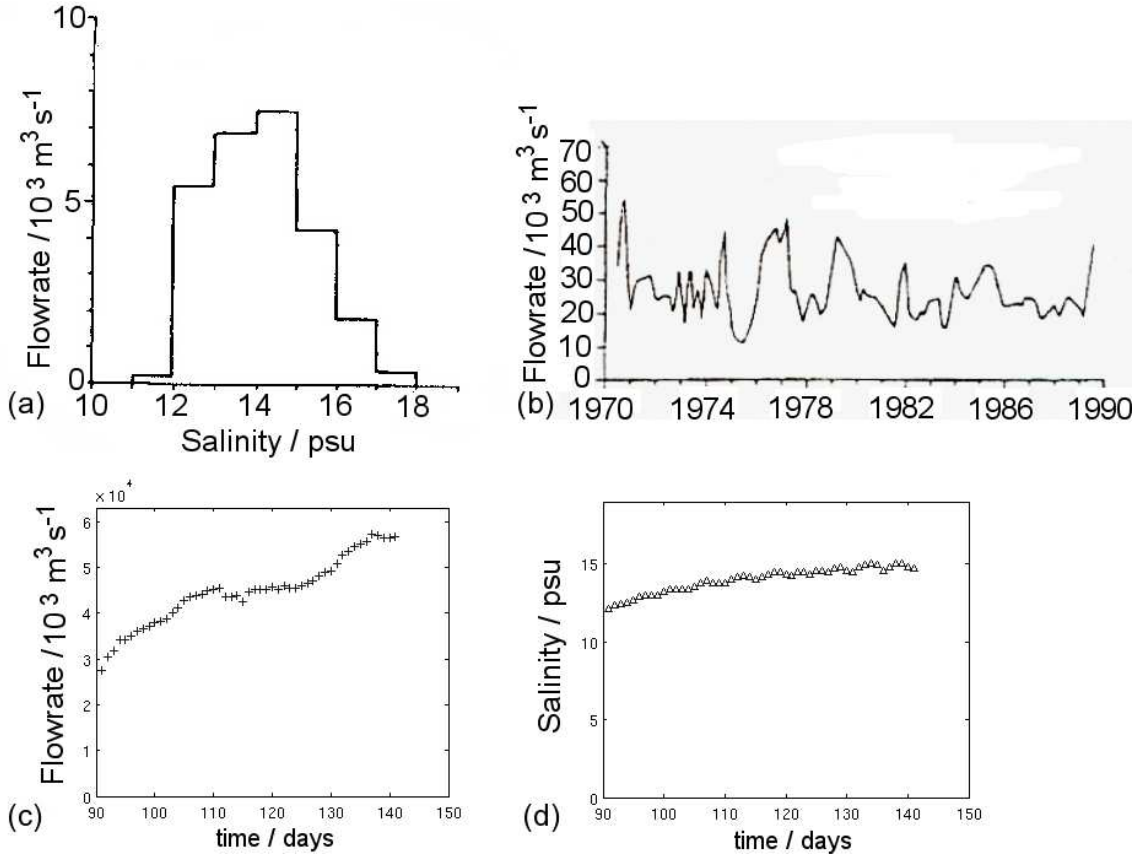

Figure 5.21: (a) Calculated salinity distribution for the geostrophic outflow rates in the Bornholm Channel. Picture taken from *Kõuts and Omstedt* [1993]. (b) Geostrophic outflow calculations for the period 1970-1990 in the Bornholm Channel. Picture taken from *Kõuts and Omstedt* [1993].(c) Time-series of flowrate of lower layer with two layer model for the Bornholm Channel. (d) Time-series of salinity distribution in lower layer with two layer model for the Bornholm Channel.

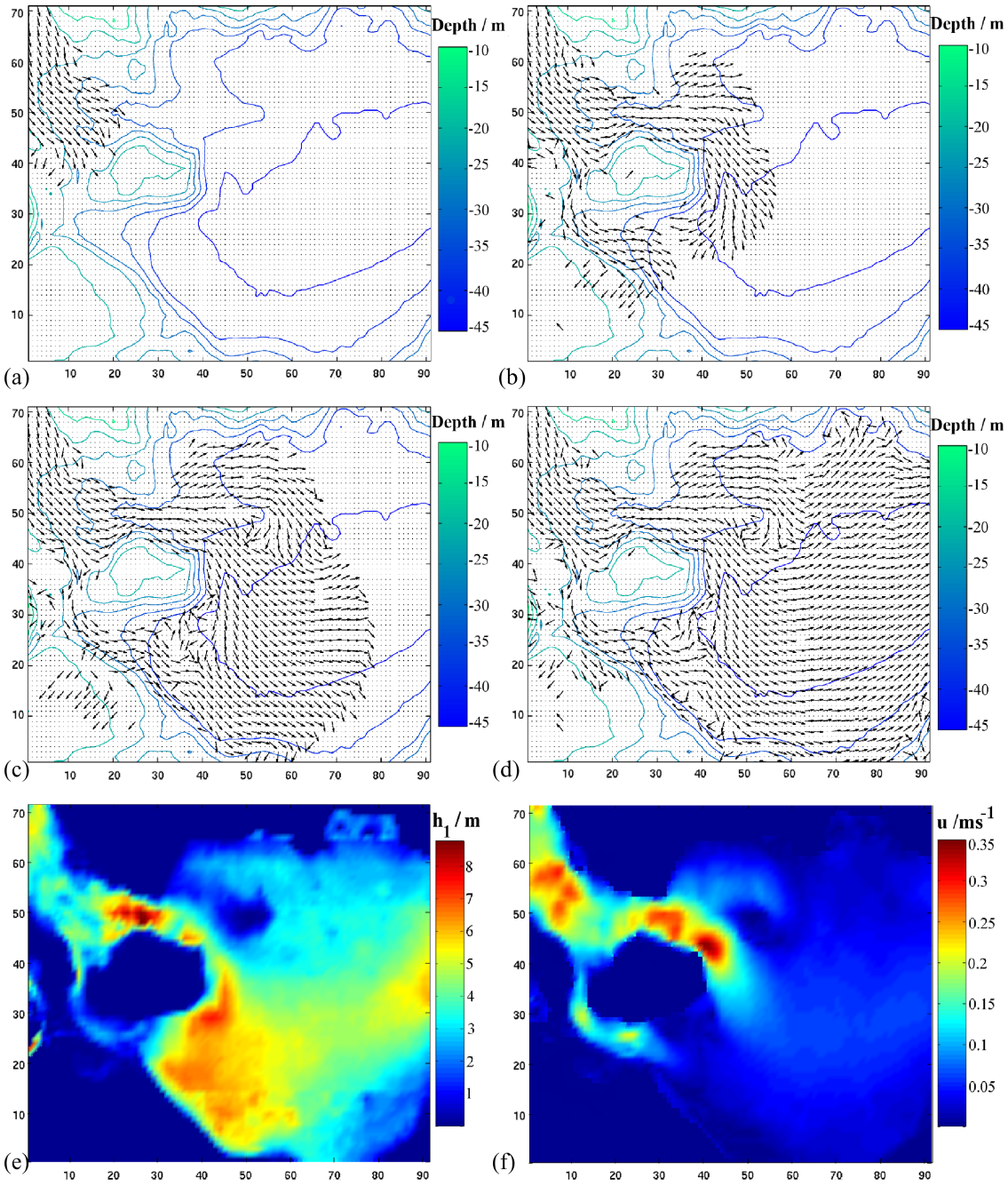

Figure 5.22: Current velocity vectors in the region of Kriegers Flak after (a) 8.5, (b) 11.5, (c) 15.5 and (d) 30 days. (e) The plume thickness near Kriegers Shoal and (f) the current velocity of the plume. The values in the legend represent the grid boxes used for discretisation of model equations whereas one grid box in east direction represent a length of 1036 m and one grid box in north direction a length of 909 m.

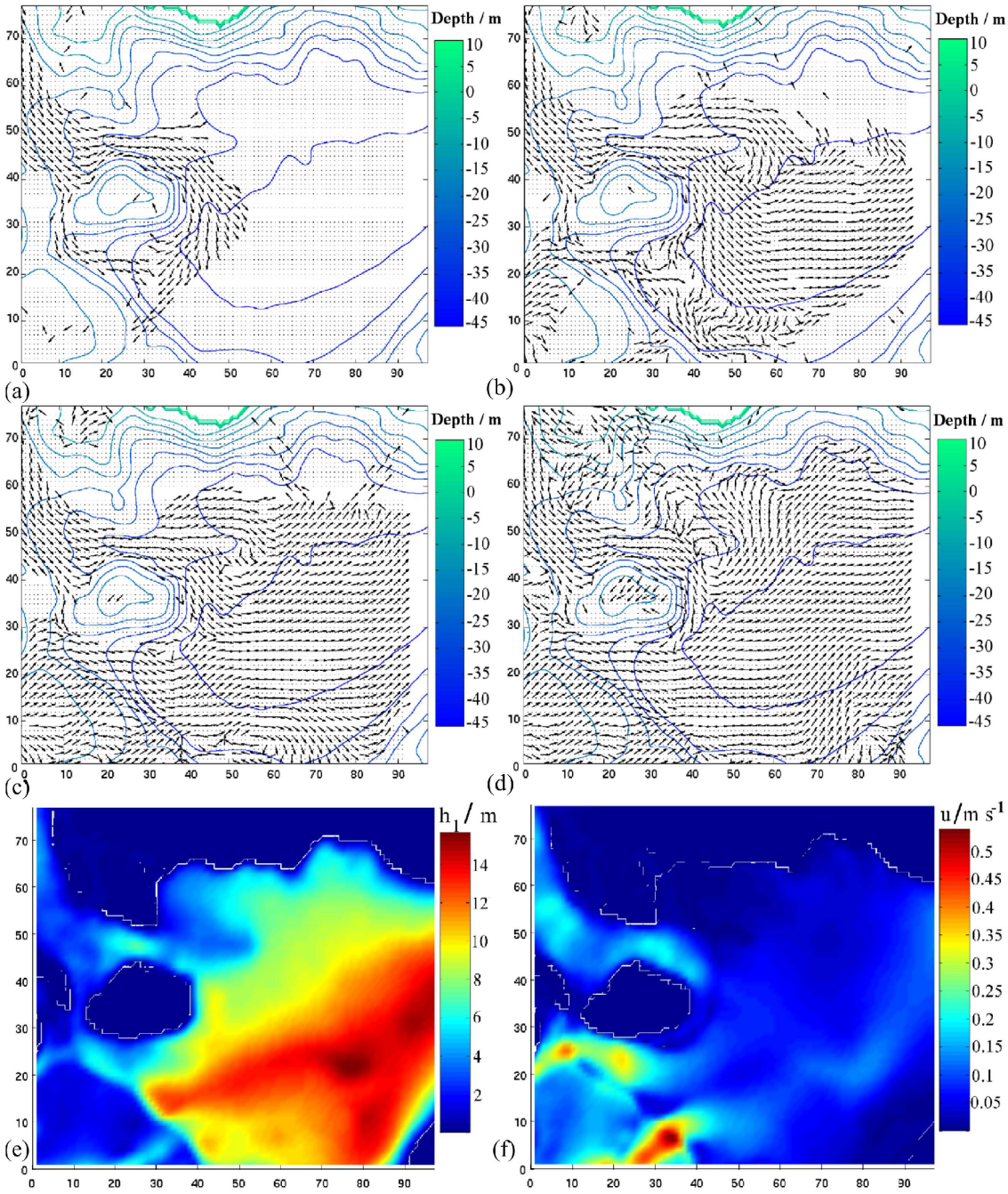

Figure 5.23: Current velocity vectors in the region of Kriegers Flak after (a) 29, (b) 56, (c) 77 and (d) 151 days. (e) The plume thickness near Kriegers Shoal and (f) the current velocity of the plume. The values in the legend represent the grid boxes used for discretisation of model equations whereas one grid box in east direction represent a length of 1036 m and one grid box in north direction a length of 909 m.

Chapter 6

Conclusions

This study on the dynamics, mixing processes and pathways of saline bottom currents during the Baltic Sea inflow event with special interest on the Arkona Sea has demonstrated that the idealized approach of a two layer system for the saline bottom current is justified. Model results compared to recent observations as obtained during a medium-intensity saltwater inflow event over Drodgen Sill in Jan and Feb 2004 (*Burchard et al.* [2005]) are in good agreement. It has been demonstrated that dense water plumes from Drodgen Sill are mainly propagating north of Kriegers Shoal with significantly lower flowrates for the branch south of Kriegers Shoal. This feature of the saline plume has also been a main conclusion of *Burchard et al.* [2005].
It has also been shown that the Arkona Sea as the most western basin of the Baltic Sea plays a very important role for water mass transformations with an increase of the flowrate up to a calculated value of 87% from west of Kriegers Shoal up to the Bornholm Channel.
Due to the comparatively simple model output of the two layer model as a horizontal two-dimensional physical system, basic assumptions for flowrates north and south of Kriegers Shoal as well as for the Arkona Sea were easily obtained.
Furthermore it was possible to demonstrate that the saline bottom current crossing the Darss Sill significantly influences the current velocities and directions in the south-east of Kriegers Shoal. Additionally the impact of the flow from Darss Sill turns out to have only negligible impact on the bottom current in the north of Kriegers Shoal. For the time being this can only be assumed for the applied idealized simulation. Obtained flowrates in the Bornholm Channel have shown similar results as calculated by *Kõuts and Omstedt* [1993].
Main reasons for qualitative less good results are: idealistic model forcing, saline bottom current as two layer system, numerical diffusion of two layer model and too coarsely horizontal model resolution.
It is noteworthy that the dynamics of the two layer model simulated plume are in very good agreement with the simulations of the 3D ocean model GETM. The disagreement in the velocity of propagation between both models for the plume crossing the Danish Belts is less than 2 days after nearly two months of simulation. The agreement in

the dynamics and lateral broadening of the plume during the idealized Arkona inflow event was surprisingly good, too. The reason may be the use of the recently developed formulation for the entrainment rate (*Arneborg et al.* [2005]). This formula is directly based on observations in the Arkona Sea, the geographical region mainly investigated with the two layer.
An advantage of this model is the simplicity of the model output compared to the 4D output of 3D models that is comparatively hard to analyse. Consequently the reason of the well mixed bottom water south of Kriegers Flak could easily be investigated and explained.

Additionally the two layer model can be applied for lake research with the investigation of Kelvin waves and internal waves. An expansion of the two layer model to a three layer model would be purposeful.
Further investigations about bottom currents running into the Gotland deep are planned within the scope of a master thesis at the Baltic Sea Research Institute of Warnemünde.

Bibliography

Arneborg, L., V. Fiekas, L. Umlauf, and H. Burchard, Gravity current dynamics and entrainment - a process study based on observations in the Arkona Basin, *J. Phys. Oceanogr.*, 2005, submitted.

Backhaus, J. O., A three dimensional model for the simulation of shelf sea dynamics, *Deutsche Hydrographische Zeitschrift*, *38*, 165–186, 1985.

Baines, P. G., Mixing in flows down gentle slopes into stratified environments, *J. Fluid Mech.*, *443*, 237–270, 2001.

Baringer, M. O., and J. F. Price, A simple model of the descending Mediterranean outflow plume, *Pratt, L.J., The physical oceanography of sea straits*, pp. 537–544, 1990.

Baumert, H., G. Bruckner, E. Kleine, R. Kluge, and W. Müller, Numerische und analytische Untersuchungen und Rechenprogramme für den Wärme- und Stofftransport in Oberflächengewässern auf der Basis der dreidimensionalen instationären Reynoldsgleichungen für inkompressible Flüssigkeiten mit freier Oberfläche unter Einbeziehung von Turbulenzmodellen, Abschlußbericht zur G_4-verteidigung, 1989.

Bo Pedersen, F., A monograph on turbulent entrainment and friction in two-layer stratified flow, Ph.D. thesis, Danish Technical University, Lyngby, Denmark, 1980a, published as: Series Paper 25, IHHE, DTU, Lyngby, Denmark, 397 pp.

Bo Pedersen, F., *Dense bottom currents in Rotating Ocean*, 1980b, published as: Journal of the Hydraulic Division, Proceedings of the American Society of Civil Engineers,19.

Bowden, K. F., The dynamics of flow on a submarine ridge, *Tellus*, *12*, 1960.

Britter, R. E., and P. F. Linden, The motion of the front of a gravity current travelling down an incline, *J. Fluid Mech.*, *99*, 531–543, 1980.

Bronstein, I. N., and K. A. Semendjajew, *Taschenbuch der Mathematik*, fourth ed., Harry Deutsch Verlag, Frankfurt am Main, 1984.

Buch, E., On entrainment observed in laboratory and field experiments, *Tellus*, *34*, 307–311, 1982.

Burchard, H., Turbulenzmodellierung mit Anwendungen auf thermische Deckschichten im Meer und Strömungen in Wattengebieten, Ph.D. thesis, Institut für Meereskunde, Universität Hamburg, 1995, published as: Report 95/E/30, GKSS Research Centre.

Burchard, H., and K. Bolding, GETM – a general estuarine transport model. Scientific documentation, *Tech. Rep. EUR 20253 EN*, European Commission, 2002.

Burchard, H., K. Bolding, and M. R. Villarreal, Three-dimensional modelling of estuarine turbidity maxima in a tidal estuary, *Ocean Dynamics*, *54*, 250–265, 2004.

Burchard, H., H. Lass, V. Mohrholz, L. Umlauf, J. Sellschopp, V. Fiekas, K. Bolding, , and L. Arneborg, Dynamics of medium-intensity dense water plumes in the Arkona Sea, Western Baltic Sea, *Ocean Dynamics*, 2005, accepted for publication.

Cenedese, C., J. A. Whitehead, J. A. Ascarelli, and M. Ohiwa, A dense current flowing down a sloping bottom in a rotating fluid, *Journal of Physical Oceanography*, *34*, 188–203, 2004.

Ellison, T. H., and J. S. Turner, Turbulent entrainment in stratified flows, *J. Fluid Mech.*, *6*, 423–448, 1959.

Griffiths, R. W., Gravity currents in rotating systems, *Annu. Rev. Fluid Mech.*, *18*, 59–89, 1986.

Hornung, H. G., C. Willert, and S. Turner, The flow field downstream of a hydraulic jump, *J. Fluid Mech.*, *287*, 299–316, 1995.

Janssen, F., H. Burchard, and K. Bolding, Simulation of dynamics and mixing in the the western Baltic sea, 2006, in preparation.

Jungclaus, J., Ein numerisches Model zur Simulation dichter Bodenströmungen im Ozean mit Anwendung auf den 'Overflow durch die Dänemarkstrasse', Ph.D. thesis, 1994.

Kõuts, T., and A. Omstedt, Deep water exchange in the Baltic Proper, *Tellus Ser. A*, *45A*, 311–324, 1993.

Kundu, P. K., and I. M. Cohen, *Fluid Mechanics*, first ed., Academic Press, San Diego, London, 1997.

Lass, H. U., and V. Mohrholz, On the dynamics and mixing of inflowing salt-water in the Arkona Sea, *J. Geophys. Res.*, *108*, 3042–3057, 2003.

Liljebladh, B., and A. Stigebrandt, Observations of the deepwater flow into the Baltic Sea, *J. Glaciol.*, *101*, 8895–8911, 1996.

Matthäus, W., and H. Franck, Characteristics of major Baltic inflows, a statistical analysis, *Cont. Shelf Res.*, *12*, 1375–1400, 1992.

Mesinger, F., and A. Arakawa, Numerical methods used in atmospheric models, *WMO - ICSU*, *17*, 1976.

Oguz, T., E. Özsoy, M. A. Latif, H. I. Sur, and U. Ünlüata, Modeling of hydraulically controlled exchange flow in the Bosphorus Strait, *J. Phys. Oceanogr.*, *20*, 945–965, 1990.

Pratt, L. J., Rotating shocks in a separated laboratory channel flow, *J. Phys. Oceanogr.*, *17*, 483–491, 1987.

Roed, L. P., and C. K. Cooper, Open boundary conditions in numerical ocean models, *Advanced Physical Oceanographic Numerical Modelling*, pp. 411–436, 1986.

Simons, T. J., Circulation models of lakes and inland seas, *Can. Bull. Fish. Aquat. Sci.*, *203*, 146pp, 1980.

Smith, P. C., A streamtube model for bottom boundary currents in the oceans, *Deep-Sea Research*, *22*, 853–873, 1975.

Stigebrandt, A., Computations of the flow of dense water into the Baltic Sea from hydrographical measurements in the Arkona Basin, *Tellus*, *39A*, 170–177, 1987.

Turner, J. S., *Buoyancy effects in fluids*, Cambridge University Press, Cambridge, 1973.

Turner, J. S., Turbulent entrainment: the development of the entrainment assumption, and its application to geophysical flows, *J. Fluid Mech.*, *173*, 431–471, 1986.

Umlauf, L., H. Burchard, and K. Bolding, General Ocean Turbulence Model. Source code documentation, *Tech. Rep. 63*, Baltic Sea Research Institute Warnemünde, Warnemünde, Germany, 2005.